



# MONASH University

## A numerical and experimental investigation of the turbulent elliptical cylinder wakes

by

Daniah Saleh Hajji Aljubaili

BEng(Hons)

---

---

A Thesis submitted to Monash  
University for the degree of  
Master of Engineering Science (Research)

---

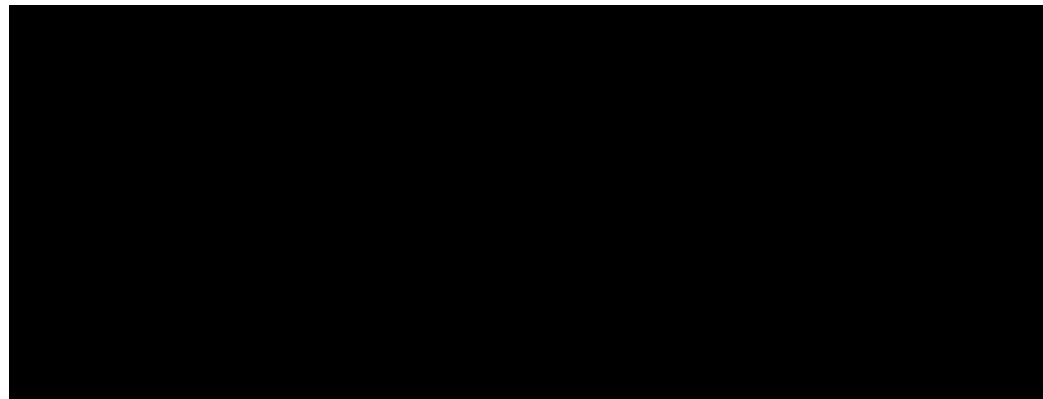
March 2018

Department of Mechanical and Aerospace Engineering  
Monash University

*For Peter and Alice*

## **Statement of Originality**

This thesis contains no material that has been accepted for the award of a degree or diploma in this or any other university. To the best of the candidate's knowledge and belief, this thesis contains no material previously published or written by another person except where due reference is made in the text of this thesis.



---

Candidate: Daniah Saleh Hajji Aljubaili

March 2018

## **Notice**

©Daniah Aljubaili. Except as provided in the Copyright Act 1968, this thesis may not be reproduced in any form without the written permission of the author.

*“Long gone I laugh and go for another  
round”*

Kissin' Dynamite, 2016

## Abstract

A combined numerical and experimental study of the turbulent flow past elliptical cylinders is presented. The study focuses on the Reynolds number ( $Re$ ) of 3900, which, for a circular cylinder, has become a benchmark problem for Large Eddy Simulation (LES) models. This Reynolds number is beyond the range at which Kelvin-Helmholtz vortices are observed in the separating shear layers, but considerably below the drag crisis range that begins at  $\sim O(Re^5)$ . Thus, it provides a good test for CFD codes that aim to reproduce time-dependent turbulent wake flows.

This research investigates the capability of different LES-type models to successfully reproduce the change in the wake behaviour as the cylinder geometry is smoothly varied. Past studies, albeit at considerably lower Reynolds number, have indicated that the wake state alters considerably as the aspect ratio of an elliptical cylinder is varied. In particular, the lower  $Re$  simulations show that the wake formation length shortens, the vortex shedding becomes more intense and the Kármán vortex shedding is replaced in the near wake by vortices forming into two offset layers. Of course, this body type includes the circular cylinder, which has motivated the current study.

For a circular cylinder, two different LES models were examined: the Wall Adapting Large Eddy (simulation) (WALE) approach, and the Improved Delayed Detached Eddy Simulation (IDDES) approach. Both models performed reasonably well in comparisons with previous experimental and numerical studies in the prediction of the surface pressure distribution, and velocity and turbulence characteristics in the wake. Experiments using Particle Image Velocimetry (PIV) were also undertaken to capture the wake characteristics, both to provide a comparison for the simulation predictions, but also to provide confidence in the method to produce an accurate dataset for the next stage of the study on elliptical cylinders.

The research was then extended to elliptical cylinder wakes. Moving from a circular cross-section to an elliptical one results in a substantial change to the drag coefficient and the surface pressure distribution. For an aspect ratio ( $AR$  = streamwise to cross-stream axis ratio) of 0.1, the drag coefficient was predicted to be approximately twice as large as for a circular cylinder ( $\sim 1.9 : 1.0$ ). An examination of the wake revealed that reducing the aspect ratio from  $AR = 1$  to 0.67 resulted in a considerable shortening of the mean recirculation bubble. Moving to lower aspect ratios resulted in this bubble length increasing again. The changes to the wake measured by time-mean

velocity and Reynolds stress fields have been quantified and compared with the fields obtained by PIV. Overall, a good match to the experimental results was obtained, with the general trends and variations of the distributions comparing well.

## Acknowledgements

For their support and guidance throughout the entire duration of my candidature, I would like to thank my supervisors, Professors Mark Thompson and Kerry Hourigan, whose expertise and enthusiasm for the subject of fluid mechanics was beyond inspiring.

I would also like to give special thanks to Jisheng Zhao for helping to implement the PIV experiments for this study and overall support.

I am grateful to the department of Mechanical and Aerospace Engineering, Monash University, for providing the office space and resources necessary for the completion of this study.

Furthermore, I would like to thank the National Computational Infrastructure (NCI) for providing access to their high performing computing facility.

Thank you also to Jane Moodie and Lilian Khaw for suggesting very helpful structural improvements to the thesis in the beginning and final stages of its preparation.

I would also like to express gratitude to the Saudi Cultural Mission (SACM) for providing a scholarship in order to complete my studies. Without you this would not have been possible.

My thanks also to my colleagues Siavash Maleki, Shibo Wang, and Daniel Tudball-Smith for your assistance and suggestions with all technical aspects for ANSYS.

Thank you to the remaining of my fellow colleagues Terence Avadiar, Farah Houdrouge, Matthew Corallo, Shian Chi, Cindy Huang, Tim Crouch, James Bell, Tom McQueen, Daniel Dehtyriov, Stephen Terrington and Jordan Dunlop for your ongoing encouragement and support in my journey.

I would like thank my family for understanding my absence in order to pursue what is right for myself and support for the ongoing journey, especially, my sister Alya for her ongoing wisdom and emotional support. Your charisma inspires me everyday.

I would also like to thank Monash Motorsport for the emotional support and plenty of chats and laughter throughout challenging times (in no particular order), Besmellah Rahimi, Sam Wilson, Josh Murfet, Zac Freeman, Paul Hendy, Yuwei Cai, Shannon Chen, James Robertson, Reece Day, Aryaman Pandav, Vincent Chu, Ruth Li, Peter Bell, Daniel Crowe, Daniel Crouch, Liam Roche, Daniel Kobiela, Senal Rajapakse, Anesu Kusangaya, Neil White, Andrew Davis, Adrian Grosso, Miguel Arrieta, Justin Green,

Steph McDonald, Lachlan Palmer, Matthew Lane, Rosanne Chan, James McCutcheon.

I would also like to express gratitude to my mentors professionally and in life, Peter Light and Alice Bouribon for being like family during my stay in Australia. your guidance, values are inspiring and always challenging me to become better everyday. Also my Australian uncle Glenn Barker for being a genuine friend and uncle to me alongside always continuously supporting my journey.

I also would like to thank the many group fitness friends that have provided emotional support throughout this journey through team-teaching group fitness classes and being open for me to chat about anything I needed (in no particular order), Jake Cherry, Jye Curwood, Aidan Lucadou-Wells, Christelle Schaung, Penny Palman, Josh Wilms, Gerry Sharman, Laura Dube, Kirsty McGrath, Steve Cavell, and of course, my members in my classes.

Finally, thank you to my brothers from Germany for their understanding and support during very difficult times while pursuing success in life, Johannes Braun, Andreas Braun, Jim Müller, Steffen Haile, Andreas Schnitzer.

# Nomenclature

---

$a$	Streamwise semi-minor axis length
$AR$	Aspect ratio = $b/a$
$b$	Cross-stream semi-major axis length
$B$	Domain blockage ratio (chosen as 1/60)
$C_D$	Drag coefficient
$C_L$	Lift coefficient
$C_p$	Pressure coefficient
$D$	Circular cylinder diameter
$L$	Recirculation bubble length
$L_Z$	Spanwise length of the cylinder
$N_Z$	Number of cells in the spanwise direction
$N$	Number of cells in spanwise planes
$Re$	Reynolds number
$St$	Strouhal number
$U_\infty, U_0$	Upstream flow speed
$U', V', W'$	Fluctuating streamwise, cross-stream & spanwise velocity components
$\overline{U'V'}$	$XY$ Reynolds stress component
$U, V, W$	Streamwise, cross-stream & spanwise velocity components
$x, y, z$	Streamwise, cross-stream & spanwise directions
$\Delta t$	Timestep
$\theta$	Azimuthal cylindrical polar coordinate
$\mu$	Fluid dynamic viscosity
$\mu_t$	Turbulent eddy viscosity (dynamic)
$\rho$	Fluid density
$\nu$	Fluid kinematic viscosity
$\nu_t$	Turbulent eddy viscosity (kinematic)

# Contents

<b>1 Problem overview</b>	<b>2</b>
1.1 Turbulent cylinder wakes . . . . .	2
<b>2 Literature review</b>	<b>4</b>
2.1 Flow around cylindrical bodies . . . . .	4
2.1.1 The importance of studying the flow around circular cylinders . . . . .	5
2.2 Different simulation methodologies . . . . .	5
2.2.1 Direct Numerical Simulation (DNS) . . . . .	5
2.2.2 Reynolds-Averaged Navier Stokes (RANS) models . . .	6
2.2.3 Large-Eddy Simulation (LES) . . . . .	8
2.2.4 Hybrid RANS/LES models . . . . .	10
2.2.5 Summary on turbulence modelling of circular cylinder wakes . . . . .	13
2.3 Flow around elliptical cylinders . . . . .	13
2.3.1 Experimental investigations of elliptical cylinders wakes at various Reynolds numbers . . . . .	14
2.3.2 Numerical investigations of elliptical cylinders in 2D .	15
2.3.3 Numerical Investigations of elliptical cylinders in 3D .	16
2.4 Summary . . . . .	16
<b>3 Methodology</b>	<b>18</b>
3.1 Computation of the turbulent flows past cylindrical bluff bodies	19
3.2 Turbulent flow models . . . . .	19
3.2.1 Improved Delayed-Detached Eddy Simulation (IDDES)	20
3.2.2 Wall Adaptive Local Eddy (Simulation) model (WALE)	23
3.3 Domain size . . . . .	24
3.4 Boundary conditions . . . . .	25

3.5	Construction of the domain . . . . .	26
3.6	Grid resolution study . . . . .	28
3.7	Temporal resolution . . . . .	29
3.8	Experimental methodology . . . . .	30
3.9	Chapter summary . . . . .	35
<b>4</b>	<b>The circular cylinder</b>	<b>37</b>
4.1	Circular cylinder simulations and experiments . . . . .	37
4.1.1	Visualisation of the flow . . . . .	38
4.1.2	1D turbulent energy spectrum . . . . .	39
4.1.3	Aerodynamic force components . . . . .	40
4.1.4	WALE and IDDES predictions . . . . .	41
4.1.5	Grid sensitivity . . . . .	50
4.1.6	Sensitivity to spanwise domain length . . . . .	53
4.1.7	Comparison with experiments . . . . .	56
4.2	Chapter summary . . . . .	65
<b>5</b>	<b>The elliptical cylinder</b>	<b>66</b>
5.1	Chapter overview . . . . .	66
5.1.1	Varying the aspect ratio . . . . .	66
5.1.2	Wake shedding patterns . . . . .	78
5.1.3	Experiments based on PIV . . . . .	79
5.2	Field comparisons between experiments and simulations . . . . .	86
5.2.1	Streamwise velocity comparisons . . . . .	86
5.2.2	Cross-stream velocity comparisons . . . . .	87
5.2.3	$\overline{U'V'}$ Reynolds stress comparison . . . . .	88
5.3	Chapter summary . . . . .	89
<b>6</b>	<b>Conclusions and future work</b>	<b>91</b>
6.1	Summary of key findings . . . . .	91
6.2	Contribution of the thesis . . . . .	91
6.3	Possible future work . . . . .	92
<b>References</b>		<b>93</b>

# Chapter 1

## Problem overview

This chapter provides an introduction to the current research project providing a context against past studies.

### 1.1 Turbulent cylinder wakes

The flow around circular, and less symmetric, cylinders has been a much studied problem for well over a century. This is due to its extensive applications to real-world engineering problems, such as flows around bridge cables, television towers, deep-sea risers and oil platform legs, power-station chimneys, and even landing-gear systems, to provide a few examples. A key feature of interest when studying these flows is the appearance of large-scale vortex shedding in the wake region behind the body.

Vortex shedding is characterised by the Strouhal number ( $St$ ), which is the shedding frequency normalised by the cross-stream dimension ( $D$ ) and the upstream flow velocity ( $U_\infty$ ):  $St \equiv fD/U_\infty$ . When the frequency of shedding matches the natural oscillation frequency of the body, this may lead to resonance, possibly resulting in structural damage. Therefore, it is important to consider vortex shedding when examining flow-structure interaction problems.

Over the years there have been many experimental and numerical studies concerning the flow past circular cylinders. In the fully turbulent regime, these studies include experimental research by Norberg (1987), Ong and Wallace (1996), and Lourenco and Shih (1994), and many numerical studies since then including Kravchenko and Moin (2000), Mittal and Moin (1997),

Beaudan and Moin (1994), and Parnaudeau et al. (2008), and indeed many others. From the point of view of numerical modelling, over the years, these studies have evolved from a focus on low-Reynolds number laminar flow to transitional and even turbulent flow around the circular cylinder, as computational resources and availability have improved. Indeed, one particular case that has received considerable attention is flow past a cylinder at  $Re \equiv U_\infty D/\nu = 3900$ , where  $\nu$  is the kinematic viscosity. This case has taken on benchmark status for LES modelling. In addition, such studies have inspired investigations into more complex cylinder shapes such as square cross-sections and elliptical bodies. In terms of the current research program, numerical and experimental studies on the flow past elliptical bodies have been undertaken in the laminar regime. However, as far as the author is aware, only limited attempts have been made to study this body type at higher Reynolds numbers where the flow is fully turbulent.

Therefore, the main aim here is to study the behaviour of the flow past elliptical cylinders in three dimensions under high Reynolds number turbulent conditions, and in particular for  $Re = 3900$ , for which there are both previous numerical and experimental results for comparison for the limiting circular cylinder case. In the following chapters, the methodology and results are validated against the benchmark case of the circular cylinder before attempting to simulate the flow past elliptical cylinders. Five different aspect ratios were used:  $AR \equiv b/a = 0.1, 0.25, 0.5, 0.67, 1$ , to investigate the change to the wake as the cylinder aspect ratio is progressively decreased. Here,  $b$  and  $a$  are the streamwise (semi-minor) and cross-stream (semi-major) axis lengths, respectively, thus  $AR = 1$  for a circular cylinder and  $AR = 0$  for a normally aligned flat plate. As indicated, these simulations included the circular cylinder case, to use as a reference case for a differential analysis.

In this thesis, the following chapter provides a short review of previous relevant studies for the flow past circular and elliptical cylinders. In Chapter 3, the experimental and numerical methods applied are briefly outlined, with further details provided in related journal articles. Chapter 4 reports the numerical and experimental results for the case of the circular cylinder to provide evidence that the methodology and predictions compare satisfactorily with previous benchmark studies. After this, results from simulations and experiments of the flow past elliptical cylinders are presented in Chapter 5. That chapter summarises the effect of aspect ratio on elliptical cylinder wakes. Chapter 6 concludes with the key findings from the current study, and provides a brief perspective on the current work.

# Chapter 2

## Literature review

This chapter focuses on past experimental and numerical studies on the flow around a circular cylinder at various Reynolds numbers, but particularly at  $Re = 3900$ , to which the current study is directed. The review also covers the numerical methods and methodologies used in these past studies. Finally, previous investigations into the flow past elliptical cylinders are reviewed, identifying remaining open areas for investigation.

### 2.1 Flow around cylindrical bodies

There has been extensive works documenting the behaviour of the flow past circular cylinders over many decades. These include classical works of Roshko (1993), Bishop and Hassan (1964), Williamson (1996), Fornberg et al. (1979), Norberg (1987), Lugt and Haussling (1974), Mittal and Raghuvanshi (2001), Ong and Wallace (1996), and many others. The contributions of some of these and other references will be established below. Beyond an isolated cylinder, many other flow problems based on this bluff body geometry have been investigated, and these include the works on cylinders in tandem, the addition of a secondary cylinder to observe the behaviour of the primary cylinder wake, as well as the introduction of a wide diversity of cross sections in steady and unsteady Reynolds number conditions, the introduction of porous cylinder surfaces, and cylinders under forced and free vibration. However, this literature review concentrates on previous research only focusing on the flow past an isolated circular cylinder. There have been numerous numerical and experimental investigations of circular bodies using different

methods. This review will highlight the importance of studying the flow around such a bluff body as well as to highlight the simulation methods used to date. The last section discusses previous studies on the flow around elliptical bodies, which is the main research focus of the current study.

### **2.1.1 The importance of studying the flow around circular cylinders**

Apart from its intrinsic theoretical worth, it is important to study the flow around bluff bodies to understand the expected flow behaviour during design stages of industrial developments, such as fluid-structure interaction for bridges and deep-sea risers, and offshore oil platform legs, to provide a few examples. An important flow problem that has been investigated widely over the last few decades has been the flow around circular cylinders at  $Re = 3900$ . This is because this Reynolds number is sufficiently high for the flow to be fully turbulent, yet low enough so that both good quality experimental results are available, and numerical simulations using Large Eddy Simulation approaches, and even Direct Numerical Simulation (DNS), are possible. The Reynolds number is large enough to expect Kelvin-Helmholtz vortices to form in the separating shear layers. The following sections describe in more detail a plethora of numerical and experimental research studies over the past decades.

## **2.2 Different simulation methodologies**

There have been many numerical methods developed that can successfully simulate three-dimensional flows. These methods have evolved from directly solving the Navier Stokes equations to predict the flow field using different turbulence models. This section reviews these different approaches discussing their advantages and disadvantages. This section also reviews previous studies that have utilised each of these methods.

### **2.2.1 Direct Numerical Simulation (DNS)**

Direct Numerical Simulation (DNS) has become more important for flow problems with complex geometries as computer power and memory size have

increased. DNS refers to solving the Navier-Stokes equations directly numerically by resolving all spatial and temporal scales down to where viscous dissipation extracts flow energy from the system. Dong et al. (2006) utilised DNS to investigate flow around a circular cylinder at  $Re = 3900$  (and 10 000) to study the development of the shear-layer instability. This method provided accurate measurements of the flow parameters such as the velocity fluctuations and Reynolds stresses when compared with their own experimental results and previous studies. These predictions were obtained using an unstructured spectral-element Fourier code, allowing very high resolution in the separating shear layers. More recently Gsell et al. (2018) used a commercial code to produce DNS predictions for this same case, again making comparisons with experiments. Typically these simulations used extremely large mesh sizes to resolve the small turbulent length scales. It is not entirely clear that either simulation fully captured the smallest turbulent scales in the wake, but in any case, enough of the turbulent spectrum was captured to give predictions that were a very good fit to experimental results. Naturally, DNS has some advantages and disadvantages. The main advantage is that there is no extra modelling, all scales are captured directly by having a grid fine enough to resolve turbulence down to the Kolmogorov scale. However, this is also the main disadvantage, in that the computer resource requirements are very high. Indeed, DNS requires massive computational power (Kurien and Taylor, 2005). Therefore, it is an impractical method to use for industrial turbulent flows (Luo et al. 2014) at present, for which Reynolds numbers are generally even higher.

### 2.2.2 Reynolds-Averaged Navier Stokes (RANS) models

Another approach to predict the flow around bluff bodies is through employing turbulence models to incorporate the effective diffusion of turbulence on the mean flow. Reynolds-Averaged Navier Stokes (RANS) turbulence models have been used to predict the time-mean flow behaviour of bluff body wakes. An example is the work of Rahman et al. (2007), who used RANS to predict the mean drag and lift forces around a circular cylinder at  $Re = 3900$ . However, accuracy of the mean force components was very difficult to achieve using this approach. Rajani et al. (2015) drew the same conclusion when they simulated flow past a circular cylinder in the range  $10^4 < Re < 10^7$  us-

ing *Unsteady RANS* or URANS. This approach adds in the time-derivative terms in the Navier-Stokes equations, allowing a time-dependent solution to be predicted. Since URANS only captures the largest length scales in the flow and is only likely to capture low frequency oscillations of a globally unstable flow, one might expect this to be at most a crude approximation. In that study, it was found that URANS computations were inadequate for good predictions of the drag coefficient, Strouhal number and fluctuating lift coefficient over the entire  $Re$  range.

Ong et al. (2009) investigated high Reynolds number flows in the transcritical and supercritical Reynolds number regimes over a circular cylinder using unsteady RANS. The focus of this study was to evaluate if the model was applicable for design under these flow conditions. It was found that the model produced some inaccuracies due to anisotropy of turbulence in such high flows. Shur et al. (2005) investigated the accuracy of unsteady RANS in two- and three-dimensions for the case of a circular cylinder. They found that three-dimensional URANS predicted the flow field more accurately over two-dimensional URANS, and that it was far less costly than other models, such as Deattached Eddy Simulation (DES). Senocak et al. (2007) highlighted the issues of URANS by simulating the flow past a square cylinder. It was found that in regions of low eddy viscosity, the flow field can be under resolved in RANS computations. This consequently causes sensitivities such as the numerical solution being dependent on the grid distribution, causing grid-independence to be difficult to obtain. Rodi (1997) presented a comparison between different models employing URANS and LES past bluff bodies. The comparison of the numerical and experimental results showed that the predictions were not satisfactory, even though some flow features were captured better in some models than others. There have also been many other studies that have shown URANS to give poor predictions of the drag and lift forces for bluff bodies. Examples include the work of Lübecke et al. (2001) and Rodi (2002). Some of these studies have been successful at predicting flow field features around bluff bodies. However, URANS was generally found to be not reliable for predicting force coefficients: URANS tends to over-predict these parameters. Finally, the accuracy of URANS also depends on the engineering application that it is applied to. For time-dependent turbulent flows, the preferred approach is to use the much more expensive method known as Large Eddy Simulation (LES) described in the next section, although this approach is still very expensive for industry-type problems.

### 2.2.3 Large-Eddy Simulation (LES)

Post-dating the development of RANS, another turbulence model emerged known as Large-Eddy Simulation (LES). LES aims to directly calculate the large turbulent spatial and temporal scales, with the effect of the finer scales on the larger scales modelled, in order to reduce the grid requirements of DNS (Luo et al. 2014). Thus, LES uses *subgrid-scale models* (SGS) to achieve this aim. Sidebottom et al. (2012) performed computations of the flow past circular cylinders at  $Re = 3900$  numerically, using LES based on two different subgrid-scale models. These were the standard Smagorinsky model and a one-equation eddy viscosity model. The purpose of this study was to compare these models in the prediction of the key flow parameters at this turbulent Reynolds number. The results based on the Smagorinsky model had significant errors; however, the one-equation eddy-viscosity model provided better predictions. This was especially true near the separation point of the cylinder, even though a shorter separation zone was predicted. The Smagorinsky model also failed to accurately predict the minimum streamwise velocity in the wake region.

One of the most important contributions to LES was the development of the Dynamic Smagorinsky Model (DSM) by Germano (1992). This is because it eliminates a key drawback of the Smagorinsky model. That drawback is that the coefficient of the Smagorinsky model defining the level of the subgrid-scale eddy viscosity needs to be preset as a constant in space and time (Meneveau and Katz, 2000). The advantage of DSM is that this coefficient can be determined dynamically using the Germano identity based on scale invariance. Essentially, the varying constant is determined by double filtering the solution as described in Meneveau and Katz (2000). Kravchenko and Moin (2000) used large-eddy simulation models (LES) based on (i) a dynamic subgrid-scale (SGS) model, (ii) a standard Smagorinsky model and (iii) without the use of an SGS model, to predict key flow parameters. The predictions were in better agreement with previous studies using the dynamic SGS model compared to no model; however, the effect of the model did not improve the results significantly. Park et al. (2006) also utilised the dynamic model for the circular cylinder case and concluded it performed better compared to the Smagorinsky model, but the differences were not significant. Parnaudeau et al. (2008) used LES with fine grids to predict the flow around a circular cylinder and compared their predictions with experimental results they also obtained. Indeed, the match with experimental velocity and Reynolds stress

component profiles in the wake was surprisingly good. Rajani et al.(2015) also used LES coupled with a dynamic SGS model to study the complexity of the three-dimensional flow structure around the circular cylinder. It was found that the LES results generally agreed well with experiments; however, the predictions became less accurate in the far wake region, especially for predictions of the streamwise velocity. It was also found that the use of the dynamic SGS model resulted in better agreement with the measured data from previous literature for the mean and fluctuating quantities, but the difference was insignificant when compared to the results using the standard Smagorinski model. This suggests that the use of a dynamic sub-grid scale model is not found to be particularly advantageous. However, in practice, since predictions are strongly dependent on the Smagorinski constant and this changes for different flow problems, DSM, which automatically adjusts the constant, still has definite advantages.

Another type of LES model is the Wall Adaptive Large Eddy (WALE) simulation model. WALE is a modified LES model that overcomes some of the deficiencies of the standard SGS model. This is because WALE produces almost no eddy-viscosity in wall-bounded flows and therefore is capable of reproducing laminar to turbulent transitions. There are several studies using WALE, such as Sarabandi and Moghadam (2016) who investigated three-dimensional flow around a finite circular cylinder standing on a flat plate. The results showed that WALE was able to capture strong tip vortex structures, but when compared with another model, (in this study, zonal-DES), the structures were created sooner compared to zonal-DES. However, overall, the predictions were very similar between the two models. Wornom et al. (2011) investigated the capabilities of WALE by studying its performance for a circular cylinder at  $Re = 3900, 10\,000$  and  $20\,000$ . It was found that WALE was able to correctly reproduce the local surface pressure distribution, the bubble formation length and the Strouhal number alongside other parameters. There were small discrepancies observed at  $Re = 10,000$  and  $20,000$ , but this appeared to be due to a lack of resolution. Parsani et al. (2010) obtained encouraging results using the WALE model, even though that study was restricted to a two-dimensional model. However, when applied to three-dimensional flows, WALE could provide more insight into the flow behaviour qualitatively and quantitatively.

One of the drawbacks of LES is that in order to compute highly turbulent flows, considerable computational power is still required. This is especially true in the boundary layer, where the number of grid points required

to resolve the important boundary layer structures is a strong function of Reynolds number. In fact, for LES, the number of grid points is effectively equivalent to that required by DNS (Luo et al. 2014). However, for the flow past a circular cylinder, the main focus is on the wake, for which the strong mesh resolution requirement is lessened even at higher Reynolds number.

There have not been many studies that have used WALE to simulate the flow past a circular cylinder at  $Re = 3900$ , although other applications have shown that it is an effective model to use. In the current study, WALE is one of the two LES-type models used for prediction. The other is the Improved Delayed Detached Eddy Simulation (IDDES), which is discussed below. Because the WALE model tries to resolve all important scales, both in the boundary layer and wake, it is the main model used in this thesis to investigate the flow around both circular and elliptical cylinders.

#### 2.2.4 Hybrid RANS/LES models

Hybrid RANS/LES models have been proposed in recent years and this approach combines the advantages from RANS and LES to solve these complex flows at an affordable computational cost (Fröhlich and von Terzi, 2008). The use of hybrid RANS/LES is better than RANS because the hybrid approach is able to predict anisotropy effects over resolved large scales. In addition, LES is employed with fine grids only in the sections where it is required to capture the turbulent flow unsteadiness and smaller length scales for accurate statistics. One of these hybrid models is Detached Eddy Simulation (DES), which was proposed by Spalart and Shur (1997). DES was designed to treat the whole boundary with RANS and apply LES in the regions far from solid surfaces (Luo et al., 2014). This is achieved via the original DES formulation, which is based on the eddy-viscosity RANS model by modifying the length scale to achieve LES behaviour (Spalart and Allmaras 1994). Romero-Gomez and Richmond (2016) validated DES using the case of the circular cylinder at  $Re = 3900$  to test the influence of time-averaging versus eddy-resolving approaches. It was shown that DES provided a full description of the flow field and could be applied to more complex engineering applications with a relatively low computational cost. Another study using DES was by Elbatran (2016) on the flow around a circular cylinder to predict the flow visualisations at  $Re = 43\,000$ . The results for Elbatran's study reveal that DES is certainly superior compared to pure LES for predicting the flow characteristics around this bluff body. In addition, DES has managed to provide

accurate flow visualisations with less computational effort compared to LES (Elbatran 2016).

Nguyen and Nguyen (2016) utilised DES for the same case and demonstrated that DES provided good accuracy in capturing unsteady vortex shedding, with excellent predictions of different flow parameters such as the pressure distribution and velocity fields. This showed that DES has a good potential to be used for more complex problems. Bai et al. (2016) assessed the capability of DES, and compared the predictions and experiments for a circular cylinder. DES adequately predicted the drag coefficient and Strouhal number using a coarser grid than LES or RANS. This model also captures the development of the Kármán vortex street, indicating that DES is capable of simulating the flow around bluff bodies which experience large separations. In contrast to these studies, Hong et al. (2014) utilised DES for the same case and found that DES performed poorly in its prediction of the fluctuating structures in the near wake of the body because of the RANS solution close to the cylinder surface. Sorensen et al. (2011) used DES to study the flow past a circular cylinder at  $Re = 10^6$  to see if DES was capable of predicting the complex high-Reynolds number flow separation. In their study, the computations showed good quantitative and qualitative agreement with previous experiments (Sorensen et al. 2011). The most interesting point from that study was that DES is not only capable of predicting the flow separation, but also turbulent reattachment and separation, compared to RANS models. D'Alessandro et al. (2016) simulated the flow past a circular cylinder at  $Re = 3900$  using DES to investigate this model's capabilities. In that study, it was found that DES managed to predict the flow parameters accurately when compared to other studies in the literature.

Although there have been a number of studies using DES, it is worth noting that this model has some issues in relation to practicability. The first one is *Grid-Induced Separation* (GIS), which was a problem reported by Menter et al. (2003). GIS is an artificial separation that occurs during the change from RANS to LES due to the introduction of a sudden grid change in grid refinement in the overlap region. *Modelled-Stress Depletion* (MSD) is another issue, which is caused by insufficient flow instability during the switch from RANS to LES. MSD refers to the reduction of eddy viscosity when switching from RANS to LES without a corresponding balance by resolved turbulent content (Spalart et al. 2006). Since the effect of GIS also occurs without resolved turbulent content, GIS is a result of MSD (Spalart et al. 2006).

In an attempt to eliminate these disadvantages, Spalart et al.(2006) created a new version of DES-referred to as *Delayed-Detached Eddy Simulation* (DDES) that was based on a simple modification to the DES formulation. There have been several studies using DDES. Constant et al. (2017) used DDES to study the flow around a circular cylinder between  $30 < Re < 3900$ . The analysis of the main flow features indicate a very high level of precision in the flow prediction especially in the shear layers in the near wake. In addition, the drag and lift coefficients are in agreement with numerical and experimental data from the literature. Another study by Lee et al. (2014) used DDES to investigate a self-oscillating cylinder at  $Re = 5000$ . This resulted in very good agreement with other computations from past studies on fluid-induced vibration of cylinders due to vortex-shedding. DDES offers many advantages such as ability to handle flows that experience massive separation, which can be tackled at low computational cost (Travin et al. 2000). Another advantage is that it does not produce GIS, which was the original problem of DES. Even though DDES has many advantages, some issues still remain. For example, the issue of *log-layer mismatch* (LLM) has not been resolved by DDES. Another of these hybrid RANS/LES models is known as Improved Delayed-Detached Large Eddy Simulation (IDDES), which offers an improvement to DDES. Xiao and Luo (2014) utilised IDDES for simulating the flow around three cylinders in tandem, overcoming several shortcomings such as grid induced separation (GIS) and log-layer mismatch, and found the performance superior to that of DDES. Weinmann et al. (2014) used a hybrid RANS/LES model for cylinders in tandem. It was expected that this hybrid model would improve the overall quality of the predictions. Indeed, it was found that this model provided the best agreement of the flow field, in addition to requiring only a relatively coarse mesh. Recently, D'Alessandro et el.(2016) produced a series of simulations of the circular wake at  $Re = 3900$  based on a number of variants of the IDDES model and different grid sizes, documenting the expected performance as modelling components changed. Due to the advantages that IDDES offers, this will be adopted as one of the simulation approaches for this study, in addition to the WALE model.

### **2.2.5 Summary on turbulence modelling of circular cylinder wakes**

In summary, there has been extensive research undertaken on the flow past circular cylinders at  $Re = 3900$  using a series of different turbulence modelling approaches: RANS, LES, DES and DDES. However, these methods have limitations as discussed above. Although the use of RANS models can capture the drag and lift coefficients accurately, RANS is poor when resolving the 3D flow structures in the wake of the body. By contrast, LES models need a much higher resolution but can resolve the wake structures well. However, the larger computational cost of LES needs to be considered. Using DES somewhat reduces the computational cost of resolving the boundary layer flows, whilst providing accurate predictions of wakes; however, new problems emerged. One of these problems is Grid-Induced Separation, which occurs from the switch between RANS and LES within the model due to the introduction of a grid refinement. Another problem was Modelled-Stress Depletion, which is caused by insufficient flow instability during the RANS to LES switch. These limitations are strongly reduced using the Improved Delayed Detached Eddy Simulation (IDDES) model. Tests indicate that it provides a better quality flow field prediction for even more complex bodies. There have only been a few studies investigating the flow around a circular cylinder at  $Re = 3900$  using this approach. Hence, this study will investigate the performance of this model, together with the WALE simulation model, in chapter 4.

## **2.3 Flow around elliptical cylinders**

In contrast to the circular cylinder, there are vastly fewer past investigations on the flow past elliptic cylinders. Those studies include investigating flows past elliptical cylinders at either low or high Reynolds numbers, the effect of ellipse aspect ratio, heat transfer studies, vortex-induced oscillations around ellipses, rotational motion of these bodies, viscous flows, positioning the body at different angles of attack, and many more. The section below focuses on reviewing past studies involving this bluff-body type and identifies areas that are open for further investigation.

### 2.3.1 Experimental investigations of elliptical cylinders wakes at various Reynolds numbers

There has been a series of experimental studies of the flow past elliptic cylinders. Previous studies include the classical works of Shintani et al. (1983), Taneda (1956), amongst others. Arat et al. (2012) investigated elliptical cylinder wakes using PIV and studied the wake streamline topology for Reynolds numbers in the range  $1500 < Re < 10\,000$ . Rocha (1997) investigated flow past an elliptical cylinder of aspect ratio  $AR = 0.86$  for  $0 < Re < 1600$ , and compared the flow to that of a circular cylinder. Radi et al. (2013) performed experiments for elliptic cylinders using a large range of aspect ratios at low Reynolds numbers. The Reynolds number for these experiments was in the range  $100 < Re < 300$ . Surprisingly, this revealed the very strong effect of aspect ratio on the wake state, so that as the aspect ratio was reduced, the Kármán vortex street seen for a circular cylinder is replaced by a two layer wake. In addition, it was shown that the occurrence of different three-dimensional wake instabilities was also sensitive to aspect ratio. Gus'kuva et al. (1998) experimentally studied the hydrodynamic forces acting on an elliptical between  $Re = 0.3\text{--}10^4$ ; revealing the strong dependence of drag on the cylinder aspect ratio.

Fonseca et al. (2013) studied two different aspect ratios:  $AR = 0.33$  and  $0.67$ , using a hydrodynamic tunnel for  $Re \leq 2000$ . As part of the study, visualisations using coloured dyes were obtained, allowing the identification of the boundary layer separation, recirculation region size and vortex shedding in the wake. For the larger aspect ratio case, it was found that the behaviour of the flow was similar to that of the circular cylinder, while significant changes occurred for the smaller aspect ratio. Modi and Wiland (1970), and Choi and Lee (2000) both carried out experiments on elliptical cylinders at trans-critical Reynolds numbers. Although these experimental studies show that the influence of aspect ratio is substantial, they are limited to either low or very high Reynolds numbers. Until now there appear to be few experimental studies investigating the flow past elliptical cylinders of varied aspect ratio at moderate Reynolds numbers.

### 2.3.2 Numerical investigations of elliptical cylinders in 2D

Many of the numerical studies on flows past elliptical cylinders have investigated low Reynolds number two-dimensional flows. Johnson et al. (2004) directly simulated wake flows for  $AR \leq 1$  for  $75 \leq Re \leq 175$  to determine the changes to both the near wake and the far wake structure, showing that as the aspect ratio decreased, the Kármán wake was replaced by a two-layer wake in the near downstream region, which reverted to a longer wavelength Kármán wake further downstream. This analysis was extended by Thompson et al. (2014), who modelled the wake state to 300 diameters downstream, showing that several distinct wake states could occur as the wake structures diffused and changed the time-mean profile. In addition, the three-dimensional stability of higher aspect ratio cylinders was quite different from the mode A and B transitions occurring for a circular cylinder. Raman et al. (2013) also simulated the flow around elliptical cylinders of small aspect ratio in 2D for  $0.1 < AR < 1$  and  $50 < Re < 100$ . Sheard et al. (2007) studied these bodies up to  $Re = 500$  and Mittal and Moin (1996) simulated the flow up to  $Re = 1000$ . Dogan et al. (2013) investigated in 2D the flow characteristics at  $Re = 6500$  and found that the wake scaled on the cylinder cross-sectional diameter. Stack and Bravo (2008) investigated the wake behind two-dimensional ellipses when the aspect ratio was varied but at low  $Re$  ( $0 < Re < 10$ ) in order to find the critical aspect ratio. It was found that the behaviour of the flow was significantly influenced as the aspect ratio changed and that the critical aspect ratio decreased as the Reynolds number approaches zero. Daoud et al. (2016) investigated 2D oscillatory flow past elliptical bodies with different aspect ratios numerically. The purpose of their study was to investigate the effects of geometrical parameters on an oscillating flow field as well as the hydrodynamic forces when manipulating these parameters. The Reynolds number was set to  $Re = 100$  for that study. Although these previous studies provide some useful insight into the behaviour of the flow around an elliptical cylinder, such as the change in near wake structure with aspect ratio, they are mainly focused on two-dimensional flow.

### 2.3.3 Numerical Investigations of elliptical cylinders in 3D

Beyond these 2D investigations, there have been a number of studies investigating three-dimensional flow. Badr (1997) performed a numerical study in 3D to determine the properties of symmetrical flow for aspect ratios  $AR = 0.6\text{--}12$  in the Reynolds number range of  $500 < Re < 1000$ . Thompson et al. (2014) studied the stability of two-dimensional base flows around elliptic cylinders to determine the transition modes and critical Reynolds numbers. It was found that as the aspect ratio was decreased, the first circular cylinder transition mode (mode A) is no longer unstable for aspect ratios below  $AR = 0.25$ . This is because the wake deviates from the standard Bénard von Kármán state. Interestingly, for the  $AR = 0.25$  case, when the  $Re$  reaches  $Re = 125$ , the initially unstable mode A restabilizes, so that the wake should undergo a transition from 3D back to 2D. Gallardo et al. (2016) also studied the development of instabilities in oscillatory viscous flows past elliptic cylinders using 3D numerical simulations. These flows were investigated for aspect ratios of  $AR = 0.33, 0.5, 0.67, 0.77$  and 1 in the range over the range  $200 \leq Re \leq 1200$ . It was found that elliptic cylinders with aspect ratios  $AR = 0.67$  and  $0.77$  exhibited rib-like structures at each side of the cylinder, similar to those found for circular cylinders. When the aspect ratio was decreased to  $AR = 0.5$ , there was a shifting of the vortex pairs towards a stagnation point. An interesting feature was that when  $AR = 0.33$  and  $0.5$ , the appearance of counter-rotating vortices near the separation point of the ellipse was found occur. This was attributed to an increase in the local curvature for very low  $AR$ . Leontini et al. (2015) investigated the flow around three-dimensional elliptical cylinders for  $AR > 1$  in order to find the critical Reynolds number for three-dimensional transition. Saturated wake states were computed, showing differences from those for a circular cylinder. While these studies have considered 3D wakes, they still appear to be primarily limited to relatively low Reynolds numbers.

## 2.4 Summary

Although there have been a reasonable number of past studies on the flow past elliptical cylinders, it is clear that this body shape has not been explored to anywhere near the extent of a circular cylinder. In particular, it

appears that little research has been performed on elliptical cylinders in the fully turbulent subcritical  $Re$  regime, and in particular for the benchmark case of  $Re = 3900$ . This situation appears to be true both for experimental and numerical investigations. Thus, documenting the wake flow and aerodynamic forces on this body shape for a range of aspect ratios, through a combined numerical and experimental study, appears a worthwhile exercise. In particular, the differences in the wake structure and characteristics compared to a circular cylinder should provide good insights into the governing flow physics of the different cases. This research program uses LES-type simulations based on the WALE and IDDES turbulence models using a parallel commercial code (ANSYS Fluent) together with 2D cinematographic PIV in a cross-stream plane as the main tools to explore this problem. The methodology is outlined in the next chapter.

# Chapter 3

## Methodology

This chapter introduces the numerical techniques employed in the research programme. As described in the literature review, the *Improved Delayed Detached Eddy Simulation* (IDDES) model is one of two computational methods used to compute the turbulent flows around the cylindrical bodies under investigation. This model is an improved version of the Delayed Detached Eddy Simulation (DDES) model, which, in turn, is an improved version of the original Detached Eddy Simulation (DES) model. In section 3.2.1 IDDES is discussed in detail and its use is elucidated. The other variation of LES used is the *Wall-Adaptive Large Eddy* (WALE) model, described in section 3.2.2. The latter model is a more pure form of LES with a functional form for wall damping to satisfy the correct physics as the flow approaches the wall. In particular, it does not generate turbulence in the case of pure laminar shear and can capture boundary-layer turbulent structures. On the other hand, IDDES uses a RANS model at the wall to capture larger time and length scale features and blends this with LES away from the wall. The models are discussed in more detail in this chapter. The last section of this chapter provides a brief overview of the experimental procedures used to obtain flow characteristics in the wake, complementing the predictions of the current numerical simulations.

### **3.1 Computation of the turbulent flows past cylindrical bluff bodies**

Previous predictions of the turbulent flow past cylindrical bluff bodies appearing in the literature have employed many different turbulent models. These approaches span from Direct Numerical Simulations, for which all turbulent time and length scales are captured, to applying coarser turbulence models such as URANS, which only attempt to capture large turbulent length scales for strongly globally unstable flows (see e.g., Rahman et al., 2007; Sidebottom et al., 2012; Kim et al., 2016). At present there do not seem to have been any/many attempts to simulate the flow around a single circular cylinder using IDDES that, at least, have been widely reported. As previously stated in the literature review, this turbulence model was developed for its ability to reduce the effects of grid-induced separation, which arise from using ambiguous grids when employing DES. Using IDDES also aims to reduce the effect that arises from employing straight DES, known as log-layer mismatch, which originates from the slow development of turbulent eddies that leads to a deficient shear stress (Xiao and Luo, 2014). The current study of the flow around a circular cylinder focuses on comparing predictions from IDDES and WALE, and both with experimental results. A key point of the numerical comparison is to verify whether there is a significant difference in the numerical predictions from using the different models, for the low Reynolds number case of  $Re = 3900$ , noting that IDDES seems to be becoming a default standard for high Reynolds number flows such as flows past vehicles and trains. Only the WALE model is used for the simulation of the elliptical cylinders discussed in chapter 5.

### **3.2 Turbulent flow models**

This section describes the governing flow equations for the two models that are employed in this study: the Improved Delayed-Detached Eddy Simulation (IDDES) model and the Wall Adaptive Large-Eddy (WALE) model. The predictions from each model will be compared in the following chapter.

### 3.2.1 Improved Delayed-Detached Eddy Simulation (IDDES)

As described in the literature review, there have been many studies that used the precursors to this model: DES and DDES. However, it became clear with experience that those turbulence models had several shortcomings, such as *Grid-Induced Separation* (GIS), *Log-Layer Mismatch* (LLM) and *Modelled Stress Depletion* (MSD). IDDES combines the DDES and Wall-Modelled LES (WMLES) models, which at least partially overcomes these shortcomings. Indeed, this model has proven to have performed better than DDES in multiple studies, including the *landing gear case* considered by Xiao et al. (2013). Therefore, IDDES is one of the turbulence models chosen for this study. In terms of details, the IDDES model was created by modifying the destruction term of the Turbulent Kinetic Energy (TKE) equation. This modification was implemented by introducing a length scale,  $L_{IDDES}$ , into the TKE equation of the Shear-Stress Transport (SST) model (the RANS model used to approximate the flow near boundaries). This can be written as

$$\frac{\partial \rho k}{\partial t} + \frac{\partial(\rho k u_j)}{\partial x_j} = \tilde{P}_k - \frac{\rho k^{3/2}}{L_{IDDES}} + \frac{\partial}{\partial x_i}[(\mu + \sigma \mu_t) \frac{\partial k}{\partial x_i}], \quad (3.1)$$

where  $k$  is the modelled TKE, and the length scale  $L_{IDDES}$  is a combination of LES and RANS length scales

$$(L_{Hybrid} \equiv ) L_{IDDES} = \tilde{f}_d(1 + f_e)L_{RANS} + (1 - \tilde{f}_d)L_{LES}. \quad (3.2)$$

In this equation,  $L_{RANS}$  is the turbulence length scale of the RANS near wall model, and is defined as

$$L_{RANS} = \frac{k^{1/2}}{\beta^* \omega}, \quad (3.3)$$

and the filter length scale of the LES component,  $L_{LES}$ , is defined as

$$L_{LES} = C_{DES} \Delta. \quad (3.4)$$

Here,  $\omega$  is the turbulence dissipation and  $\beta^*$  is a constant in the SST model that takes the value of  $\beta^* = 0.09$ . Also,  $C_{DES}$  is a constant in the DES model with the value of  $C_{DES} = 0.15$ . In addition, the grid scale  $\Delta$  is defined as

$$\Delta = \min [\max (C_W \Delta_{\max} C_W D_W; \Delta_{\min}); \Delta_{\max}], \quad (3.5)$$

where  $C_W$  is a constant and  $d$  is the closest distance to the wall.  $\Delta_{\min}$  is taken as  $\min(\Delta x, \Delta y, \Delta z)$ , which is the minimum cell size in  $x, y, z$  directions. Similarly,  $\Delta_{\max}$  is defined as  $\max(\Delta x, \Delta y, \Delta z)$ . Note that compared to the DDES grid scale, the IDDES grid scale reduces the sub-grid viscosity in the log layer. The function  $\tilde{f}_d$  is defined as

$$\tilde{f}_d = \max[(1 - f_{dt}), f_B]. \quad (3.6)$$

It depends on both  $f_B$ , which is geometry dependent and  $(1 - f_{dt})$ , which is flow dependent.

In eqn (3.2), when  $f_e = 0$ ,  $L_{IDDES}$  becomes as defined in eqn (3.7), and importantly IDDES reverts to DDES. However, when  $f_e < 0$  and  $\tilde{f}_d = f_B$ , then  $L_{IDDES}$  becomes

$$L_{IDDES} = f_B(1 + f_e)L_{RANS} + (1 - f_B)L_{LES}. \quad (3.7)$$

This means that IDDES behaves similarly to WMLES near a solid wall. This occurs during the transition from RANS to LES modes. In addition, in the range  $0 < f_B = \tilde{f}_d < 1$ , where  $L_{IDDES} = L_{WMLES} > L_{LES}$ ; as a result, the eddy viscosity increases and avoids insufficiently modelled Reynolds stress (Shur et al., 2008). For additional details on the blending functions  $f_e$ ,  $f_B$ ,  $f_{dt}$ , and other parameters, refer to the paper by Shur et al.(2008).

There have been limited studies utilising IDDES to predict the flow around bluff bodies. Xiao and Luo (2014) used IDDES to investigate the flow around circular cylinders in tandem. Figure 3.1 shows the turbulent wake structure as depicted by the instantaneous Q-criterion; this shows evidence of the shear-layer instability in the upstream cylinder shear layer. In addition, other small-scale structures were observed in the wake and the gap between the two cylinders (Xiao and Luo, 2014). It was shown for the fine mesh utilised in that study, that the shear layer instability and small-scale turbulent structures showed excellent agreement with the experimental and numerical measurements from previous studies, such as Satti et al. (2011) and Jakirlic and Maduta (2012). These Q-criterion isosurface plots, reflect the effect of grid resolution. That is, a finer mesh resolves smaller-scale turbulent flow structures, as could be expected. For the coarse mesh, the shear-layer instability is delayed, and the wake structures are larger in scale than those observed in the previous investigations mentioned above.

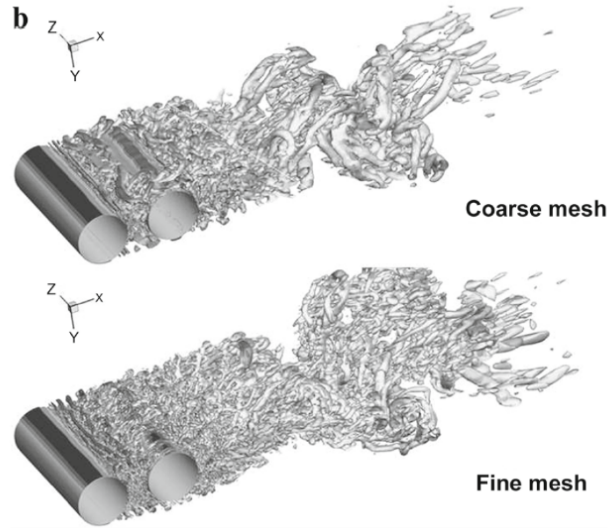


Figure 3.1: Iso-surfaces of  $Q = 1.5 \text{ s}^{-2}$  obtained from IDDES simulations of the tandem cylinder flow for a coarse and fine mesh. Reproduced with permission of Xiao and Luo 2014.

Figure 3.2 shows the pressure distributions on the two cylinders for a coarse and fine mesh. The results using IDDES for both coarse and fine meshes are in good agreement with direct experimental measurements. In addition, there is an almost insignificant difference between the pressure distributions of both meshes, despite the fact that the range of turbulent scales captured by the two grids is different. This means that the pressure force distribution on the bodies is (almost) grid-independent even with the coarser mesh.

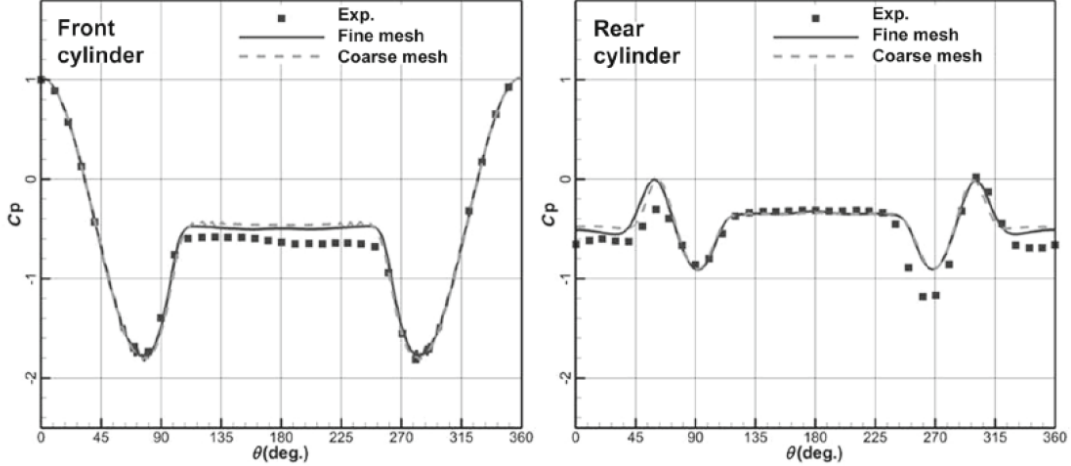


Figure 3.2: Pressure distributions on the front and rear cylinders in a tandem arrangement for both the coarse and fine meshes, and with the experimental results overlaid. Reproduced with permission (Xiao and Luo, 2014).

### 3.2.2 Wall Adaptive Local Eddy (Simulation) model (WALE)

One of the main difficulties with the standard LES model is that it does not give the correct behaviour near a wall. In practice, the turbulent viscosity needs to be damped to achieve the correct behaviour. The *Wall Adapting Large Eddy (Simulation)* (WALE) model of Nicoud and Ducros (1999) modifies the turbulent viscosity as a wall is approached to give the correct asymptotic behaviour. In addition, the WALE model uses the velocity gradient tensor to modify the behaviour near a wall. This allows a distinction between pure strain and rotation, in turn, allowing a model to be constructed that does not add turbulent viscosity for a flow with pure shear, in line with the correct physical behaviour.

The modified sub-grid scale turbulent viscosity is constructed as

$$\nu_{sgs} = (C_W \Delta)^2 \frac{(S_{ij}^d S_{ij}^d)^{3/2}}{(S_{ij} S_{ij})^{5/2} + (S_{ij}^d S_{ij}^d)^{5/4}}, \quad (3.8)$$

where  $S_{ij}$  is the rate of strain tensor and  $S_{ij}^d$  is a function of the rate of strain tensor and the rotation tensor. The functional relationships are quite

complicated and have been omitted here. As indicated this model asymptotes to zero turbulent viscosity as a wall is approached and does not add turbulent viscosity in a laminar shear flow. The constant  $C_W$  is known as the WALE model constant, which is determined by assuming that the model provides the same average sub-grid kinetic energy dissipation as the Smagorinsky model. Like the Smagorinski constant, its value can differ depending on the flow problem. However, it has been reported previously that the WALE model is not as sensitive to its constant as the Smagorinsky model (Menter, 2015), noting that the predictions from the Smagorinski model are indeed quite sensitive to the Smagorinski constant.

The greatest advantage of the WALE model is that it is more robust than the Smagorinsky model because it is based on a decomposition of the velocity gradient tensor. This means that the WALE model can detect turbulent structures with large strain and rotation rates. WALE is able to reproduce laminar to turbulent transitions (Menter, 2003).

### 3.3 Domain size

The domain size was selected mainly based on the blockage ratio  $B$ . This is a ratio of the frontal area of the body to the cross-sectional area of the computational domain, i.e.  $B = \frac{DL_z}{L_y L_z}$ , where  $D$  is the cylinder diameter, and  $L_y$  and  $L_z$  are the cross-stream and spanwise domain lengths, respectively. Ideally this ratio should be small to prevent the application of artificial boundary conditions at the cross-stream boundaries adversely affecting the solution. For the LES simulations, the blockage ratio was set to  $\sim 1\%$ . Since the current study focussed on capturing the energetically important scales of the three-dimensional turbulent flow, the spanwise length was varied in the  $z$ -direction to test the sensitivity of predictions to this length. Based on previous LES studies of the flow past a cylinder at  $Re = 3900$ , the two spanwise lengths chosen for the current study were  $L_z = \pi D/2$  and  $\pi D$ . For example, these spanwise lengths were used in previous studies by Kravchenko and Moin (2000), and it was reported that there was no significant difference in the predicted solutions of the wake flow, at least for most of the velocity and turbulence profiles investigated.

It is also necessary to specify the downstream location of the outflow boundary. This was chosen as  $L_{x,out} \simeq 10D$ , but with fine resolution only extending to  $\sim 8D$  downstream, which should be sufficient to capture the

near wake flow. This is shorter than usually prescribed to restrict the number of elements in mesh, and noting that the aim is really only to resolve the near wake—downstream to approximately  $5D$  to match the interrogation window for PIV.

### 3.4 Boundary conditions

At upstream and at the cross-stream boundaries, a constant freestream velocity of  $U_\infty$  was specified. The Reynolds number was specified based on this velocity scale and the cylinder major axis:  $Re = U_\infty L/\mu$ , where  $\mu$  is the dynamic or molecular viscosity. Here,  $L = D$  for a circular cylinder and  $L = 2b$  for an elliptical cylinder (see later).

Application of the boundary conditions is illustrated in Figure 3.3, where a pressure outlet was specified downstream of the cylindrical body, i.e., constant pressure and zero downstream velocity gradient, with symmetry conditions at the spanwise walls (not shown in figure) and a specified inflow velocity upstream and at the cross-stream boundaries of the body.

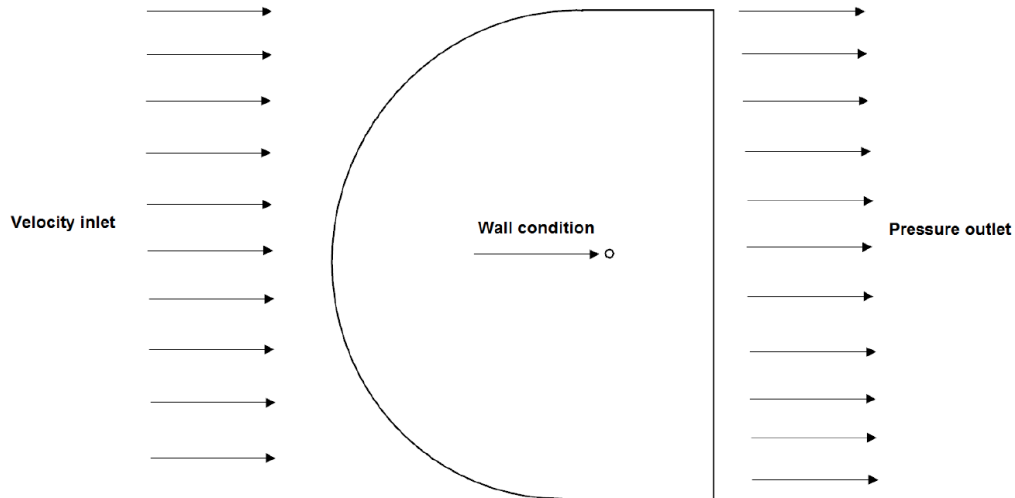


Figure 3.3: Schematic of the computational domain used with imposed boundary conditions shown. Downstream location of the outflow boundary is specified as  $L_{x,out} \simeq 10D$ . However, with finer mesh resolution, this domain was extended to  $\sim 8D$

### 3.5 Construction of the domain

The size of the domain was established based on limiting the blockage ratio to a small value, as discussed in the previous section. Figure 3.4 presents a schematic of a cross-section through the 3D mesh that was generated to study the circular and elliptical cylinder cases. The mesh created is broadly in the form of a *C-mesh*. This type of mesh has been utilised in many previous studies, such as by Catalano et al. (2003) where a C-mesh was utilised to simulate the case of a circular cylinder at  $Re = 5 \times 10^5\text{--}10^6$ . The mesh shown was constructed as a result of a number of prototype meshes, which were sequentially modified to increase spatial resolution in regions of high gradients and in the cylinder boundary layer. From the coarsest version of the mesh, the spatial resolution was increased by a factor of 2 twice, to produce the medium and fine meshes. Typically the finest mesh contains almost 7 million cells, while the medium and coarse meshes contain 1/8th and 1/64th the number of cells. One aim was to try to keep the mesh as orthogonal as possible, especially in regions of substantial velocity gradients. Note that the refinement regions are conformal in the sense that the grid points match across the block boundaries. This was done using bridging elements across boundaries, as shown in Figure 3.5. There was also an attempt to keep the spatial resolution approximately constant in the near wake region, since this is desirable for a large eddy simulation. A medium mesh was used for the initial simulations, in which the velocity field data was interpolated onto a finer mesh before restarting the simulation. Details of the medium and fine meshes are presented in Table 3.1.

For the simulations of the flow past elliptical cylinders, the cylinder mesh was transformed algebraically to convert the circular boundary to an elliptical one. This transformation also preserved grid orthogonality at the bluff body boundary in order to better capture the boundary layer, and in particular, to not add artificial diffusion in this important region. The outer boundary position is maintained under the transformation. Hence, the elliptical meshes have the same number of cells as the circular cylinder mesh. And again, there was an attempt to try to maintain reasonably constant spatial resolution in the near wake region.

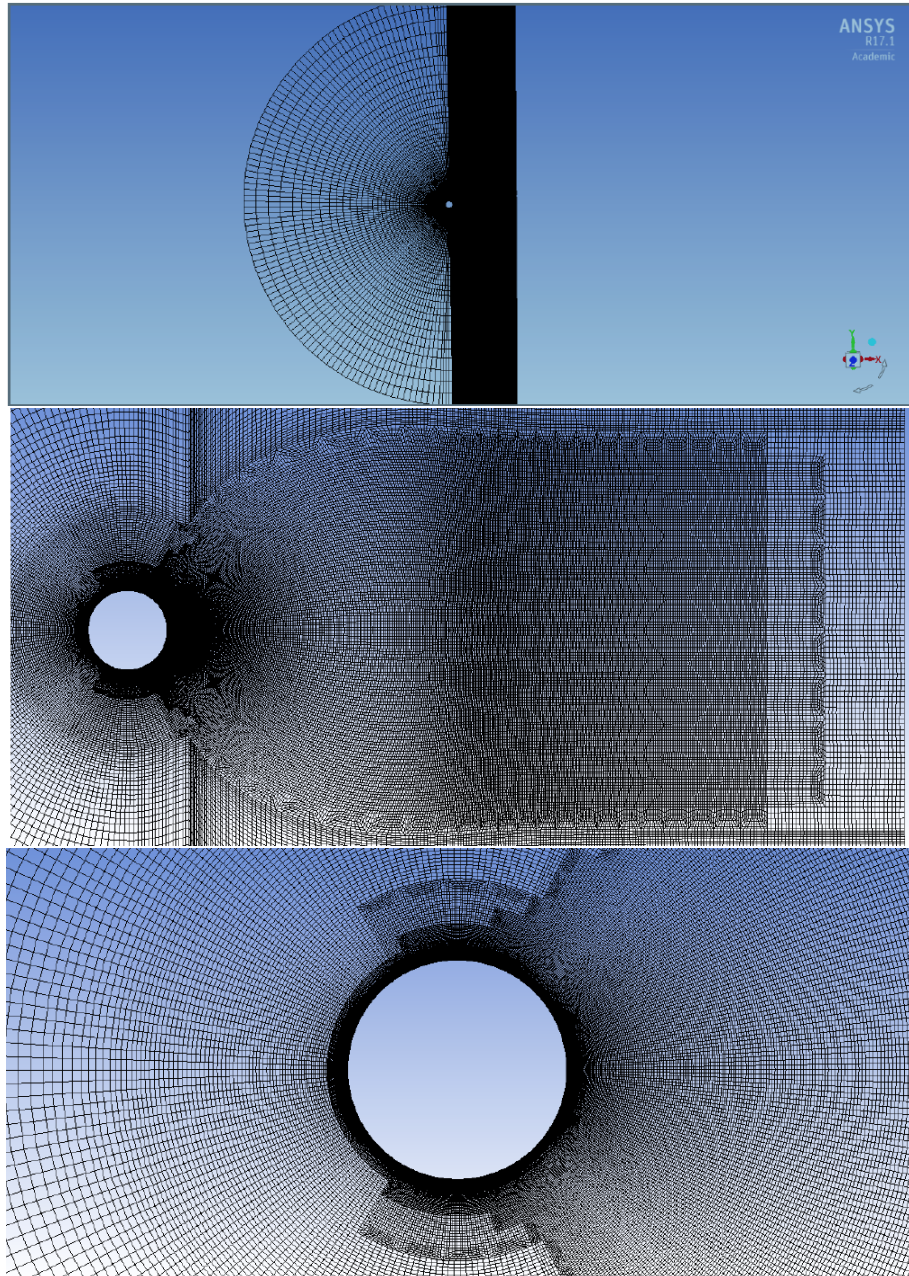


Figure 3.4: Top: Schematic of the cross-section of the mesh used in the present study. The images below are zoomed in versions showing the mesh point distribution about the cylinder and in the near wake. The mesh is extended in the  $z$  direction (spanwise) using uniform grid point spacing.

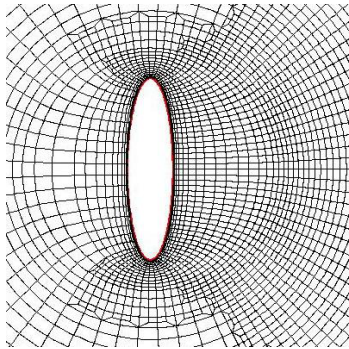


Figure 3.5: Mesh distribution around the elliptical cylinder showing how the refinement blocks are connected. This shows the coarse mesh distribution; for the fine mesh each of the cells is divided into 16 cells. Note that the mesh is orthogonal at the boundary.

### 3.6 Grid resolution study

A grid-resolution study was performed to determine whether the spatial resolution was sufficient to resolve a satisfactory range of scales to give a good approximation of the turbulent near wake at the Reynolds number considered in the study. Table 3.1 illustrates such data. The two finest grids were used in the present study. The first one (medium grid) contained 850,000 cells across the domain. The second grid (fine grid) contained  $6.8 \times 10^6$ , which had double the spatial resolution of the first grid. It can be seen that the values of the drag coefficient, Strouhal number and recirculation bubble length are maintained between each grid to within an error of  $\approx 1\%$ . These features are most dependent on solution accuracy very close to the cylinder. This suggests that the medium grid still provides a reasonable approximation of bulk flow properties. The wake turbulence statistics, such as the Reynolds stress components, are likely to require higher accuracy downstream in the near wake. Such features are examined in the results chapters that follow, including the falloff in the energy spectrum to determine how much of the range of spatial/temporal scales is captured. In addition, the resolution of the boundary layer is also examined in those chapters. The finest mesh resolution is used for the bulk of the simulations for the remainder of this study.

Table 3.1: Flow parameters from the present simulations compared to other computational and experimental studies.

Data from	Total cells	$C_D$	$L/D$	$St$
Present WALE	850 000	0.97	1.65	0.22
Present WALE	6 800 000	0.96	1.64	0.22
Present IDDES	850 000	0.95	1.75	0.21
Present IDDES	6 800 000	0.95	1.75	0.21
Mittal and Moin (1997)	19584	1.00	1.40	0.21
Beaudan and Moin (1994)	48120	1.00	1.36	0.20
Kravchenko and Moin (2000)	2 400 000	1.04	1.35	0.21
Sidebottom and Jones (2012)	1 900 000	0.89	1.19	0.18
Parnaudeau et al. (2008)		-	1.56	0.21
Khan et al. (2016)		1.61	2.26	0.21
D'Alessandro et al. (2016)	3 955 200	1.02	1.43	0.22
Norberg (1987) (exp)	-	0.98±0.05	1.4±0.05	0.21±0.10

### 3.7 Temporal resolution

A non-iterative timestepping method was used for the time integration. Since the nonlinear convective substep is explicit, the timestep has to be chosen so that the Courant number of below unity (almost) everywhere. This is also known as the Courant Friedrichs-Lowy (CFL) condition. This also ensures that the fluid does not pass through more than one cell at a time, which is required for temporal accuracy anyway. The Courant number field is calculated during the simulations. The standard timestep chosen for the fine grid simulations is  $\Delta t = 0.005D/U_\infty$ , in line with many previous simulations using a similar spatial resolution (e.g. Kravchenko and Moin 2000). This was found to lead to a Courant number less than unity across the entire domain. Note that this timestep corresponds to using approximately 1000 steps per shedding cycle.

In general, the CFL condition is a necessary, but not sufficient, condition for a numerical approximation to converge, with the CFL condition necessary for stability (Trefethen, 1994).

### 3.8 Experimental methodology

The simulation predictions were complemented with experimental results for the circular cylinder, and subsequently for elliptical cylinders. The aim of the experiments was to quantify the near wake flow, including the velocity profiles and Reynolds stress components. These experiments were conducted in the water channel of the *Fluids Laboratory for Aeronautical and Industrial Research* (FLAIR) at Monash University. Time-resolved Particle Image Velocimetry (PIV) was used to measure the time-varying 2D velocity field in  $x-y$  planes in the near wake of the body. PIV is a mature experimental method that has been used in a multitude of fluid mechanics investigations over many years. It provides non-invasive measurements of the velocity components, with the resolution determined by various factors, such as seeding density, image size, magnification, laser sheet access, etc. The current setup is described in Zhao (2012). A detailed description of the PIV technique in general can be found in Raffel (2007).

The PIV recording system used in this study employed double frames/single exposure technique alongside normalised spatial cross-correlation analysis to evaluate the acquired data (Fouras et al., 2008), i.e., determine the velocity components. Figure 3.7 illustrates the cross-correlation algorithm. The flow was seeded with small tracer particles that were close to neutrally buoyant, which can be illuminated by a thin laser sheet (see Figure 3.6).

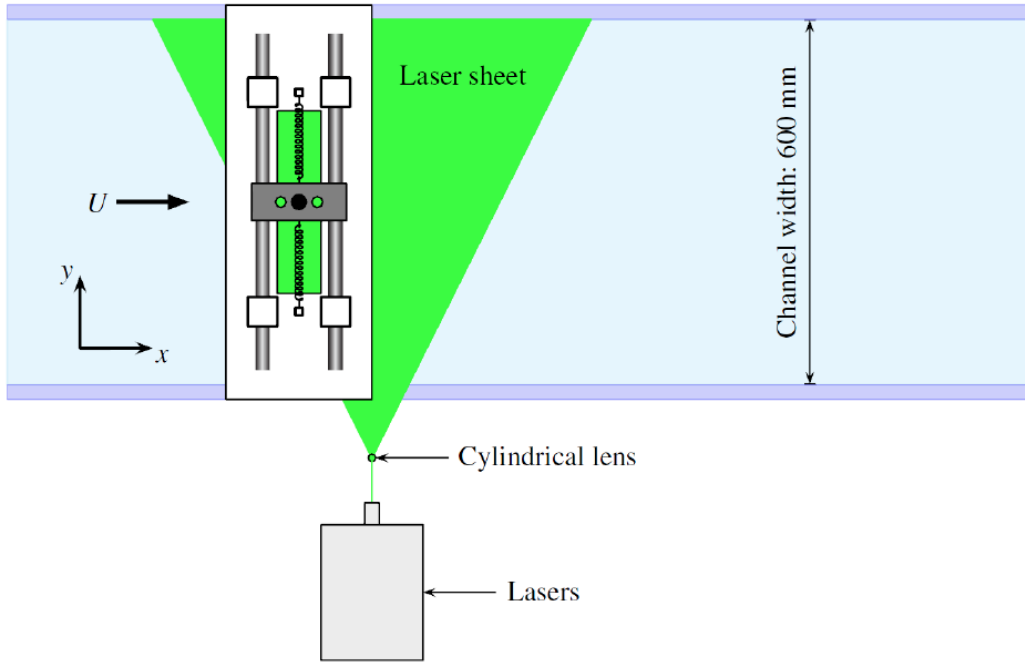


Figure 3.6: Schematic of the water channel setup where tracer particles are illuminated with laser sheet (Zhao et al. 2014). The air-bearing rig (shown) is not required for the current experiments and is simply part of the general setup. The cylinder is fixed with the long axis into the page.

A camera capable of double-frame/single exposure was coupled with a synchroniser which timed the pulsed lasers, and were both triggered at a selected sampling frequency using an external generator to record the illuminated flow region onto a series of image pairs (Zhao, 2012). Each image pair was separated in time by a short interval  $\Delta t$ . This process was illustrated in Figure 3.7. These image pairs were divided into interrogation windows and a Fast Fourier Transform (FFT) was used to calculate the cross-correlation function between each pair of windows.

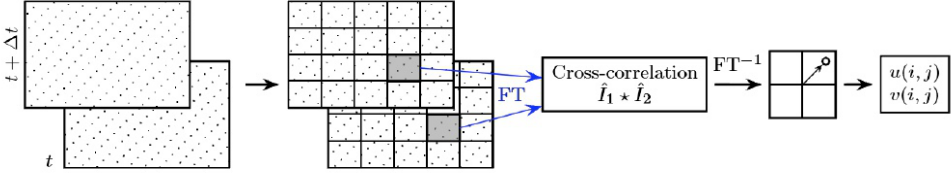


Figure 3.7: Schematic describing the cross-correlation algorithm used in the digital PIV recordings to extract the velocity field (Zhao et al., 2014).

By locating the peak value in the cross-correlation, the average displacement of the particles ( $\Delta x, \Delta y$ ) can be calculated. The location of this peak value was found using a least-square fit of a Gaussian function (Fouras and Soria, 1998). To convert the units of distance from pixels to millimetres, a magnification factor  $M$  of the images is determined using a photograph of a ruler, which was placed in the plane of interest. This plane was illuminated with a laser sheet (Zhao, 2012). Therefore, with the knowledge of  $\Delta t$  and  $M$ , the velocity vector within the interrogation windows can be determined by  $(u, v) = (\Delta x / \Delta t, \Delta y / \Delta t)$ , where  $u$  and  $v$  are the velocity components of the fluid in the  $x$  and  $y$  directions, respectively.

The vorticity is one of the flow quantities of interest, and is defined as

$$\boldsymbol{\omega} = \nabla \times \mathbf{u}, \quad (3.9)$$

where  $\mathbf{u}$  is the velocity vector in the Cartesian coordinate system ( $x$ - $y$ - $z$ ). This study focused on the  $z$ -component of the vorticity vector ( $\omega_z$ ) corresponding to the spanwise component. In component terms,  $\omega_z$  is given by

$$\omega_z = \frac{\partial v}{\partial x} - \frac{\partial u}{\partial y}. \quad (3.10)$$

The data from the PIV experiments have statistical errors. These errors are a result of bias and random errors (Zhao, 2012). They are discussed in more detail in Fouras and Soria (1998), who used a second-order polynomial fit for the local velocity components that improved the accuracy of the numerical differencing when estimating the velocity gradient. Zhao (2012) employed an approach developed by Fouras and Soria (1998) that is used in the present study. The method uses 21 sampled velocity points to calculate the vorticity fields. Again, refer to Zhao (2012) for further details.

The elliptical cylinder models used in the experiments were made from elliptical cross-section aluminium tubing. Five different aspect ratio cylinders:  $AR = 0.1, 0.25, 0.5, 0.67, 1$ , were constructed for the experiments. The aspect ratio ( $AR$ ) is defined as the ratio of the minor to major axis lengths. This is illustrated in Figure 3.8, where the major axis is  $2b$  and the minor axis is  $2a$ . The aspect ratio is therefore  $AR = a/b$ . Details about the actual dimensions of the cylindrical bodies (in mm) are provided in Table 3.2. Note that the effective water channel depth is  $\sim 500$  mm, giving a span to major axis length of  $\sim 20:1$ . The PIV data is taken in a horizontal image plane approximately  $1/3^{rd}$  of the spanwise dimension from the bottom end of the cylinder.

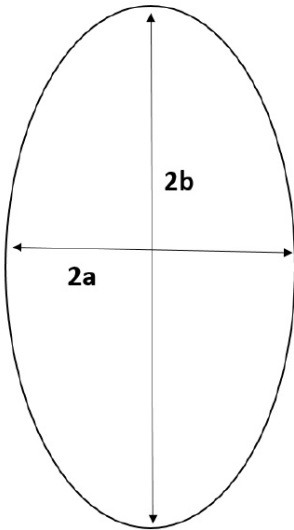


Figure 3.8: The cross section of the elliptical cylinder showing the minor and major axis dimensions.

Table 3.2: Dimensions and properties of the elliptical cylinders used in the present study.

D25					
Dimension a (mm)	Dimension b (mm)	Elliptical ratio, b/a	Elliptical ratio, a/b	Weight (g) (excl. screws)	Notes
25.00	<b>25.00</b>	1.00	1.00	230.2	hollow
20.00	<b>25.00</b>	1.25	0.80	436.5	hollow
16.67	<b>25.00</b>	1.50	0.67	390.3	hollow
14.29	<b>25.00</b>	1.75	0.57	347.5	hollow
12.50	<b>25.00</b>	2.00	0.50	332.1	hollow
10.00	<b>25.00</b>	2.50	0.40	523.6	Solid
8.00	<b>25.00</b>	3.13	0.32	460.9	Solid
6.25	<b>25.00</b>	4.00	0.25	401.4	Solid
5.00	<b>25.00</b>	5.00	0.20	353.4	Solid

Figure 3.9 illustrates a side view of the rig that was used in the current experiments. The cylindrical body was coupled with a force balance sting and was vertically mounted on the locked air-bearing system. Details of the force balance/air-bearing system can be found in Nemes et al. (2012). The platform to conduct these experiments was placed at a height of 165 mm above the water channel floor, and a base plate that had dimensions  $600 \times 400 \times 5$  mm. This provided a small gap of 1 mm between the cylinder and the plate (Zhao et al. 2014) to reduce end effects. The experiments were all runs at a Reynolds number of  $Re = 3900$ , in line with many past literature studies. The Reynolds number was based on the constant (cross-stream) major axis of the elliptical cylinders of  $2b$ .

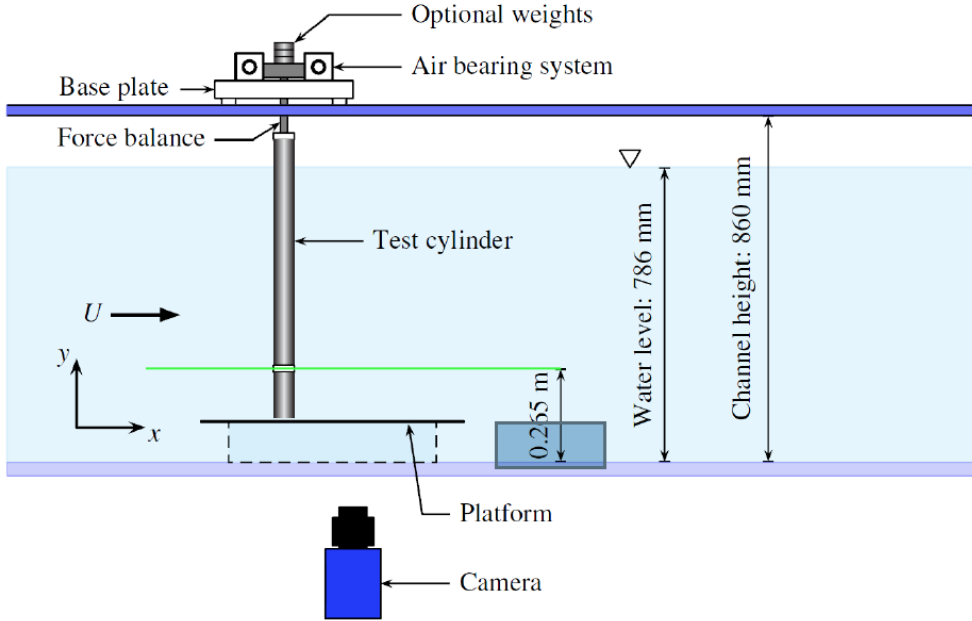


Figure 3.9: Schematic of the water channel used in the current experiments (Zhao et al., 2014). Again, note that the air-bearing is locked at a fixed position.

### 3.9 Chapter summary

In this chapter, a very brief overview of the turbulence models: IDDES and WALE, was provided. These models were used to study the near-wake flow past circular and elliptical cylinders. Some care was used to generate suitable meshes after first developing various prototypes. The final mesh was of a block structure that refined the near-wake region and the cylinder boundary layer. The elliptical meshes were obtained from the circular cylinder mesh by a coordinate transformation, trying to maintain the near orthogonality of the cylinder mesh and the near-wake spatial resolution. Resolution studies were performed showing that even the medium mesh (850,000 cells) produces converged estimates of bulk flow quantities such as the Strouhal number and drag force coefficient. The last part of the chapter described the experimental procedures used to produce a comparison data set of the near wake. In the next chapter, the numerical results of the circular cylinder study will be

presented and discussed. Various model parameters were investigated such as: the effect of turbulence models; the influence of spanwise dimension; and the effect of resolution on the near wake. Predictions of downstream velocity components, Reynolds stresses and surface pressures are compared with results from previous numerical and experimental studies, as well as the new set of experiments. This chapter provides a context for the following chapter where the effects of changing the geometry from circular to elliptical are quantified.

# Chapter 4

## The circular cylinder

As described in the literature review, three-dimensional turbulent flow around a circular cylinder is a much studied flow problem. This chapter reports on the simulation predictions of the flow around a circular cylinder using two different turbulence models: Wall-Adaptive Large Eddy Simulations (WALE) and Improved Delayed Detached Eddy Simulation (IDDES). In addition, a new set of PIV results are presented. In general, the present simulations and experimental results agree with those from previous studies discussed in the literature review. This provides confidence in using these approaches for the elliptical case in the next chapter.

### 4.1 Circular cylinder simulations and experiments

There were several parameters that were varied as part of the investigation. These variations included changing the spanwise length, refining the grid resolution, and comparing the solutions between the WALE and IDDES model. In addition, experiments using PIV are available to complement the numerical data. The predicted results were compared with those of numerical studies by Beaudan and Moin (1994), Kravchenko and Moin (2000), Mittal and Moin (1997), Parnaudeau et al. (2008), and experimental studies by Lourenco and Shih (1994) and Norberg (1987), amongst others.

For the first part of this chapter, the simulations are based on both the WALE and IDDES models using 6.8 million cells covering a span of  $L_Z = \pi D/2$ , and with 50 cells in the spanwise direction. In  $X-Y$  planes, the

cell count was 136 000. These cases will be referred to as case 1 and case 2, respectively. This span size was chosen as a compromise to restrict the number of cells, and noting that the results of Kravchenko & Moin (2000) and others suggest that the predictions do not depend strongly on span length, through their comparison of simulation results using span lengths of  $\pi D$  and  $\pi D/2$ . While Kravchenko & Moin typically used 50 divisions in the spanwise direction of  $\pi D$ , their method was spectral, hence the use of 50 cells in this case for the shorter span of  $\pi D/2$ . Resolution and domain size issues will be considered later in the chapter.

#### 4.1.1 Visualisation of the flow

A sample image of the flow is shown in Figure 4.1. This shows an isosurface of the Q-criterion where Hunt et al. (1988) separated the regions of the flow dominated by shear and rotation. Regions with  $Q > 0$  are rotation dominated. The isosurface value shown in the figure has  $Q = 1$ , noting the maximum value to 1200. The isosurface is coloured according to the static pressure. In can be seen that fine scale turbulent structures are captured in the near wake, as might be expected. Note that Kelvin-Helmholtz vortices appear in the separating shear layers as might be expected at this Reynolds number. (These structures are more visible in other images).

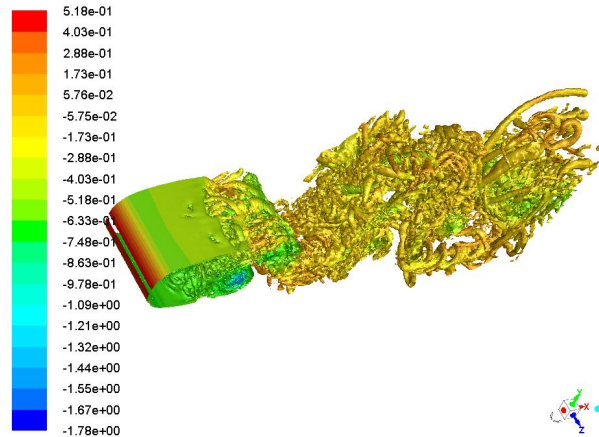


Figure 4.1: Isosurface visualisation the  $Q$ -criterion ( $Q = 1$ ), depicting the vortical wake flow structures for case 1. The isosurface is coloured according to the static pressure.

### 4.1.2 1D turbulent energy spectrum

For the WALE model on the finest grid, the 1D turbulence energy spectrum was obtained by sampling the velocity field on the centreline at  $x/D = 5$  downstream of the cylinder centre point over approximately 10 shedding cycles ( $\Delta t = 50D/U_\infty$ ). The  $\overline{u'u'}$  signal was extracted at each spanwise point in the grid, and the signals were run through a FFT to obtain the 1D energy spectra. More details on extracting these spectra are provided in Kravchenko & Moin (2000) and Ong & Wallace (1996). These spectra were averaged to produce the spectrum shown in Figure 4.2. The experimental results of Ong & Wallace and the LES predictions of Kravchenko and Moin (2000) are overlaid for comparison. It can be seen that the spectra match very well. The inertial subrange is well predicted with the spectra matching up to the short wavelength cutoff of the LES simulations of Kravchenko & Moin (2000) shown by the vertical line. This suggests that the grid resolution is sufficient to capture that range of scales required by LES simulations – extending to within the inertial subrange even  $5D$  downstream.

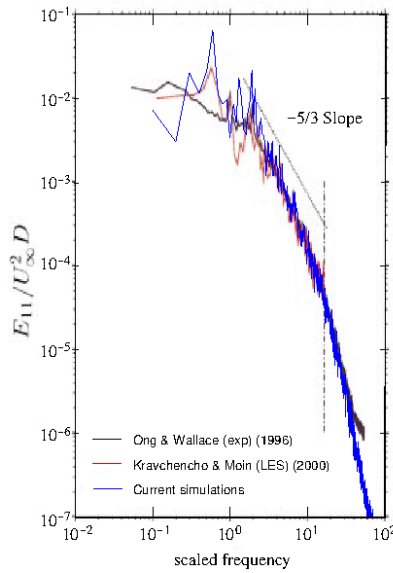


Figure 4.2: One-dimensional turbulent energy spectrum at the point  $(5D, 0)$  downstream from the cylinder centre. The spectra obtained by Kravchenko & Moin (2000) from LES and Ong & Wallace (1996) through experiments are shown for comparison. Case 1 shown.

### 4.1.3 Aerodynamic force components

The lift and drag coefficients were recorded during the simulations. Figure 4.3 shows typical examples of these signals, for the fine grid WALE model with  $L_Z = \pi D/2$ . Something to note is the strong variation in these signals over the simulation time. For example, the drag range varies between approximately between 0.9 and 1.05, but mostly extends over the range [0.94, 0.98]. Similarly, the lift coefficient sometimes shows high amplitude oscillations, and at other times much lower amplitudes. These variations are associated with the mean recirculation zone lengthening and shortening during the flow evolution. The mean lift and drag are recorded in Table 4.1 below.

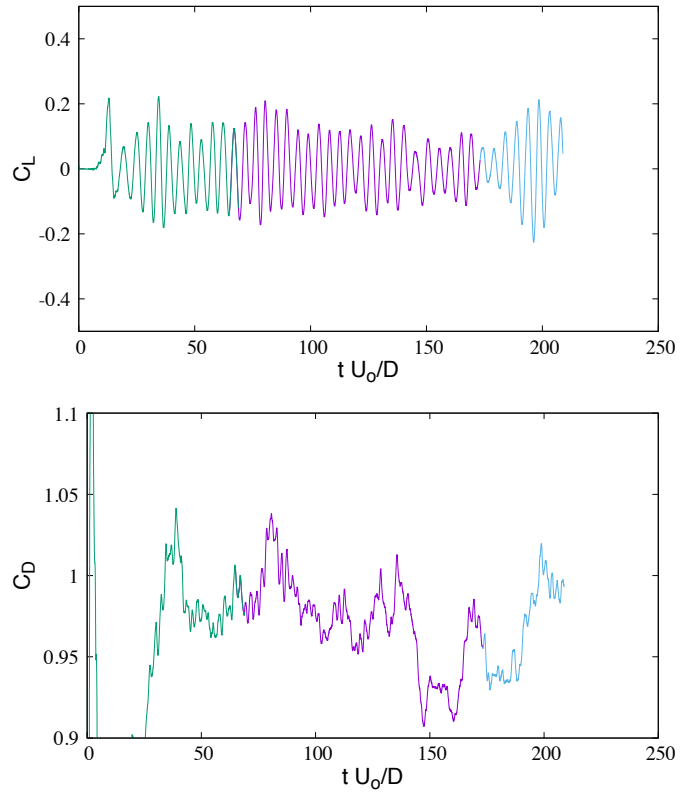


Figure 4.3: Lift (top) and drag (bottom) coefficient variation with time during the simulation using WALE for case 1.

#### 4.1.4 WALE and IDDES predictions

As mentioned in chapter 2, the IDDES model has a number of advantages over other DES-based turbulence models. For the case of the circular cylinder at  $Re = 3900$ , the results from case 1 and 2 simulations were compared to discern differences between the IDDES and WALE models. Figure 4.4 below shows the pressure coefficient distribution around the surface of the cylinder. Generally, the predictions of the WALE and IDDES models show negligible differences. Both predictions were compared with the experimental work of Norberg (1987), which was performed at almost the same Reynolds number of  $Re = 4020$ , and a selection of other literature LES studies and experimental studies. Both turbulence models predict the pressure coefficient variation around the surface to within a few percent of the experimentally measured distribution. This match between cases 1 and 2 is presumably an indication that the IDDES model does an adequate job of predicting the separation point reasonably well. Of course, the IDDES model can revert to the Wall Modelled Large Eddy Simulation model (WMLES) given sufficient resolution. That model is capable of capturing a subset of turbulent boundary layer structures, again dependent on the Reynolds number, although for the current simulations the most important physics to predict the wake correctly is likely to be predicting the correct separation angle and capturing the separating shear layers. The fine grid used here has a maximum  $y^+$  of 0.3 along the cylinder surface, so the boundary layer will be well resolved in both cases.

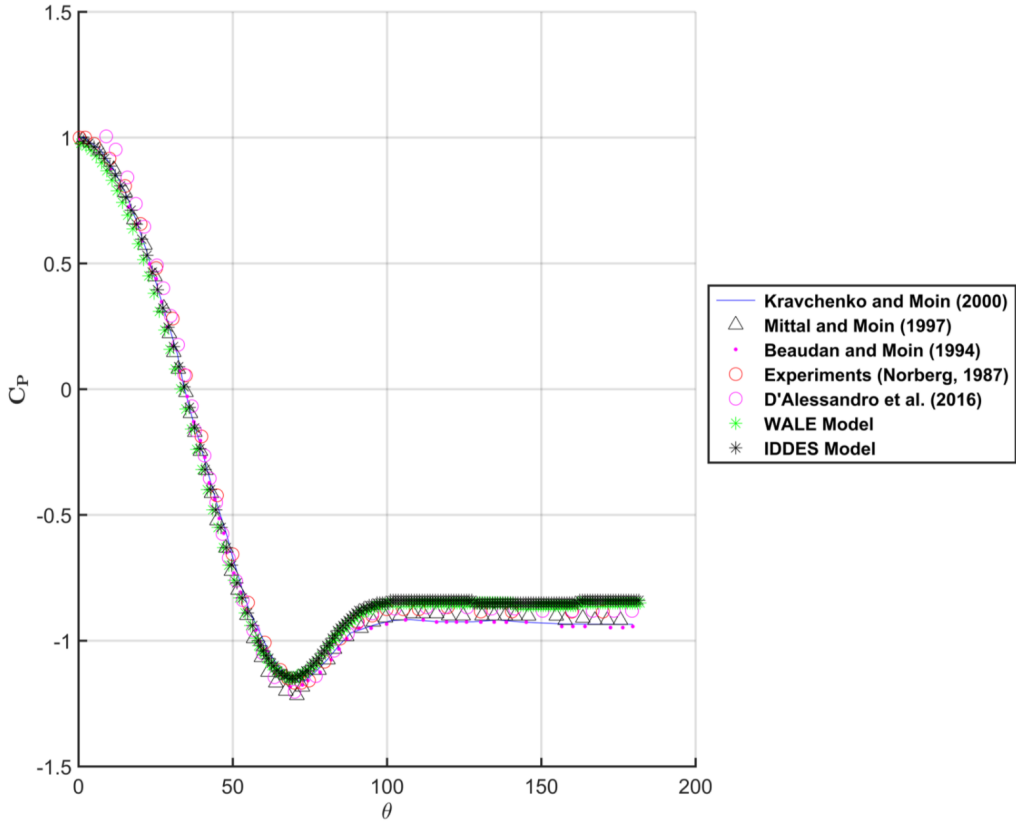


Figure 4.4: Plot of the time-mean pressure coefficient around the surface of the body ( $\theta$ ) for current predictions using the WALE and IDDES models and previous predictions of numerical and experimental results.

Figure 4.5 shows the variation of the spanwise averaged time-mean streamwise velocity along the centreline. The differences between the IDDES model and the WALE model were small. In comparison to previous studies, the mean recirculation length was slightly longer and the recovery downstream a little slower. However, there is a large range in this variation between different literature studies. The recirculation length will depend on upstream turbulence level, amongst other factors, which is not treated adequately with the current model. In addition, as shown in Figure 4.3, the drag fluctuates considerably over the integration time. When the drag coefficient oscillates at a low value, the recirculation zone tends to be longer; in fact, observations of the wake over time shows that it can spend long times in this extended state

before returning to a more compact state. Thus, the integration time may need to be longer to obtain a reliable average for the downstream velocity variation.

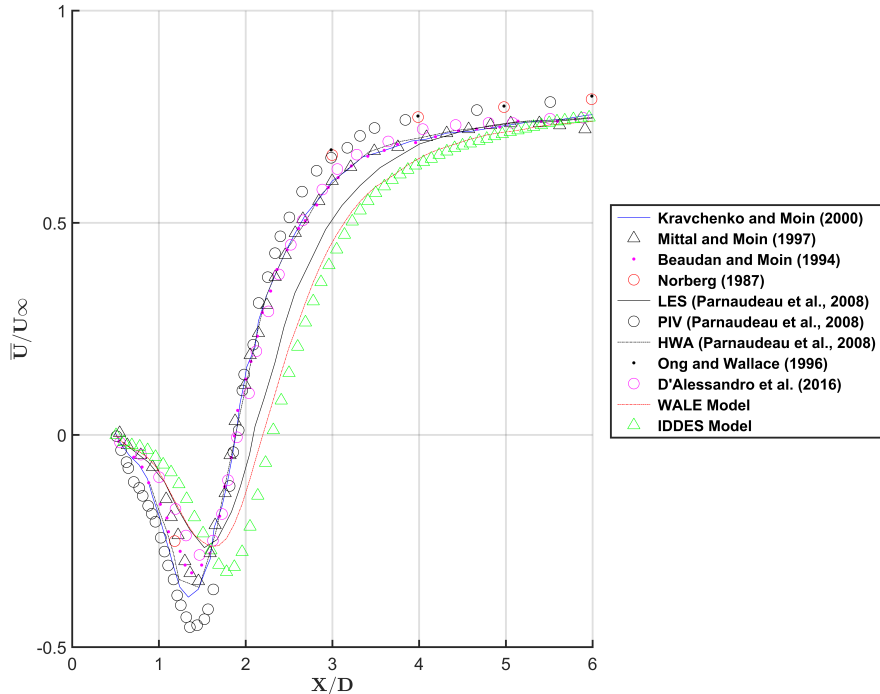


Figure 4.5: Plot of the time-mean streamwise velocity in the wake behind the body from the present predictions and previous studies.

Table 3.1, summarises important parameters from the present simulations compared with previous numerical and experimental studies. Interestingly, using the IDDES model predicted a slightly longer recirculation bubble length in comparison to the WALE model, however, note the comments in the previous paragraph. In both cases, the recirculation bubble predicted was significantly larger compared to other studies. The drag coefficient and Strouhal number were also extracted for each model. Generally, the drag coefficient,  $C_D$ , and Strouhal number,  $St$ , compare well with previous simulations and experiments. It is worth noting that  $C_D$  of Kravchenko and Moin (2000) was slightly higher compared with other studies.

Table 4.1: Flow variables and parameter from the present simulations compared to other computational and experimental studies.

Data source	$C_D$	$L/D$	$St$
Norberg (1987)	$0.98 \pm 0.05$	$1.4 \pm 0.05$	$0.21 \pm 0.10$
Mittal and Moin (1997)	1.00	1.40	0.21
Beaudan and Moin (1994)	1.00	1.36	0.20
Kravchenko and Moin (2000)	1.04	1.35	0.21
Sidebottom and Jones (2012)	0.89	1.19	0.18
Khan et al. (2016)	1.61	2.26	0.21
D'Alessandro et al. (2016)	1.02	1.43	0.22
Present (IDDES)	0.95	1.75	0.21
Present (WALE)	0.97	1.65	0.22

The time-mean streamwise velocities were plotted on vertical lines at different distances in the wake behind the cylinder. Figure 4.6 shows the mean velocity profile with increasing downstream distance in the wake. The solutions produced by the WALE and the IDDES model show very similar trends. Given the differences between the wake recovery of these time-mean results and other literature results, the match is good, with the wake shape variation with downstream distance matching well with other results. In particular, the change in the wake from a  $U$  shape to a  $V$  shape is predicted well. Ma et al. (2000) explained that this change in the shape of the profile (for  $Re=3900$ ) is due to the increase in the fluctuations in the wake.

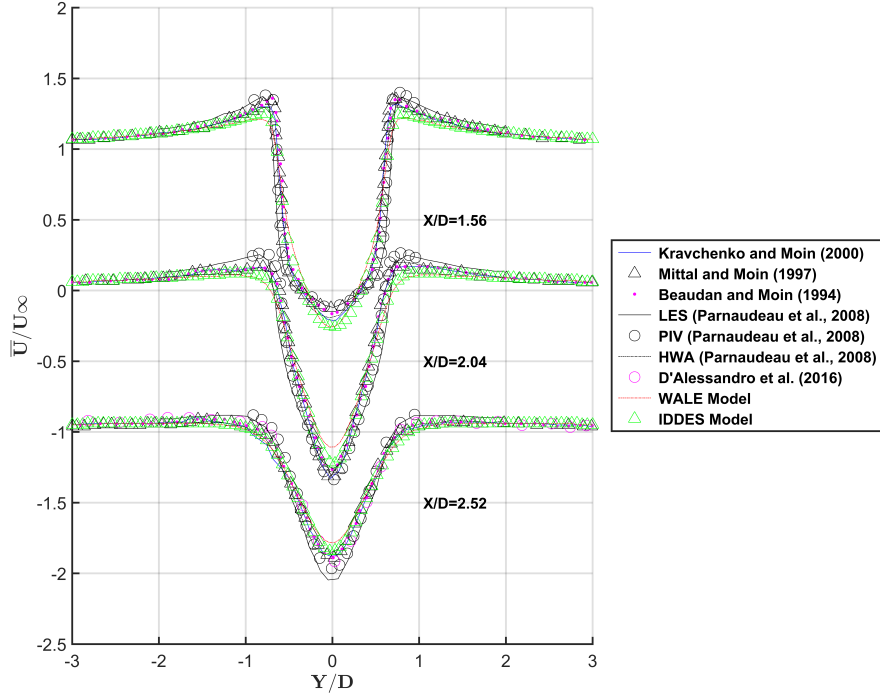


Figure 4.6: Plots of the time-mean near-wake streamwise velocity at  $X/D = 1.56, 2.04 \& 2.52$  for different turbulence models, including literature results.

Similar observations can be made using the profiles of the cross-flow velocity at the same points in the wake. Figure 4.7 shows antisymmetry in the cross-flow velocity at the same downstream positions are the previous figure. Interestingly the IDDES model appears a better fit to the numerical and experimental literature profiles than WALE in the first near wake point. It can be noted that for both present numerical turbulence models, the cross-flow velocity profile contains sharper peaks compared to other studies. At  $X/D=2.04$ , the shape of the cross-flow velocity profile expands further in the vertical direction with sharper peaks. The predictions from the IDDES model shows a very good match when compared to the first three studies in Figure 4.7 (i.e. Kravchenko and Moin (2000), Mittal and Moin (1997) and Beaudan and Moin (1994)). Interestingly, the results from the WALE model agrees best with the LES results as well as with the experimental results from Parnaudeau et al. (2008). At  $X/D=2.52$ , it can be seen that both the

WALE and IDDES models show good agreement with profiles from previous studies. It is worth noting that the PIV and LES results from Parnaudeau et al. (2008) contain sharper peaks compared to other past studies.

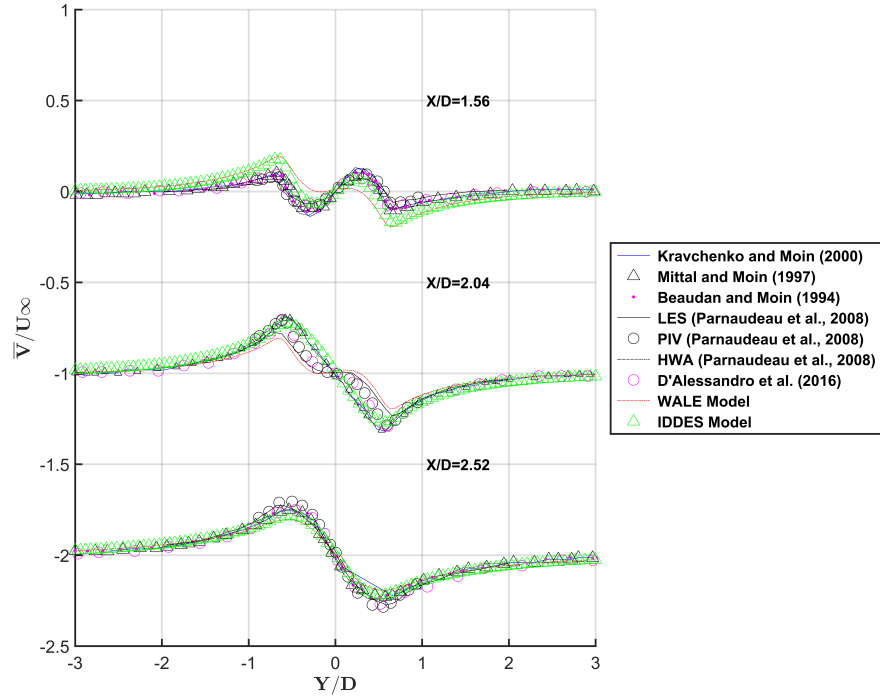


Figure 4.7: Plots of the spanwise-averaged time-mean cross-flow velocity at  $X/D = 1.56, 2.04$  and  $2.52$  in the near wake. Literature results as marked.

Figure 4.8 shows the correlation of the streamwise velocity fluctuations  $\overline{U'U'}/U_\infty^2$  as a function of downstream distance. The same downstream locations used previously are used for comparison. Generally, the solution provided by both models agree well; but with some differences. Close to the rear of the cylinder, the profiles are less peaked and in some other studies, while still maintaining the correct general shape and level. Further downstream the comparison between previous simulations and experiments is closer, with a reasonable match with both PIV results and other simulations. Parnaudeau et al. (2008) found that the formation of these strong peaks were due to the transitional state of the shear layers.

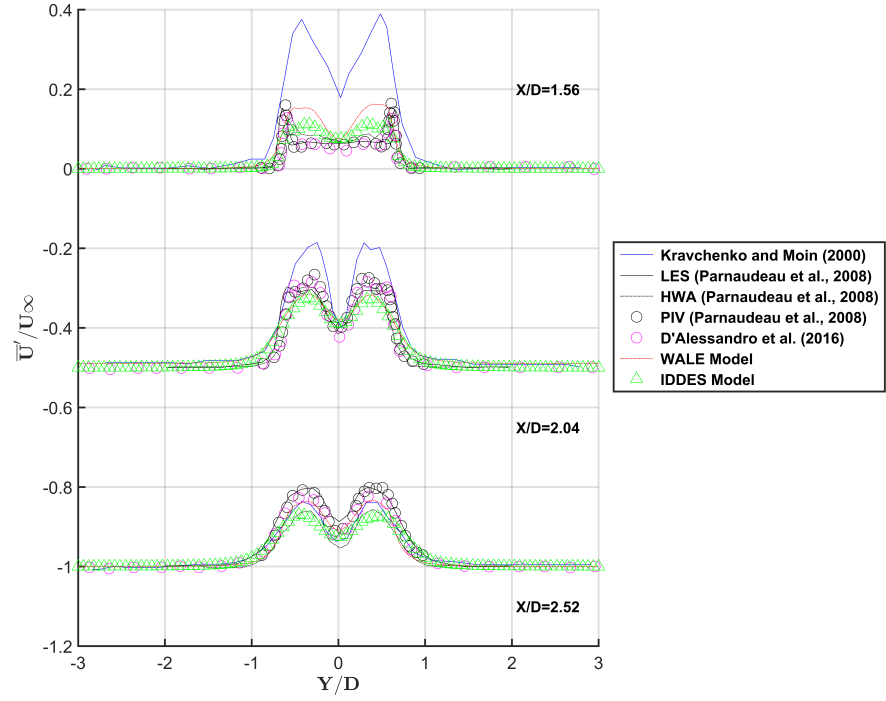


Figure 4.8: Plots of the  $\overline{U'U'}/U_\infty^2$  Reynolds stress component at  $X/D = 1.56$ ,  $2.04$  and  $2.52$  in the near wake.

Figure 4.9 shows the correlation of the streamwise velocity fluctuations  $\overline{V'V'}/U_\infty^2$  as a function of downstream distance. The value is high close to the centreline in the wake. This strong peak arises due to shear layer flapping associated with vortex shedding. It can also be observed that there are no major differences between the results of the WALE model and IDDES model. In fact, for both models, there is an over-prediction in the variance of the  $V'$  fluctuating velocity component compared to the numerical and experimental solutions of Parnaudeau et al. (2008). This difference decreases substantial on moving further downstream. Again, the differences are likely due to the over-prediction of the recirculation zone length, relative to other studies.

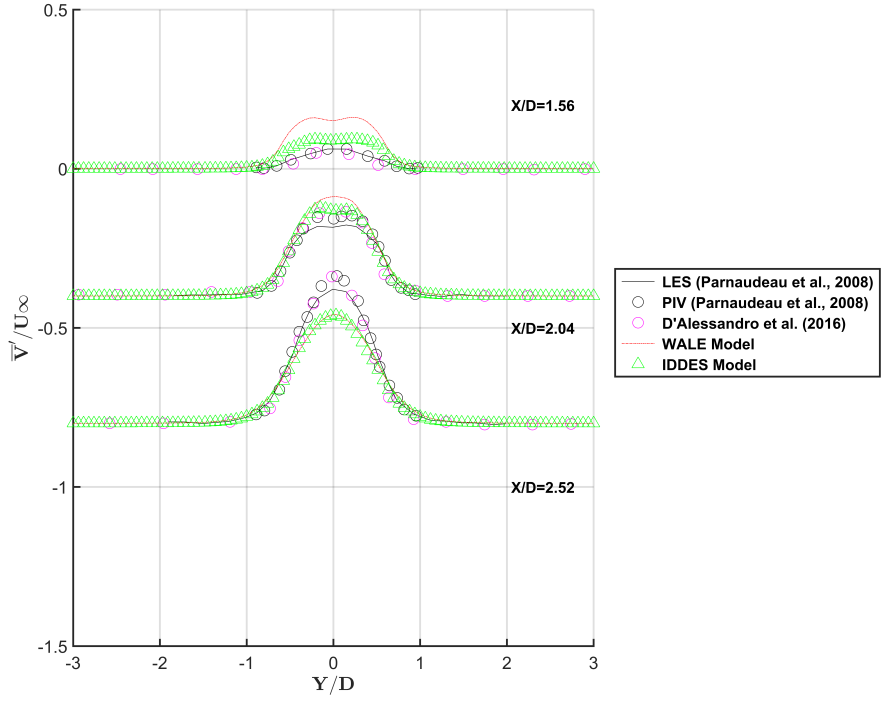


Figure 4.9: Plots of the  $\overline{V'V'}/U_\infty^2$  Reynolds stress component at  $X/D = 1.56$ ,  $2.04$  and  $2.52$  in the near wake.

Figure 4.10 shows the  $\overline{U'V'}/U_\infty^2$  Reynolds stress component profiles in the near wake. There are extrema on either side of the wake centreline corresponding to the locations of the shear layers. The near wake profile at  $X/D = 1.56$  has the correct general shape for both the WALE and IDDES models in comparison to the PIV and LES results of Parnaudeau et al. (2008), however, the peaks are slightly over-predicted. Further downstream the shape changes so that the reverse slope region between the peaks is not picked up with the current models. Still further downstream at  $X/D = 2.52$ , the results again match better the general shape of those of Parnaudeau et al. (2008). Overall, the differences are likely mostly associated with the longer recirculation bubble length, which is likely to shift the downstream position at which the profiles change their general shape.

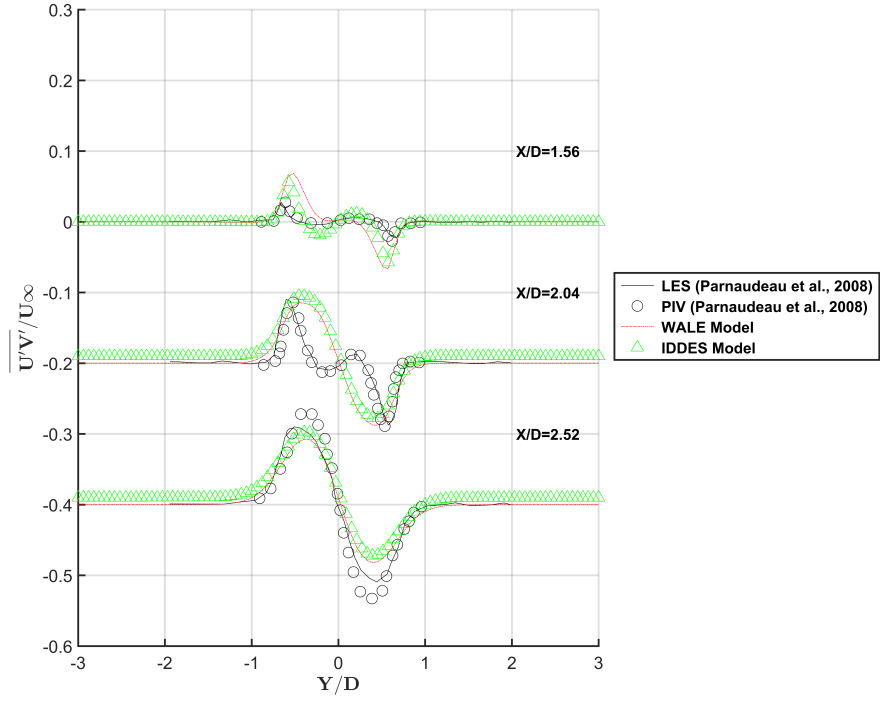


Figure 4.10: Plots of the  $\overline{U'V'}/U_\infty^2$  Reynolds stress across wake at  $X/D = 1.56, 2.04$  and  $2.52$ .

The comparisons above show that, although there are some differences, the WALE and IDDES models provide reasonable predictions of the turbulent flow field around a circular cylinder at  $Re = 3900$ . It is likely that most of the differences in profiles are due to the slight over-prediction of recirculation bubble length, which means that taking fixed downstream distances to compare profiles accentuates differences.

The next section examines sensitivity to grid resolution prior to embarking on the elliptical cylinder study in the next chapter. In that study the WALE model will be used solely, as it is more a pure form of LES and shows the correct physical behaviour as no-slip boundaries are approached. However, the study on the flow past a circular cylinder so far has indicated that the wake predictions are not strongly dependent on the turbulence model used, noting that both models revert to LES outside the boundary layer anyway. The IDDES is mainly used for higher Reynolds numbers in engineering

applications due to its capability to model the entire boundary layer with RANS, making it considerably cheaper for higher Re flows.

#### 4.1.5 Grid sensitivity

This section reports on the sensitivity of predictions to grid resolution to provide more confidence in the robustness of the setup to adequately predict the flow over elliptical cylinders. In the first part of the study, two meshes were used. The first mesh consisted of 850,000 cells, with  $N_Z = 25$  cells in the spanwise direction. The second mesh, which is the one used for the study above, had double spatial resolution, i.e., 8 times as many cells, or 6.8 million in total. These predicted wakes based on these two meshes showed only minor changes to the fields and profiles considered above. Figures 4.11–4.14 show comparisons of different variables between the two cases.

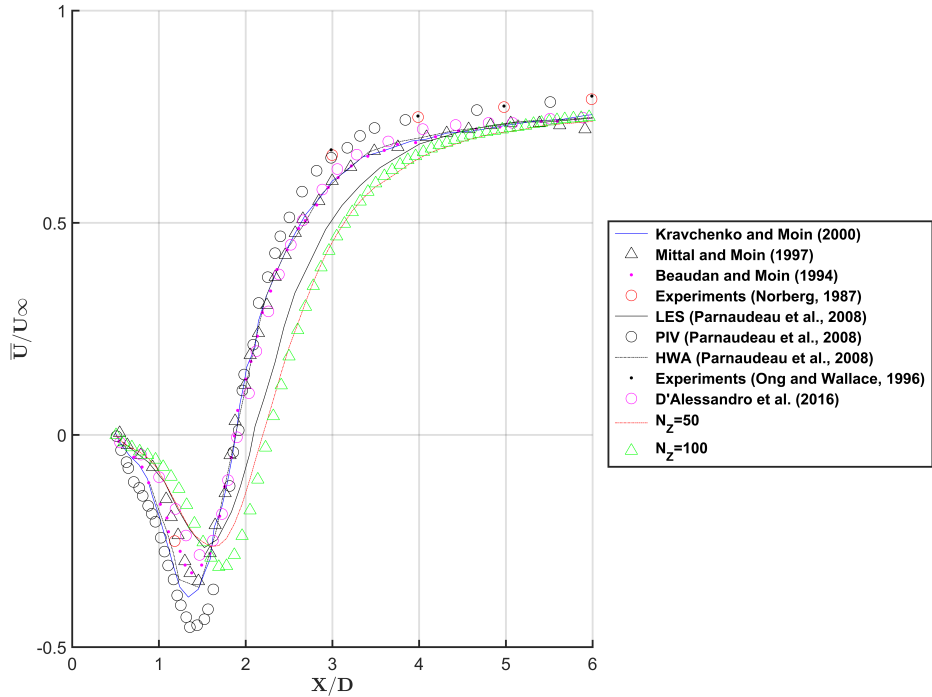


Figure 4.11: The time-mean streamwise velocity variation along the centreline for the medium and fine grids using the WALE model.

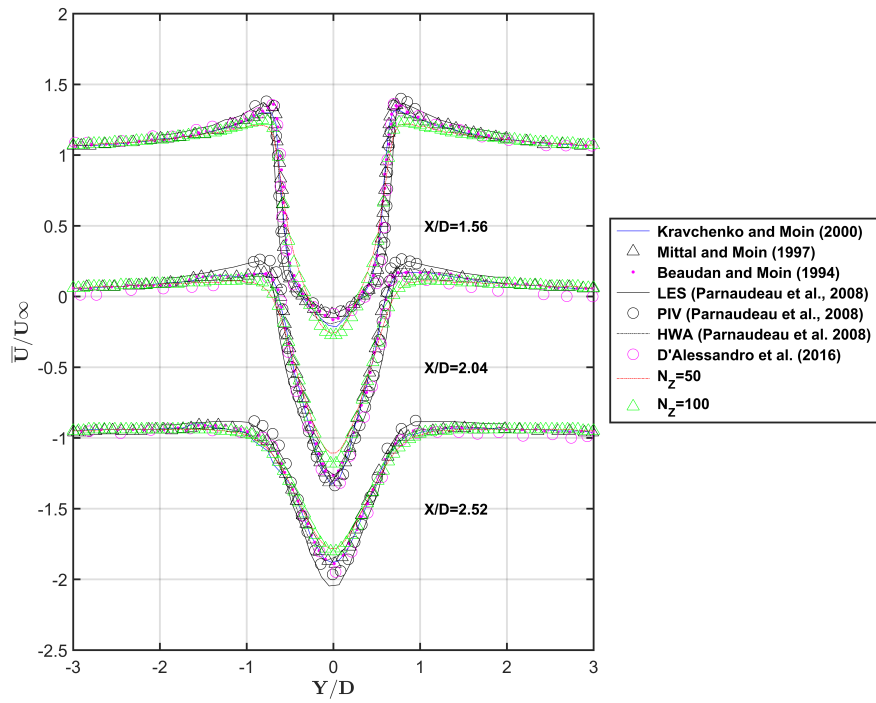


Figure 4.12: The time-mean streamwise velocity on vertical lines at  $X/D = 1.56, 2.04 \& 2.52$  for the medium and fine grids using the WALE model.

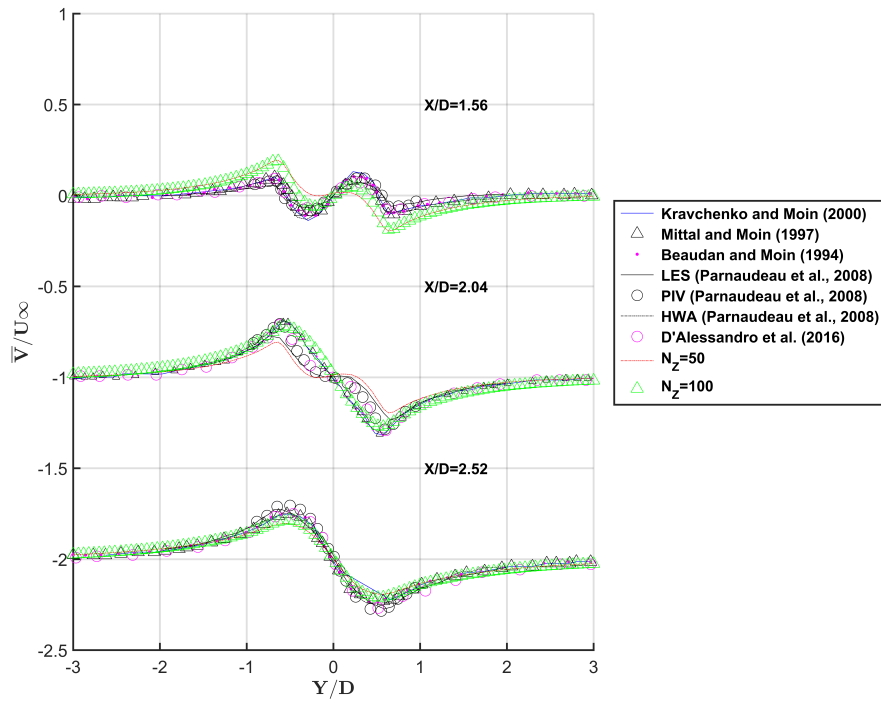


Figure 4.13: The time-mean cross-stream velocity on vertical lines at  $X/D = 1.56, 2.04 \& 2.52$  for the medium and fine grids using the WALE model.

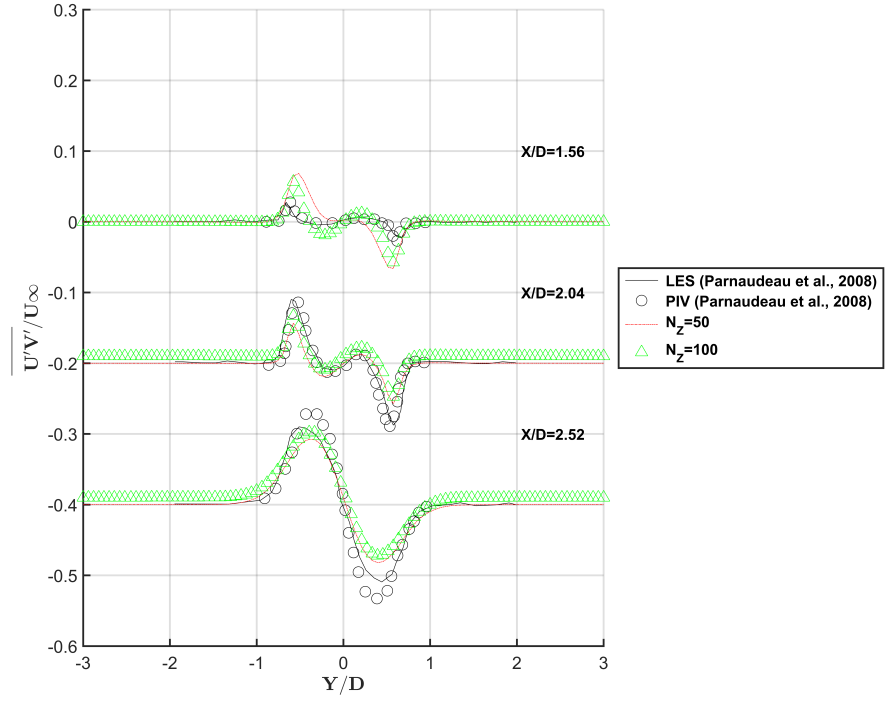


Figure 4.14: The time-mean  $\overline{U'V'}/U_\infty^2$  Reynolds stress component on vertical lines at  $X/D = 1.56, 2.04 \& 2.52$  for the medium and fine grids using the WALE model.

Interestingly, there are only relatively small differences in the predictions of these parameters between the medium and fine mesh. The differences are probably mostly generated from the slight difference in recirculation bubble extent, which in turn, is likely at least partially a result of averaging time. Thus, even though the medium mesh has less than 1 million cells, it still produces reasonable predictions.

#### 4.1.6 Sensitivity to spanwise domain length

Another computational parameter that is studied is the spanwise domain length. This is changed from  $\pi D/2$  to  $\pi D$ , also increasing the cells in span by factor of two and thus retaining the spanwise resolution. The different flow parameters were plotted and compared to the reference case. Since

the features of the flow will be the same as above, only some of the results are shown in this section. Figure 4.15 shows the mean pressure coefficient predictions using the different spanwise lengths of  $\pi D/2$  and  $\pi D$ . It was found that although the spanwise length is doubled, the solution does not change significantly between  $\theta = 0^\circ$  and  $60^\circ$ . Interestingly, there is a small difference in the pressure coefficient around the surface between  $\theta = 60^\circ$  and  $180^\circ$ .

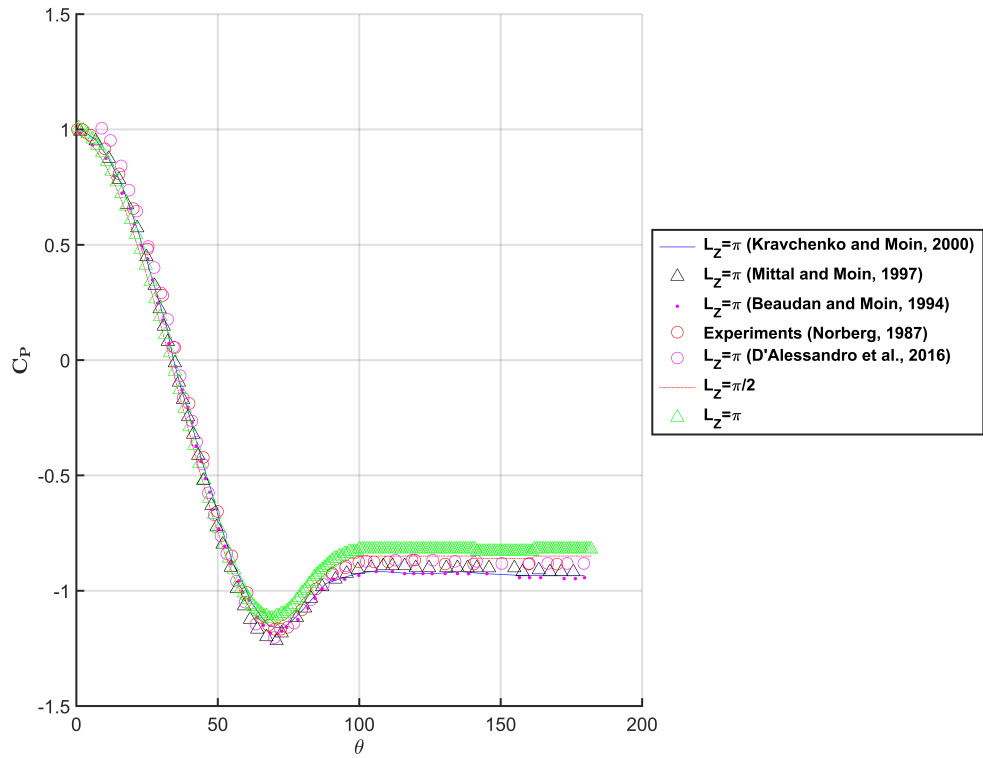


Figure 4.15: Plot of the time-mean pressure distribution in the wake behind the body using two spanwise lengths  $L_Z = \pi D, \pi D/2$ .

Figure 4.16 represents the time-mean streamwise velocity along the centreline in the wake downstream of the cylinder for both span sizes. By changing the spanwise length from  $\pi D$  to  $\pi D/2$ , the velocity profile does not vary significantly. Note that there is a difference in the recirculation region compared to previous numerical and experimental studies; this difference was

addressed earlier. In addition, there is a crossover of the current results and others in the region  $X/D = 5\text{--}7$ .

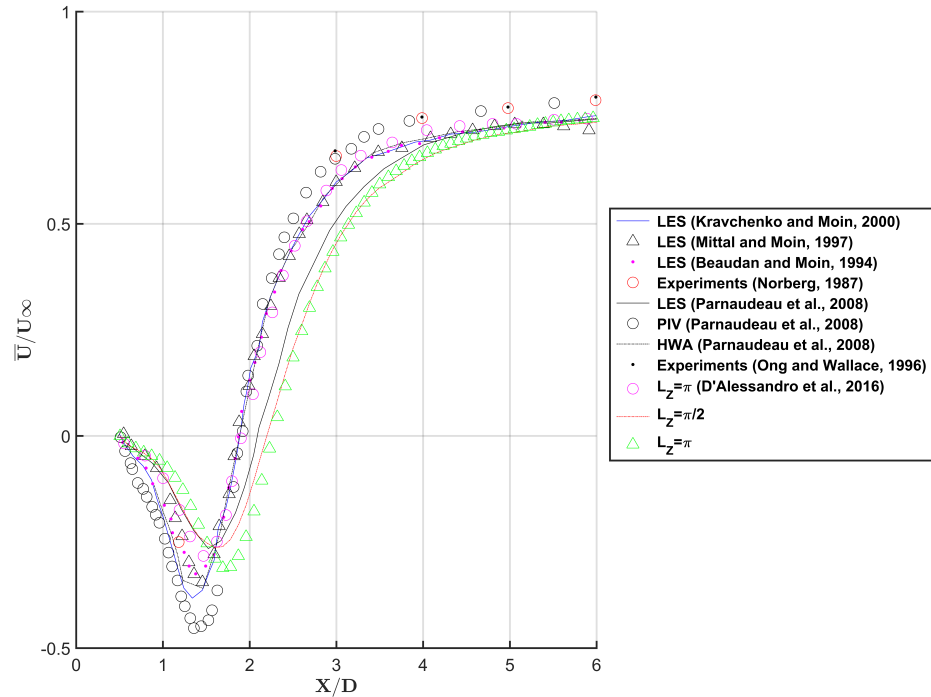


Figure 4.16: Plot of the time-mean streamwise velocity in the wake behind the body using two spanwise lengths  $L_Z = \pi D, \pi D/2$ .

In Figure 4.17, the velocity profiles at different sections in the wake are compared with current and previous measurements taken at  $X/D=1.56, 2.04$  and  $2.52$ . In terms of the variation of the spanwise length, it was observed that as the span was doubled from  $\pi D/2$  to  $\pi D$ , the accuracy of the solution does not change significantly when compared with previous studies. In general, the effect of doubling the span in the  $Z$ -direction does not have a significant effect on the solution. The shorter span is used for the remaining simulations because it has a smaller cell size in the span direction, so it should be better able to resolve the spanwise flow variation.

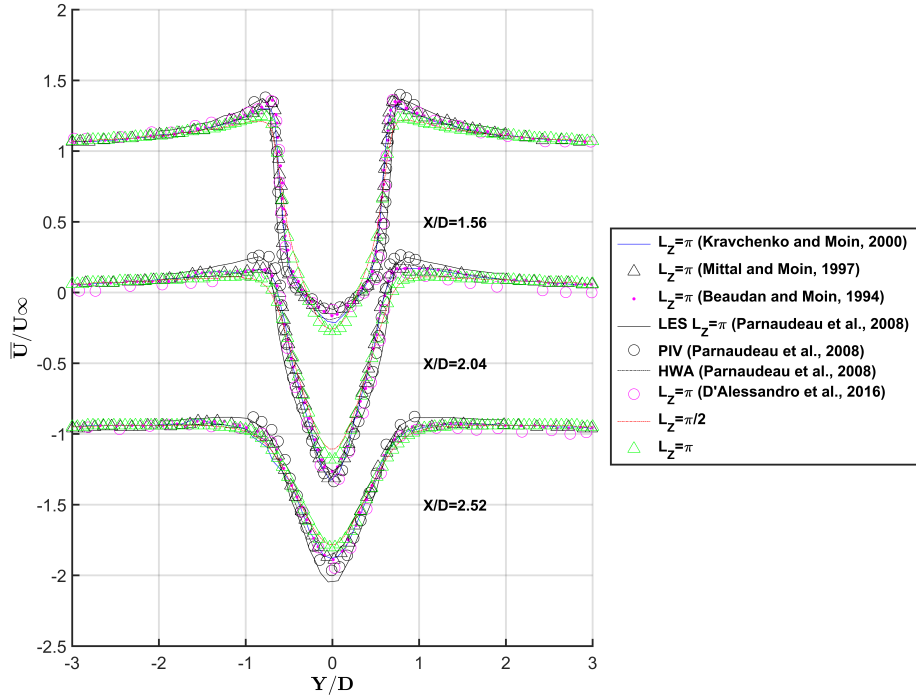


Figure 4.17: Plots of the time-mean streamwise velocity at  $X/D = 1.56, 2.04$  &  $2.52$  using two spanwise lengths  $L_Z = \pi D, \pi D/2$ .

#### 4.1.7 Comparison with experiments

The experiments were performed in the Fluids Laboratory for Aeronautical Industrial Research (FLAIR) at Monash University. The primary aim was to produce an experimental data set for elliptical cylinder wakes. In this chapter, the aim is to show that the PIV results are consistent with other experimental results for a circular cylinder.

The results were compared with previous experimental studies conducted by Ong and Wallace (1996), Norberg (1987) and Lourenco and Shih (1994). Figure 4.18 shows the time-mean streamwise velocity comparing both numerical and PIV results. Generally, the agreement is good between the current numerical and experimental results. It was observed that the recirculation bubble length from the present PIV measurements is similar to that mea-

sured by Norberg (1987). On the other hand, the numerical results show a slightly longer recirculation bubble length, as discussed previously.

Table 4.2: Flow parameters from the present work compared to other computational and experimental studies.

Data from	L/D
Norberg (1987)	1.4±0.05
Mittal and Moin (1997)	1.40
Beaudan and Moin (1994)	1.36
Kravchenko and Moin (2000)	1.35
Sidebottom and Jones (2012)	1.19
Khan et al. (2016)	2.26
D'Alessandro et al. (2016)	1.43
PIV (Present)	1.5±0.05
Present (WALE)	1.65

Table 4.2 shows data comparing the recirculation bubble length from previous studies and the current numerical studies. It can be seen that the differences between the experimental and numerical results are not very significant. In fact, the recirculation bubble length between the current PIV experiments and Norberg's (1987) experiments are very close in agreement. It should be noted, however, that recirculation bubble lengths are affected by a number of influences, such as background turbulence and period used for time-averaging.

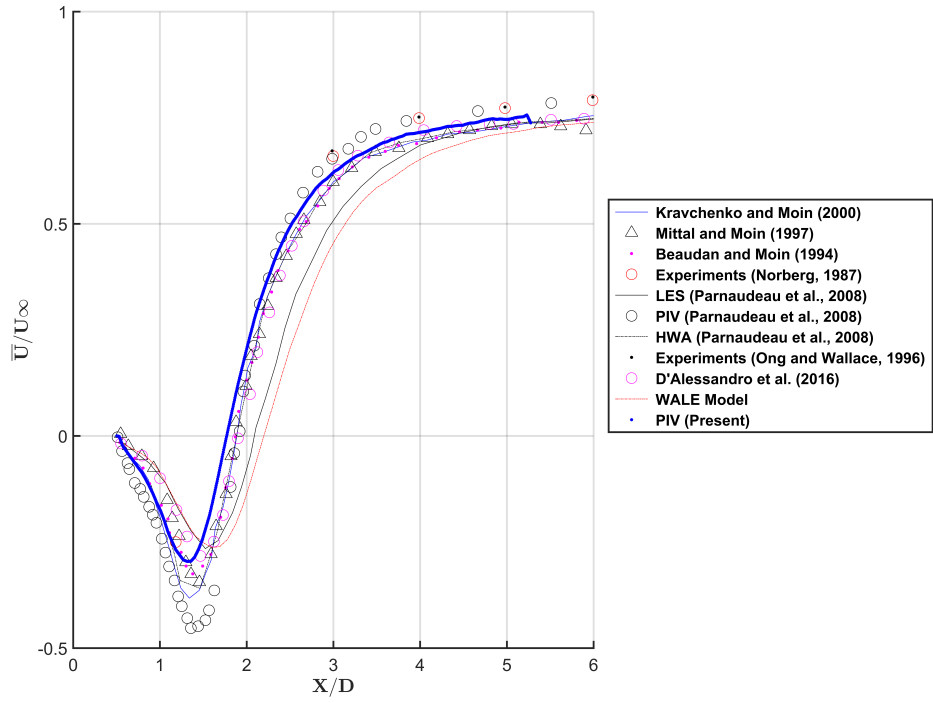


Figure 4.18: Plots of the time-mean streamwise velocity in the wake downstream of the circular cylinder comparing the LES predictions with PIV experimental results.

Figure 4.19 present plots of the streamwise velocity at  $X/D = 1.56\text{--}2.52$ . The PIV measurements show good agreement with the numerical predictions alongside other studies with minor differences around the recirculation region. The other parameters such as the cross-flow velocity (Figure 4.20), the Reynolds stresses (Figure 4.21) were investigated, which also show reasonable agreement.

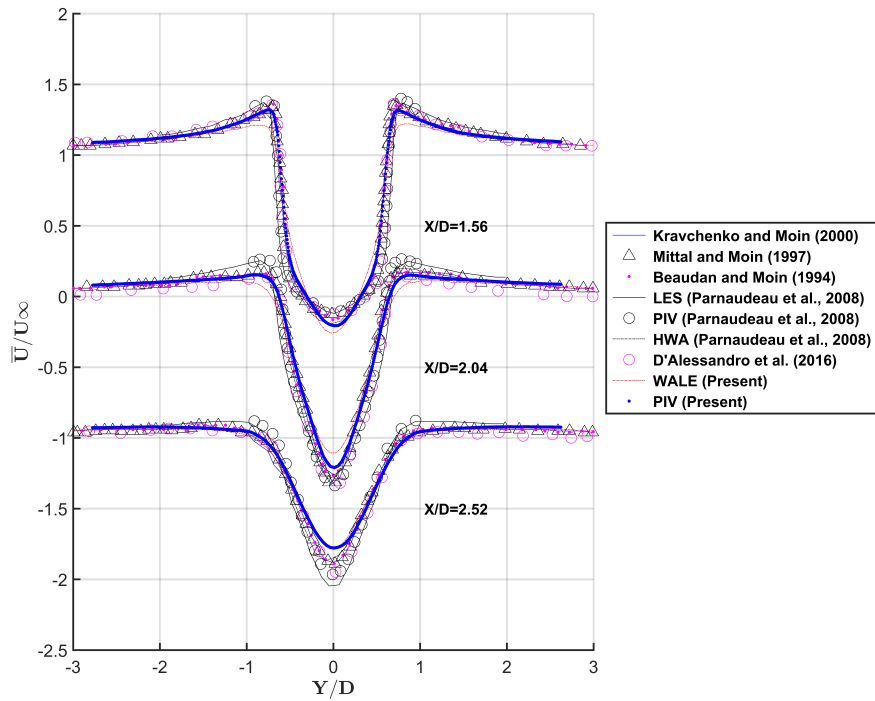


Figure 4.19: Plot of the time-mean velocity at  $X/D = 1.56, 2.04 \& 2.52$ , comparing the WALE predictions with the PIV results.

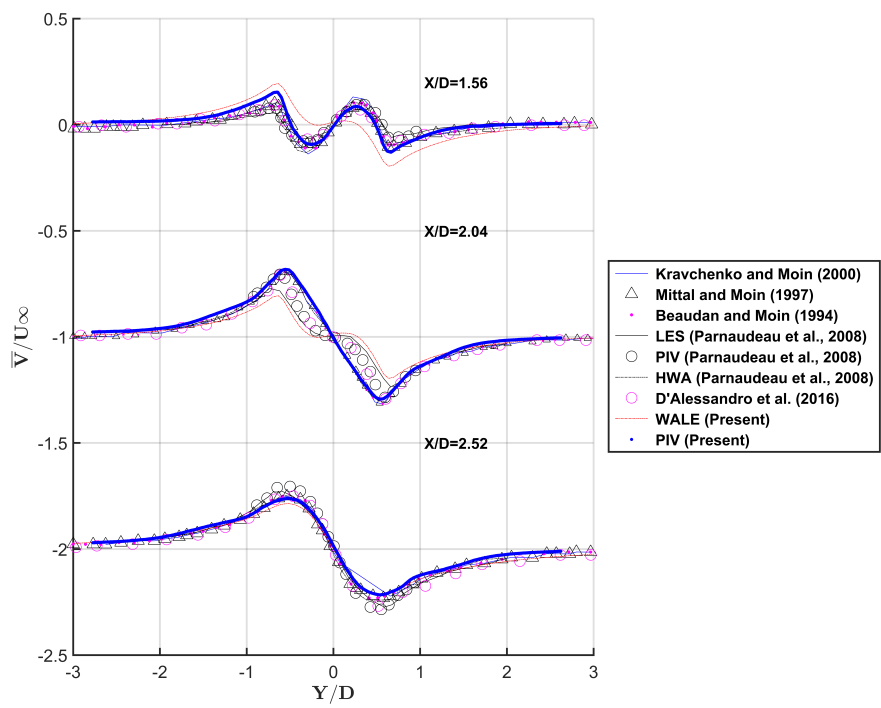


Figure 4.20: Plot of the cross-stream velocity component at  $X/D = 1.56$ ,  $2.04$  &  $2.52$ , comparing the WALE predictions with the PIV results.

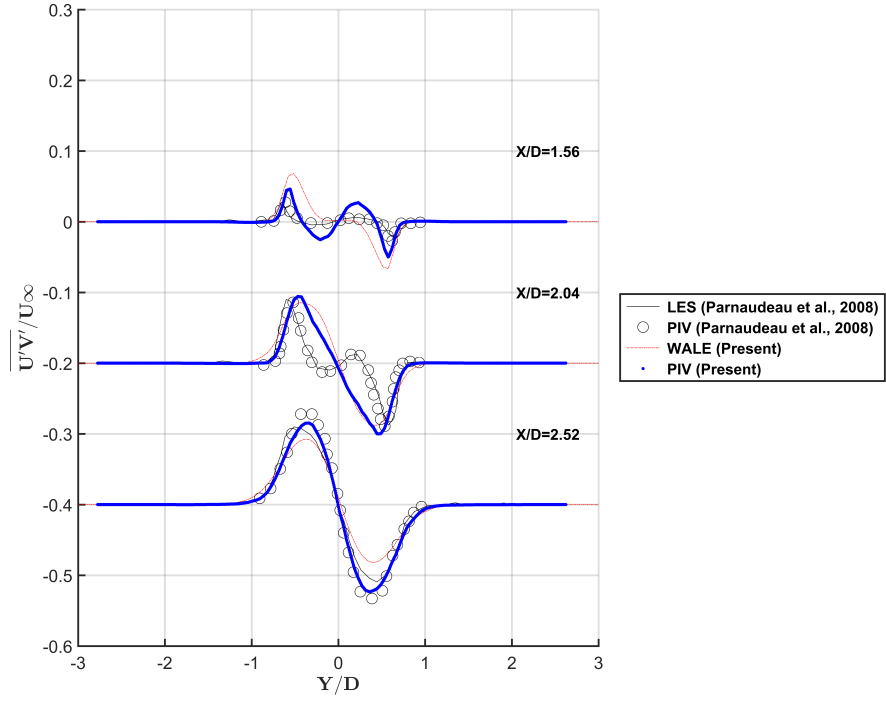


Figure 4.21: Plot of the  $\overline{U'V'}/U_\infty^2$  Reynolds stress component at  $X/D = 1.56$ ,  $2.04$  &  $2.52$ , comparing the WALE predictions with the PIV results.

Overall, the numerical results show good agreement with the present PIV measurements. Perhaps surprisingly, the current experiments appear to fit the numerical predictions slightly better than previous experimental datasets. These experiments will be replicated for the elliptical case to compare with the present numerical predictions.

#### 4.1.7.1 Full field comparisons

One of the problems with the profile comparisons is that if the recirculation bubble length is slightly off, the profiles can appear quite different, while the overall fields can be quite similar (apart from the offset, of course). Thus, this section compares predicted velocity and Reynolds stress components against experimental fields using contour plots, in the same way that Dong et al. (2006) used them to compare numerical predictions with PIV results.

Figure 4.22 shows the mean  $U$  velocity component field in the near wake compared to the experimental field. Clearly, the predictions are a good match to the experimental results. Notice the slightly thicker shear layers of the PIV field, due to cross-correlations over  $32 \times 32$  interrogation windows, and recall that the PIV window extended to  $5D$  downstream. Figure 4.23 shows the comparison of the  $V$  velocity component. Here, the general shape of the predicted field closely replicates the experimental field although there are slight differences in the recirculation zone. Figure 4.24 shows a comparison of the predicted and measured  $\overline{U'V'}/U_\infty^2$  Reynolds stress component. Again the comparison is strong with the general shape and magnitude of the Reynolds stress component field predicted well. Dong et al. (2006) supply similar predicted and experimental contour plots in their paper where they use DNS to calculate the flow. A similar match is observed between the predictions here and their predictions.

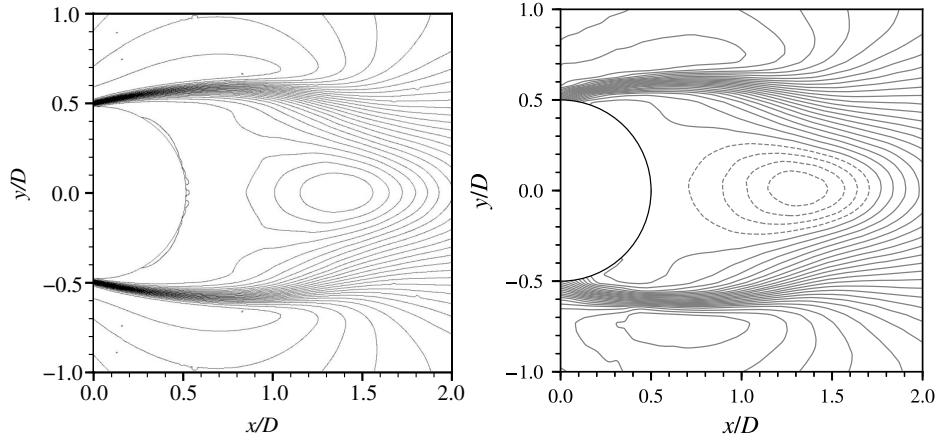


Figure 4.22:  $U$  velocity component field contour plots. Left: simulated result for case 1; Right: experimental result from PIV. The contour levels were chosen to match those used by Dong et al. (2006). Minimum value: -0.252, increment: 0.063.

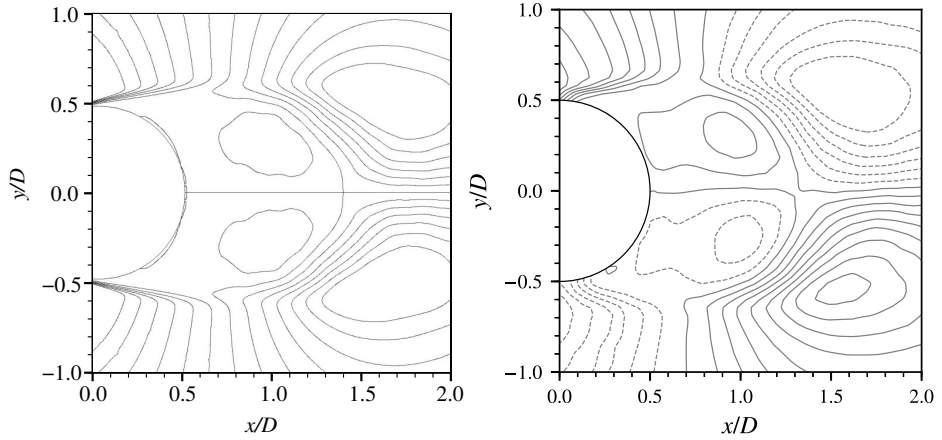


Figure 4.23:  $V$  velocity component field contour plots. Left: simulated result for case 1; Right: experimental result from PIV. The contour levels were — Minimum value: -0.228, increment: 0.038.

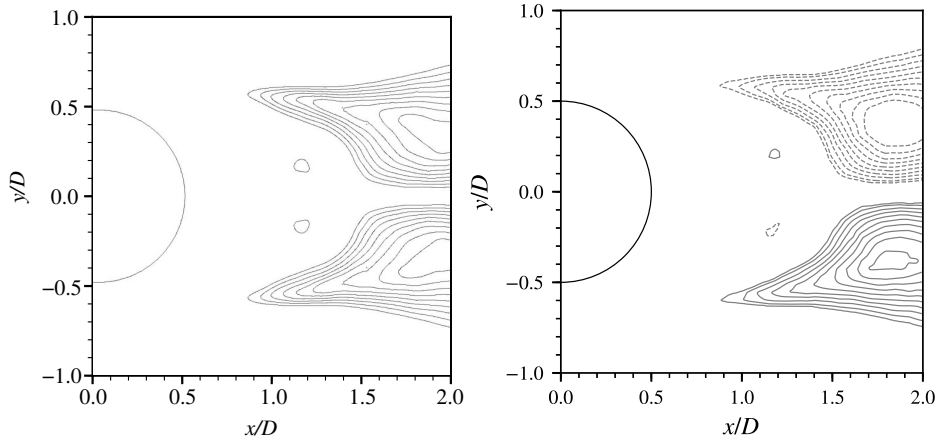


Figure 4.24:  $\overline{U'V'}/U_\infty^2$  Reynolds stress field contour plots. Left: simulated result for case 1; Right: experimental result from PIV. The contour levels were chosen to match those used by Dong et al. (2006). Minimum value:  $\pm 0.03$ , increments:  $\pm 0.01$ .

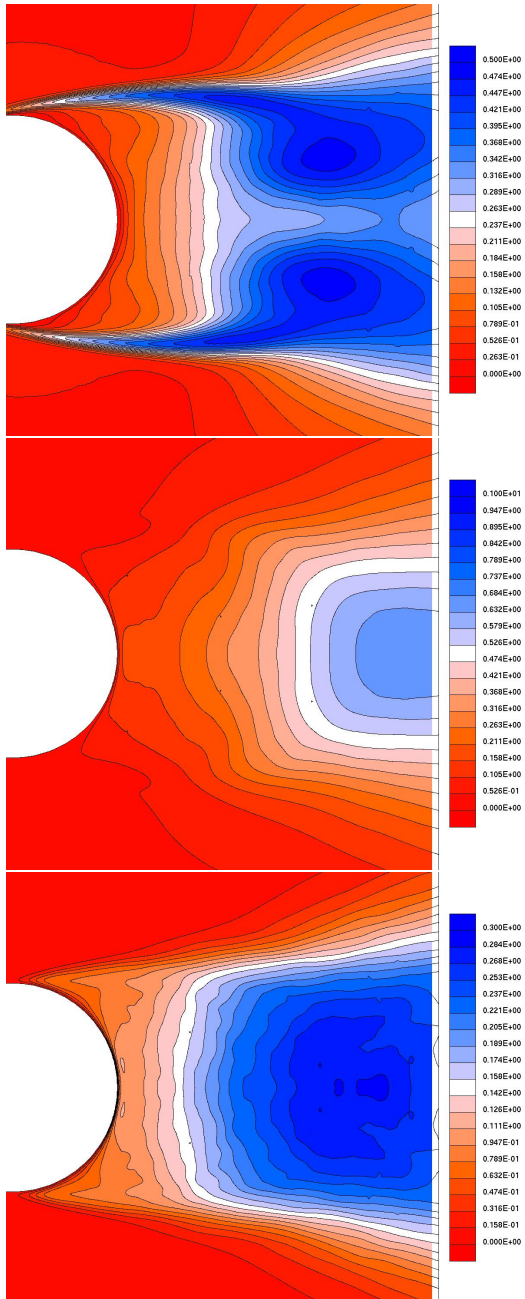


Figure 4.25: Predicted  $\sqrt{(\bar{U}'\bar{U}' / U_\infty^2)}$  (top),  $\sqrt{(\bar{V}'\bar{V}' / U_\infty^2)}$  (middle),  $\sqrt{(\bar{W}'\bar{W}' / U_\infty^2)}$  (bottom) RMS velocity correlation contours for case 1. Region shown covers  $x \in [0, 2]$ ,  $y \in [-1, 1]$ .

Finally, Figure 4.25 shows the predicted rms velocity correlations for case 1 for  $U'$ ,  $V'$ ,  $W'$ . Once again, Dong et al. (2006) supplies the  $U'$  rms field, which is very similar to the predicted field shown in this figure.

## 4.2 Chapter summary

In this chapter, the flow around a circular cylinder was investigated using both LES and PIV. The focus of this section was to utilise this established benchmark case of  $Re = 3900$  to investigate how well the current simulations and experiments reproduce previous findings. This provides a basis to investigate elliptical cylinders at  $Re=3900$ , which is still an open area for investigation. Generally, the methods used to study the circular case provided satisfactory results, so these methods will be utilised when studying the elliptical cases. To summarise, it is found that through this investigation that the differences between predictions based on the WALE and IDDES models were not significant, and they both showed a satisfactory match to previous work, especially after accounting for the slightly longer recirculation lengths predicted by these models. In addition, examining the predictions on a coarser mesh indicated that the mesh resolution is also satisfactory. The effect of spanwise domain size was also investigated, again showing only weak sensitivity, therefore, for the elliptical cases, a spanwise length of  $\pi D/2$  was selected alongside the WALE model for the simulations in the next chapter. Finally, PIV measurements in the FLAIR lab have validated the numerical results, and produced results that compare well with previous work. Similar experiments utilising PIV will be used to study the elliptical cases.

# Chapter 5

## The elliptical cylinder

### 5.1 Chapter overview

This chapter reports the key findings from studying the flow around elliptical cylinders simulated at  $Re = 3900$ . As mentioned previously, the focus of this study is to investigate how the variation of the aspect ratio of the body affect the different flow parameters such as drag coefficient, Strouhal number, and many other measures compared to the circular cylinder case reported in chapter 4.

#### 5.1.1 Varying the aspect ratio

For the simulations reported in this chapter, the Reynolds number was fixed at  $Re = 3900$  based on the fixed cross-stream major axis length. Figure 5.1 illustrates how varying this ratio affects the drag coefficient. It was observed that as the aspect ratio increases from a narrow cylinder to a circular cylinder, the drag coefficient decreases substantially. The measured drag coefficients have some uncertainty because there is considerable variation even over long times, as demonstrated in Figure 5.1(b), which shows the drag signal for the circular cylinder. The increase in drag at smaller aspect ratios can be attributed to the higher pressure on the front-facing surface and the low pressure at the rear relative to the reference case of the circular cylinder (as can be seen in Figure 5.3 below). For the case of  $AR = 0.10$ , the drag of  $C_D \simeq 1.9$  is almost a factor of 2 higher than the circular cylinder case. This figure also shows the approximate drag variation from Blevins (1984). The predicted drag values are a reasonable fit to this trend.

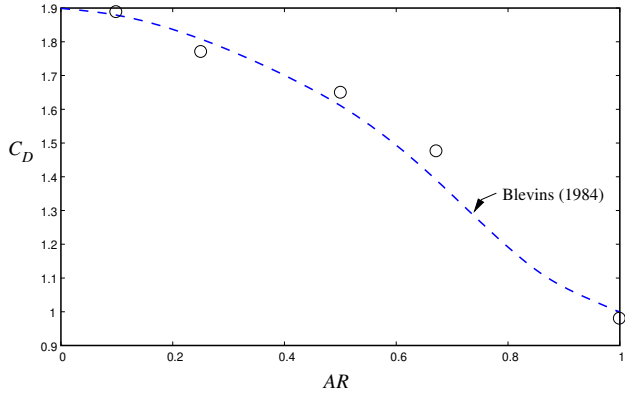


Figure 5.1: Variation of the mean drag coefficient with aspect ratio. The dashed blue line is a correlation provided by Blevins (1984). Circles are from the present predictions.

Figure 5.2 shows the corresponding effect on the Strouhal number with increasing aspect ratio. The trend is opposite to that of the drag coefficient. Thus, when the aspect ratio is increased, the Strouhal number increases. It can be observed that there is an approximately linear increase between the aspect ratio and the Strouhal number. Thompson et al. (2014) numerically modelled the flow past elliptical cylinders at low Reynolds numbers  $Re \leq 200$ . They found that even over this range the Strouhal numbers plateaued beyond critical Reynolds numbers to give a similar trend. For the cases of  $AR = 0.1$ ,  $0.25$  and  $0.5$ , at  $Re = 3900$ , these predicted values were slightly higher, although the trend to higher  $St$  at higher  $AR$  was the same.

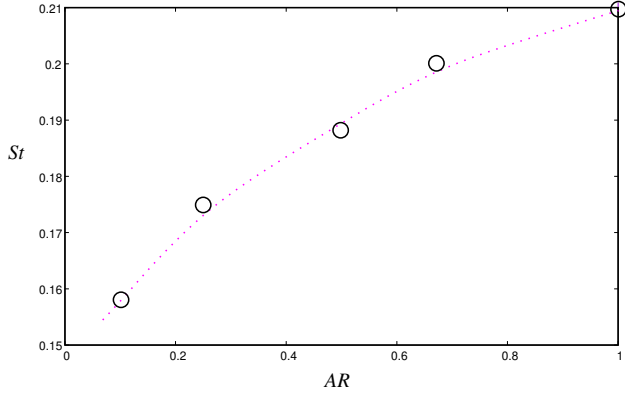


Figure 5.2: Plot of the Strouhal number variation with aspect ratio ( $AR = 0.10, 0.25, 0.50, 0.67, 1$ ). The dashed line is an approximate fit to the data.

Figure 5.3 shows plots of the pressure coefficient variation with angle around the surface of each cylinder. It was observed that the local minimum  $C_P$  was much lower than the circular cylinder for all the other elliptical cylinders. The trend was not monotonic, with the values for  $AR = 0.1\text{--}0.67$  clustering around -1.5. As discussed above, this variation may be a function of the time-averaging period, given the considerable variations in pressure over time. (Typical averaging periods are 100-250 time units, corresponding to 20-50 periods). The shapes of the curves are quite different, which is associated with the different cross-sectional shapes. The pressure on the front surface increases considerably as the aspect ratio is decreased, consistent with the expected behaviour, given the front surface becomes progressively flatter. On the other hand, the base pressure does not vary much over the aspect ratio in the range  $0.1 \leq AR \leq 0.67$ , with values in the range  $-1.40 \leq C_P \leq -1.25$ . In contrast, for the circular cylinder,  $C_P \simeq -0.90$ .

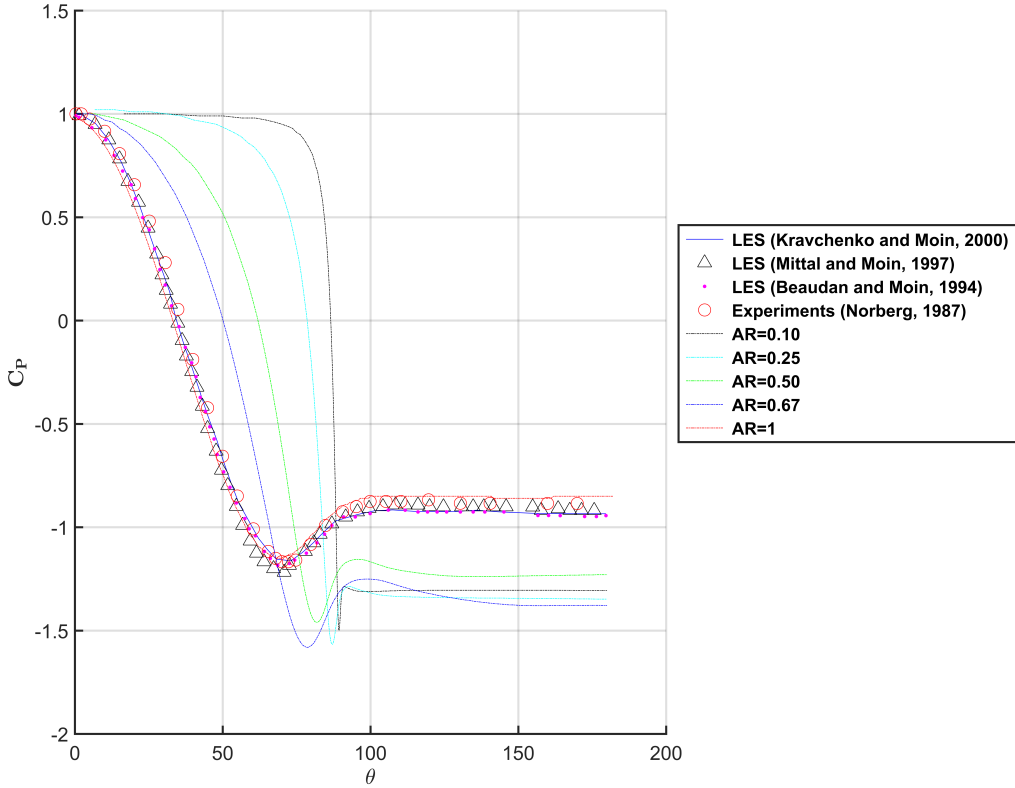


Figure 5.3: Plot of the time-mean pressure coefficient along the circumference of each elliptical cylinder.

Figure 5.4 shows time-averaged pressure contours for each elliptical cylinder in a  $X-Y$  plane. For the smallest  $AR$  ( $AR = 0.10$ ), the low pressure region inside the recirculation bubble is very close to the body compared to the  $AR = 1$  case, where this region is longer and more symmetric. Indeed, there do not appear to be strong noticeable differences between the near wake distributions for all the elliptical cylinder cases. The circular cylinder distribution is extended downstream compared to the other cases.

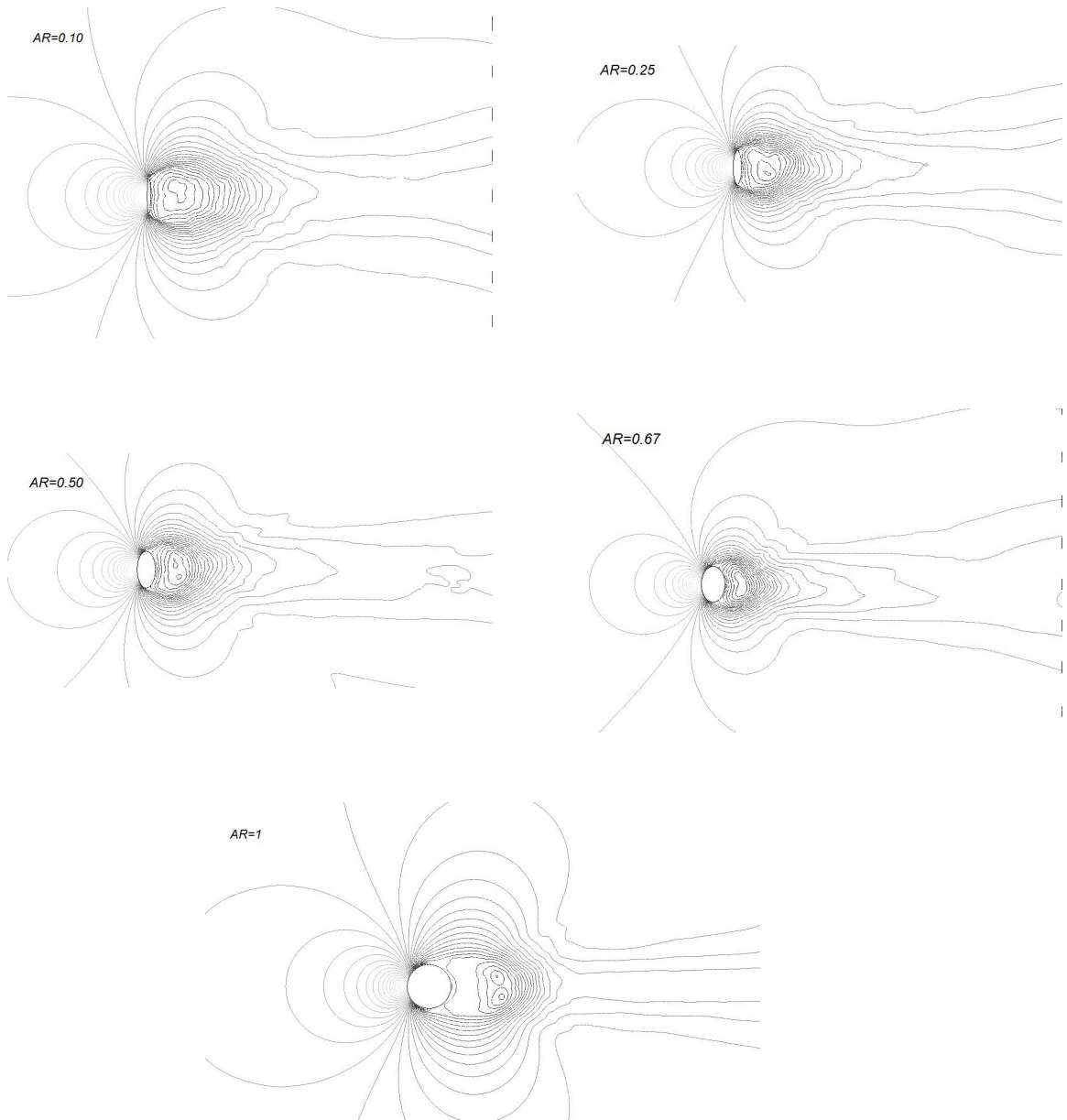


Figure 5.4: Contour plots of the time-mean pressure coefficient along the surface area of each elliptical cylinder.

Figure 5.5 shows the time and span-averaged streamwise velocity component along the centreline in the wake for each cylinder. In the near wake,

the downstream position of the minimum velocity occurs closest to the rear of the cylinder for  $AR = 0.67$ , moving further downstream for smaller aspect ratios. On the other hand, further downstream at  $X/D = 4$ , the wake recovery follows a monotonic trend with aspect ratio, with smaller aspect ratios having a higher wake deficit. In terms of the recirculation bubble length, as the aspect ratio becomes larger, the recirculation bubble length becomes shorter, except for the circular cylinder case. This behaviour seems surprising given the smooth and continuous change in geometry between the cylinders. The recirculation bubble lengths are summarised in Table 5.1.

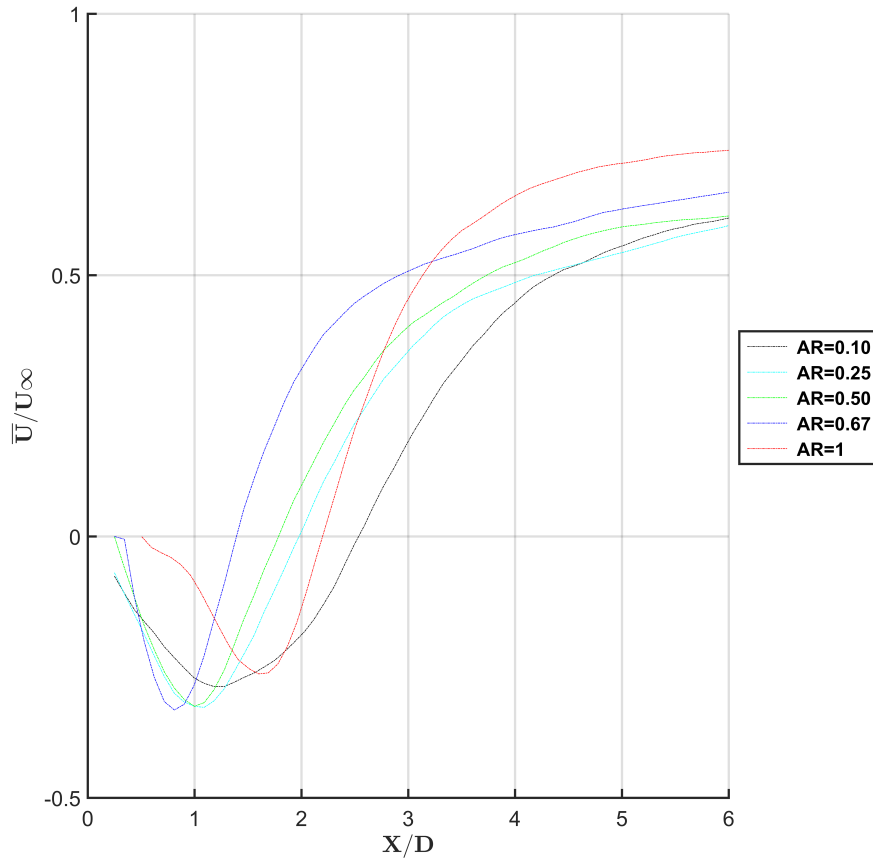


Figure 5.5: Plot of the time-mean streamwise velocity the surface area of each elliptical cylinder.

Table 5.1: Data for the recirculation bubble lengths of each  $AR$ .

<i>Aspect Ratio</i>	$L/D$ – bubble length
$AR = 0.10$	2.82
$AR = 0.25$	2.09
$AR = 0.50$	1.89
$AR = 0.67$	1.27

Figure 5.6 shows the time- and span-mean streamwise velocity at  $X/D = 1.56$ ,  $2.04$  and  $2.52$  measured from the centre of the body, as done for the circular cylinder in the previous chapter. Relative to the circular cylinder case, the shape of the time-mean velocity profiles in the near wake become more V-shaped instead of U-shaped. This is especially true for aspect ratios in the range  $0.25 \leq AR \leq 0.67$ , and is probably mainly due to the considerably shorter mean bubble lengths in these cases. Thus, there is also a reduction in the wake deficit for those aspect ratios as well. The lowest aspect ratio case of  $AR = 0.1$  appears to show slightly different behaviour, in that the wake deficit is higher than even the circular cylinder at these three downstream distances. The lower aspect ratio cases all show a wider wake structure, indicative of the separating shear layers flaring outwards relative to the circular cylinder case. This would appear to be consistent with the greater acceleration of the fluid over the top and bottom of the cylinder in the smaller aspect ratio cases.

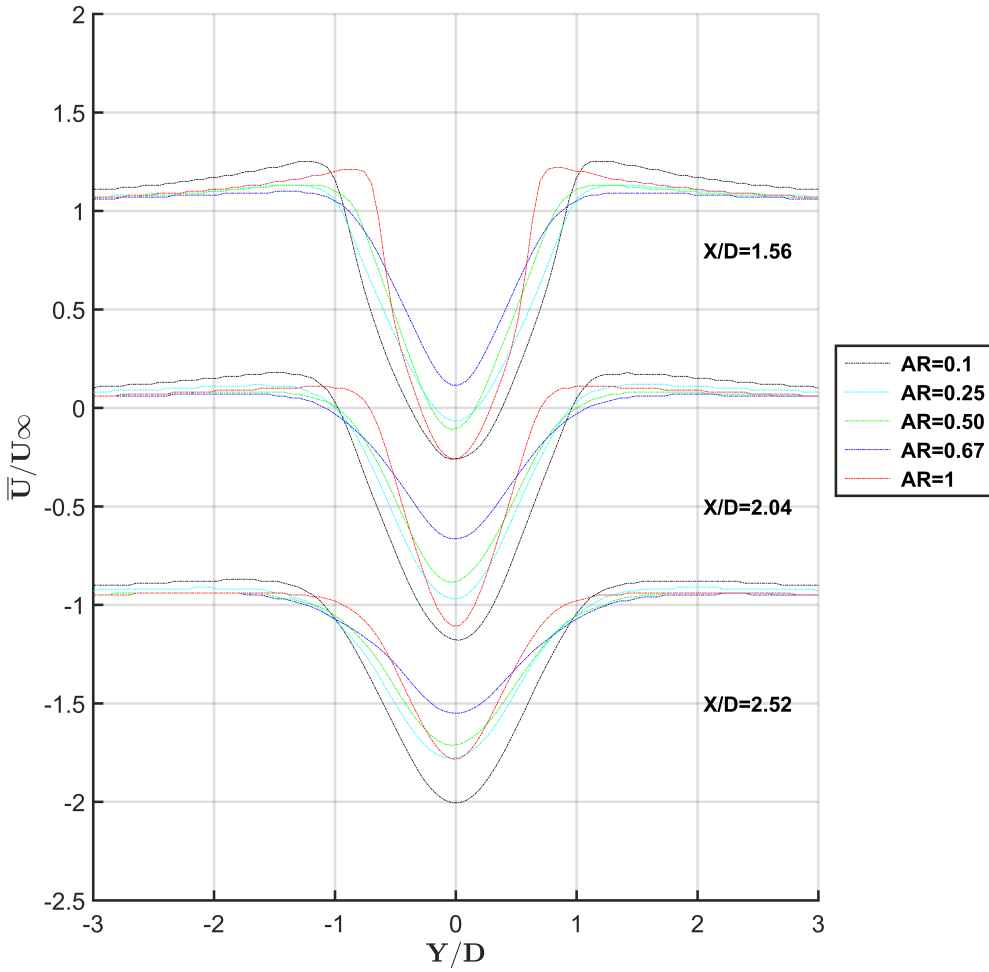


Figure 5.6: Plot of the time-mean streamwise velocity at  $X/D=1.56, 2.04, 2.52$  showing the numerical results for the elliptical cases.

Figure 5.7 represents the time- and span-mean cross-flow velocity component at  $X/D = 1.56, 2.04$  and  $2.52$  for all cases. At the distance of  $X/D = 1.56$ , for larger aspect ratio, the cross-flow velocity profile shows obvious minimum and maximum peaks. Interestingly, at the centreline of the wake ( $Y/D = 0$ ) for the case of  $AR = 1$ , there is a slight bend in the profile in contrast to the other cases. Again, this is likely due to the difference in the recirculation bubble length, which affects the profile shapes. (In the future, it might be beneficial to plot profiles along lines scaled in downstream

distance by the bubble length corresponding to each aspect ratio). Further downstream at  $X/D = 2.52$ , this bend disappears for all cases.

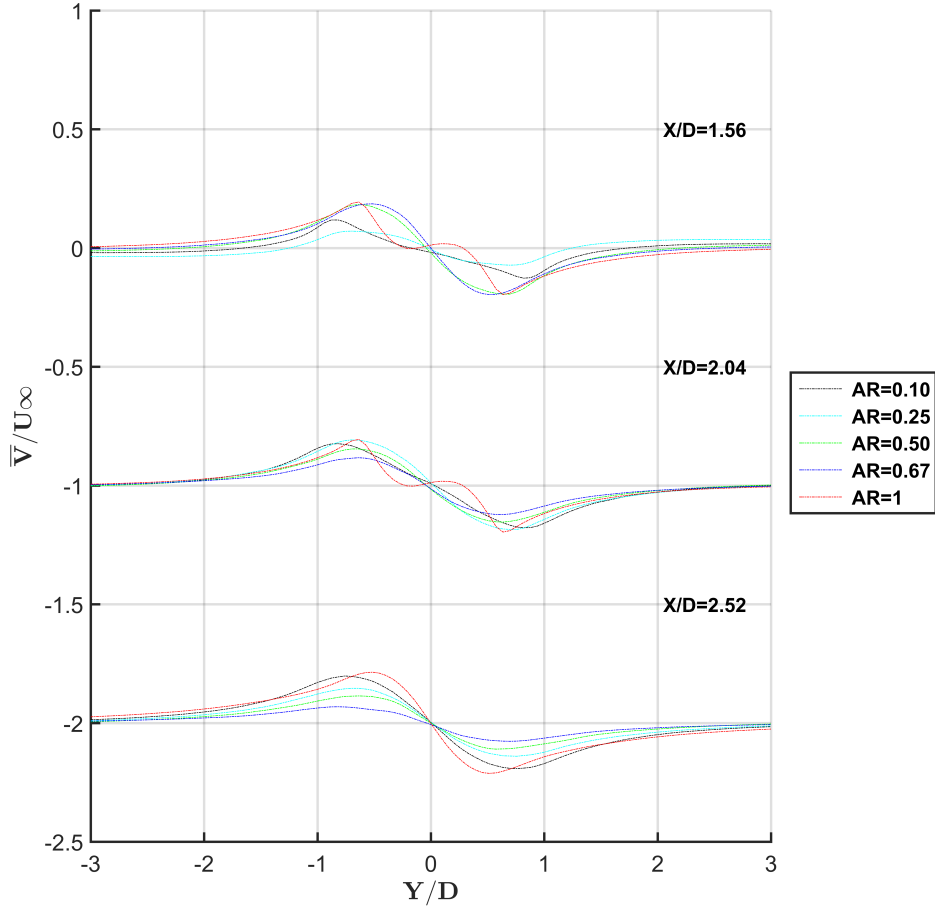


Figure 5.7: Plot of the time-mean cross-flow velocity at  $X/D=1.56, 2.04, 2.52$  showing the numerical results for the elliptical cases.

Figure 5.8 shows the variance of the streamwise velocity  $\overline{U'U'}/U_\infty^2$  at for the same downstream locations of  $X/D$ . The general trend shows an increase in  $AR$  leads to similarities in this Reynolds stress component when compared to the circular cylinder. As discussed previously, the appearance of peaks in the profiles is due to the transition of the shear layers. In addition, the overall shape of the profile is smallest for the circular cylinder case and

expands as  $AR$  decreases. This is associated with the wider wake at smaller aspect ratios, as discussed above.

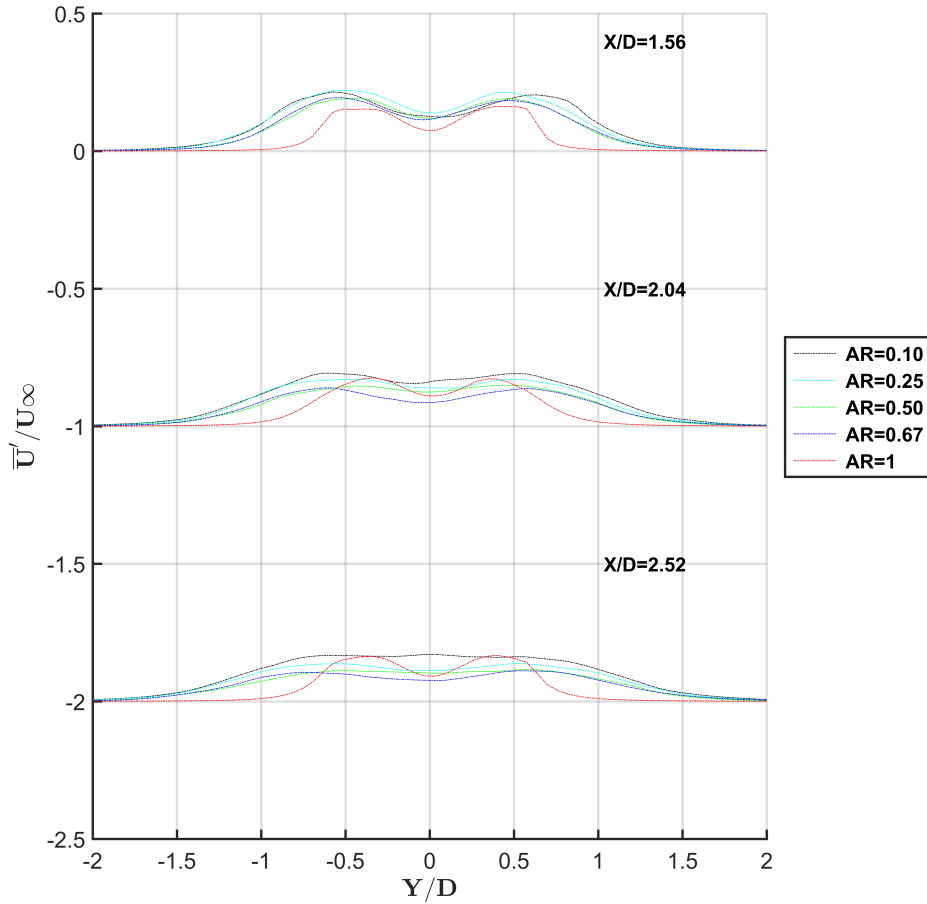


Figure 5.8: Plot of the  $\bar{U}'\bar{U}'/U_\infty^2$  Reynolds stress component at  $X/D = 1.56$  showing the numerical results for the elliptical cases.

Figure 5.9 shows the  $\bar{U}'\bar{V}'/U_\infty^2$  Reynolds stress component at the same downstream distances as for the other profile comparisons. At  $X/D = 1.56$ , the peaks for all elliptical cases are smoother than the circular cylinder case. Further downstream, these distributions are more similar.

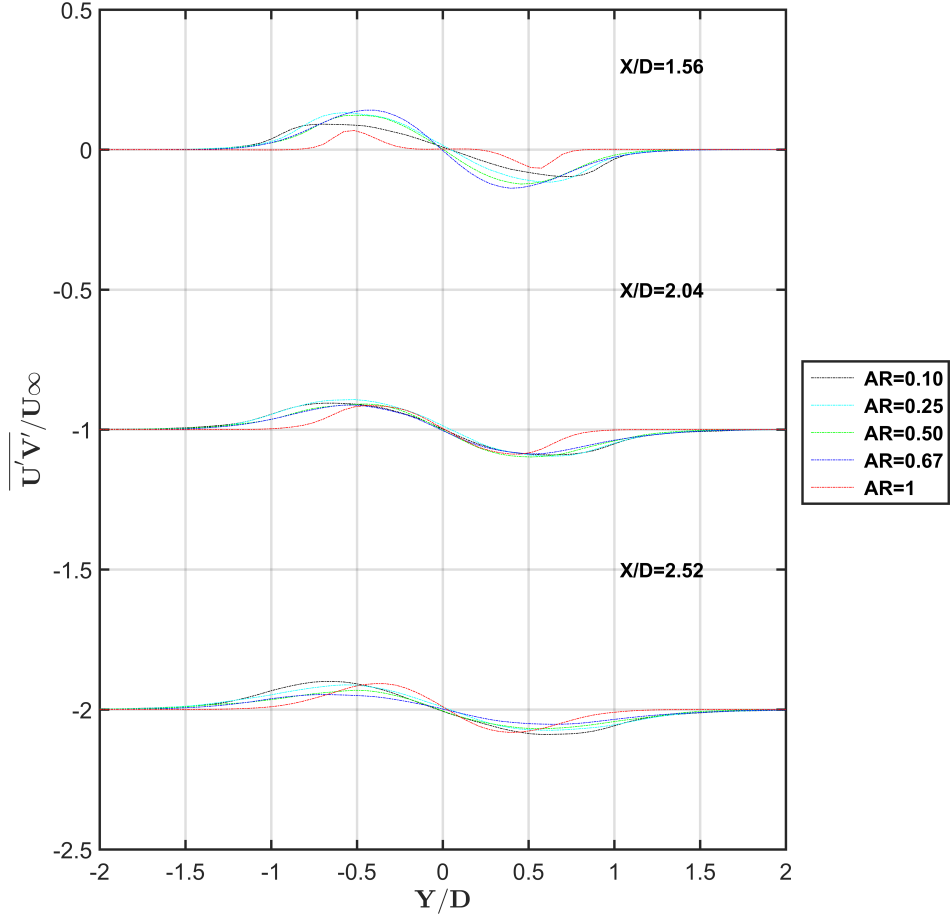


Figure 5.9: Plot of the Reynolds stress  $\overline{U'V'}/U_\infty$  at downstream distances  $X/D = 1.56, 2.04, 2.52$ .

Figure 5.10 shows the  $V'$  Reynolds stress component of each of the cases. The general trend for the profiles is that further downstream of the body, the maximum peaks becomes flatter and smoother, indicating the wider wakes for the elliptical cases compared to the circular cylinder case.

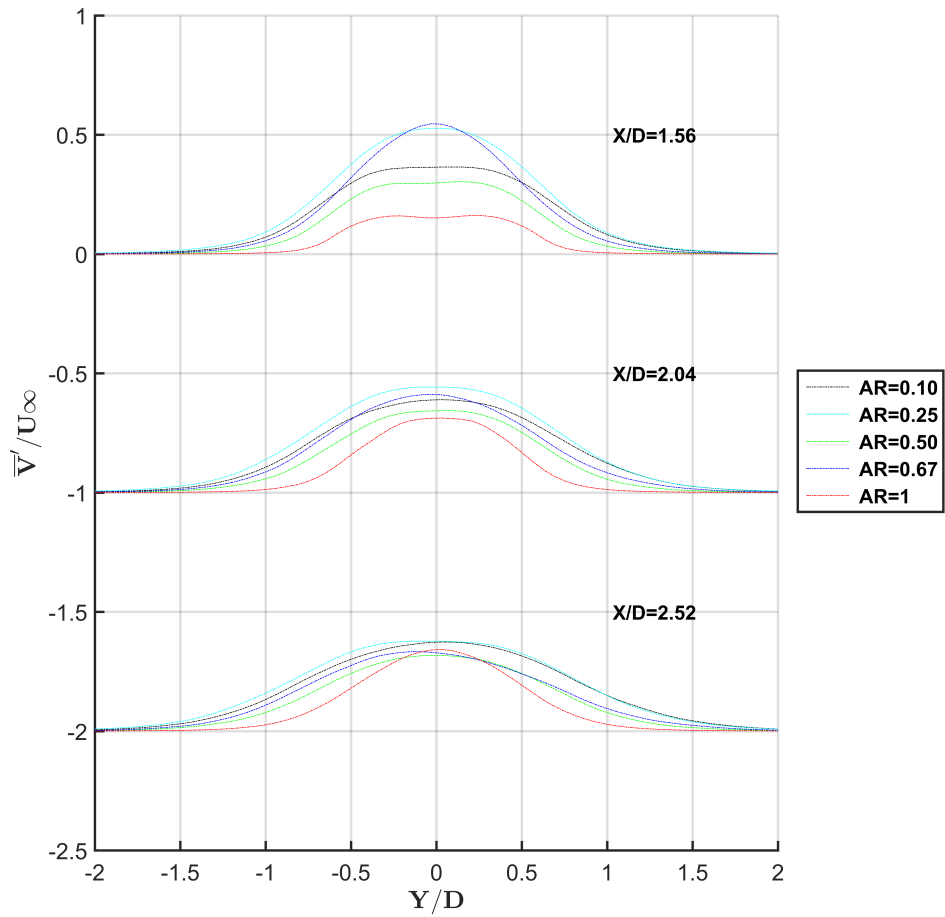


Figure 5.10: Plot of the numerical predictions of the  $\overline{V'V'}/U_\infty^2$  at  $X/D = 1.56, 2.04, 2.52$ .

Overall, this investigation attempts to quantify some of the trends of how the wake changes as the aspect ratio is changed. Although an analysis based on downstream profiles is often used to compare different simulation approaches or the match up with experiments, a variation of the predicted bubble length can make the comparisons difficult. The bubble length can be affected by oncoming turbulence and possibly cylinder smoothness in experiments, or a failures to predict the correct separation point in numerical simulations. This point will be partially addressed further below with comparisons of spanwise averaged fields.

The next section characterises the three-dimensional shedding in the wakes and reports on the variations observed between different elliptical cylinders.

### 5.1.2 Wake shedding patterns

This section reports the formation of vortex structures as the aspect ratio is varied at  $Re = 3900$ . Thompson et al. (2014) considered two-dimensional shedding around elliptical cylinders at low Reynolds number. A key finding was that the wake formation length (also known as recirculation length) continued to shorten as the aspect ratio was lowered. This was connected with stronger and more compact wake vortices producing a stronger and more persistent wake deficit. The current results at a higher Reynolds number seems to show that the wake formation behaviour is slightly different, especially since the formation length actually increases for the lowest aspect ratio case.

Figure 5.11 shows instantaneous vortex shedding patterns in an  $X$ - $Y$  plane. A noticeable observation is the occurrence of Kelvin-Helmholtz vortices that should be expected at this Reynolds number for all cases. These are especially prominent for the lower aspect ratio cases. It is also noticeable that the braid regions between the downstream spanwise rollers are more complex in the lower aspect ratio cases. It is also clear from these images that the formation region is cleaner for the circular cylinder. The separating shear layers also advect more at an angle to the downstream direction, as has been pointed out in previous discussions and analysis.

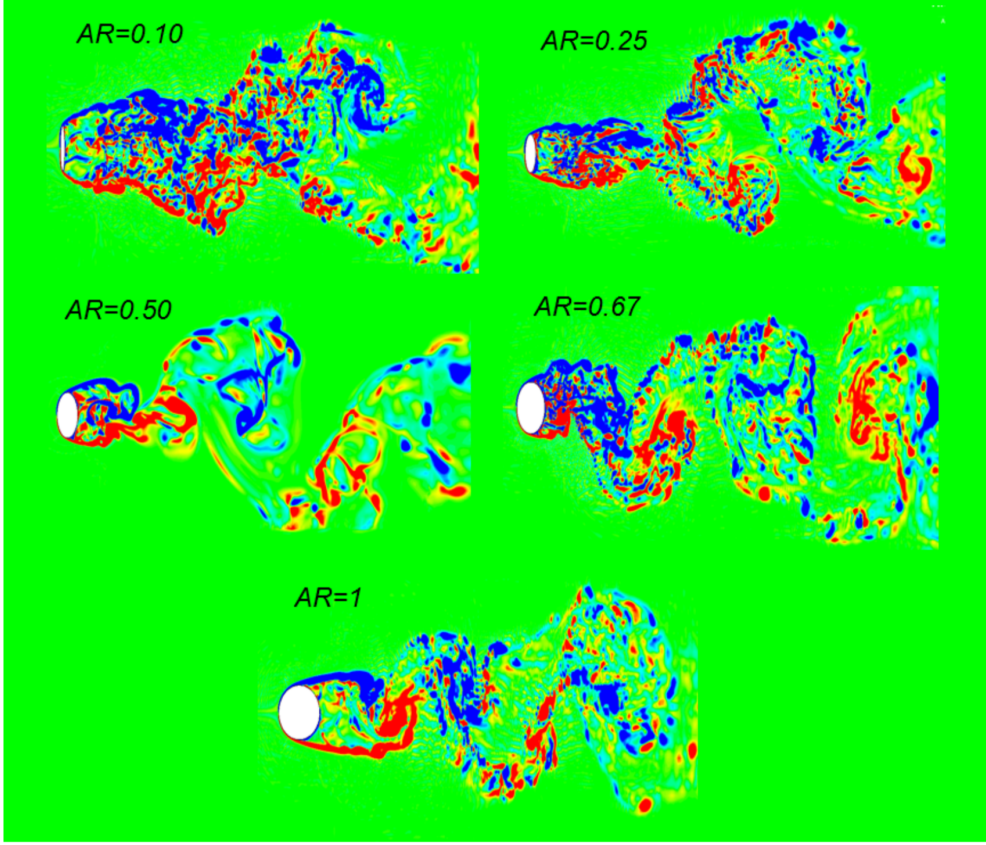


Figure 5.11: Vorticity contours of the elliptical bodies for  $AR=0.10, 0.25, 0.50, 0.67, 1$  at  $Re=3900$ .

### 5.1.3 Experiments based on PIV

PIV measurements of the flows past elliptical cylinders were obtained as part of the present study. Figure 5.12 presents the PIV measurements for the time-mean streamwise velocity for  $AR = 0.25, 0.50$  and  $1$ . The trends from these experiments are consistent with the numerical predictions of the streamwise velocity shown in Figure 5.5. In particular, the intermediate aspect ratio case ( $AR = 0.5$ ) has the shortest reattachment length and both elliptical cases have a stronger reverse flow than the circular cylinder case. In addition, further downstream at  $X/D = 4$  for example, the wake deficit increases with decreasing aspect ratio. The wake velocity at this point of  $U \simeq 0.5U_\infty$  for both elliptical cases, matches well with the numerical prediction. The

maximum reversed flow in the near wake is slightly underpredicted with the simulations.

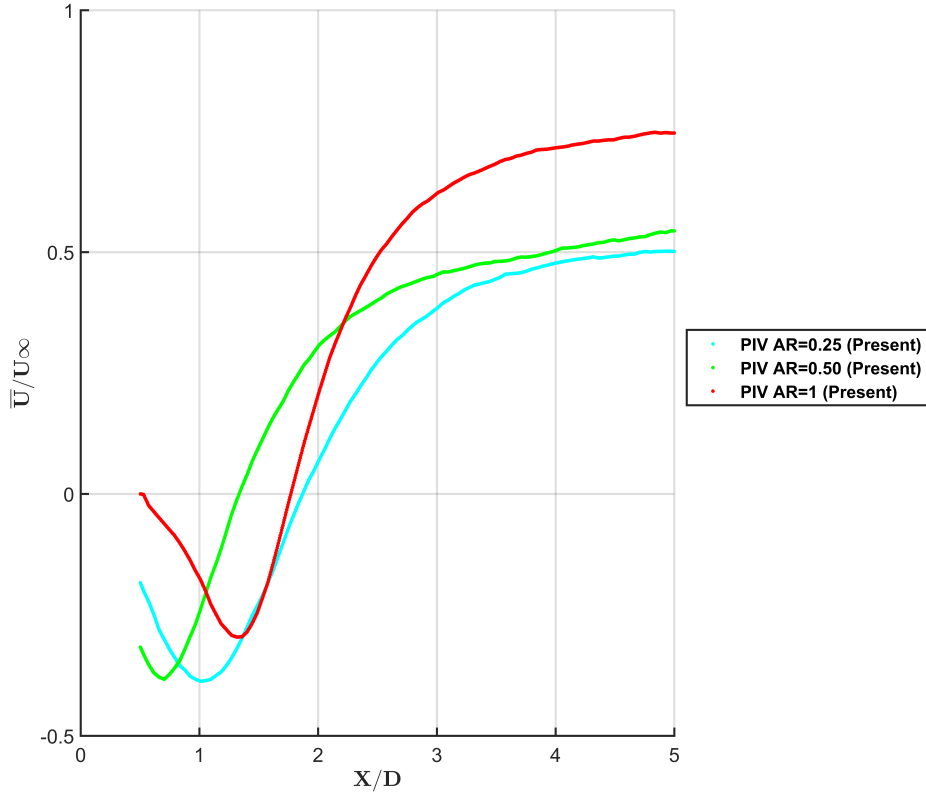


Figure 5.12: Plot of the time-mean streamwise velocity from PIV measurements for  $AR = 0.25, 0.50$  and  $1$ .

Figure 5.13 presents the time-mean streamwise velocity at  $X/D = 1.56$ ,  $2.04$  and  $2.52$  in the wake. Similar to the numerical results, the shape of these profiles expand as the aspect ratio becomes smaller, while the overshoot in the streamwise velocity beyond the shear layers is reduced at smaller aspect ratio. In addition, the shapes of these profiles near the cylinder changes from a U-shape to a V-shape as the aspect ratio is decreased. Further downstream, the V-shape is maintained regardless of the aspect ratio.

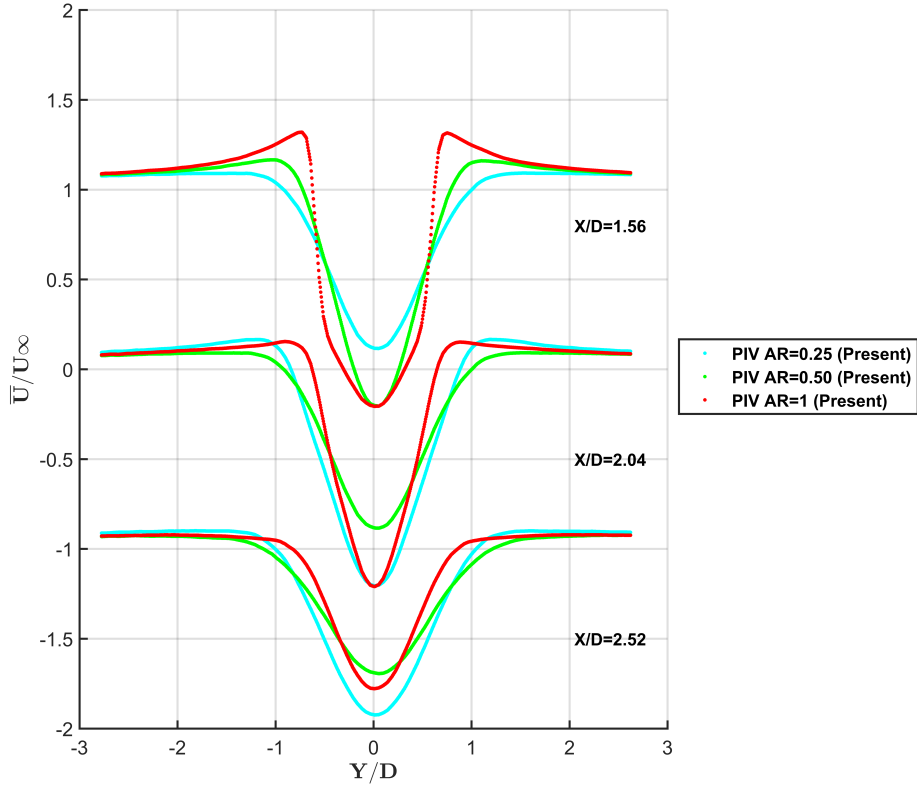


Figure 5.13: Plot of the time-mean streamwise velocity at  $X/D = 1.56, 2.04$  and  $2.52$  from PIV measurements for  $AR = 0.25, 0.50$  and  $1$ .

Figure 5.14 shows the time-mean cross-flow velocity from the PIV measurements at the same distances downstream. At  $X/D = 1.56$  for  $AR = 1$ , the peaks are higher compared to the numerical prediction shown in Figure 5.6. Consistent with the numerical results in the previous section, these peaks at this distance in the wake are more defined as  $AR$  increases. Further downstream, these peaks are sharper compared to the numerical results for the case of  $AR = 0.50$ . Finally, these peaks become smoother further downstream from the body. However, overall, the trends of these measurements are consistent with the numerical results reported previously.

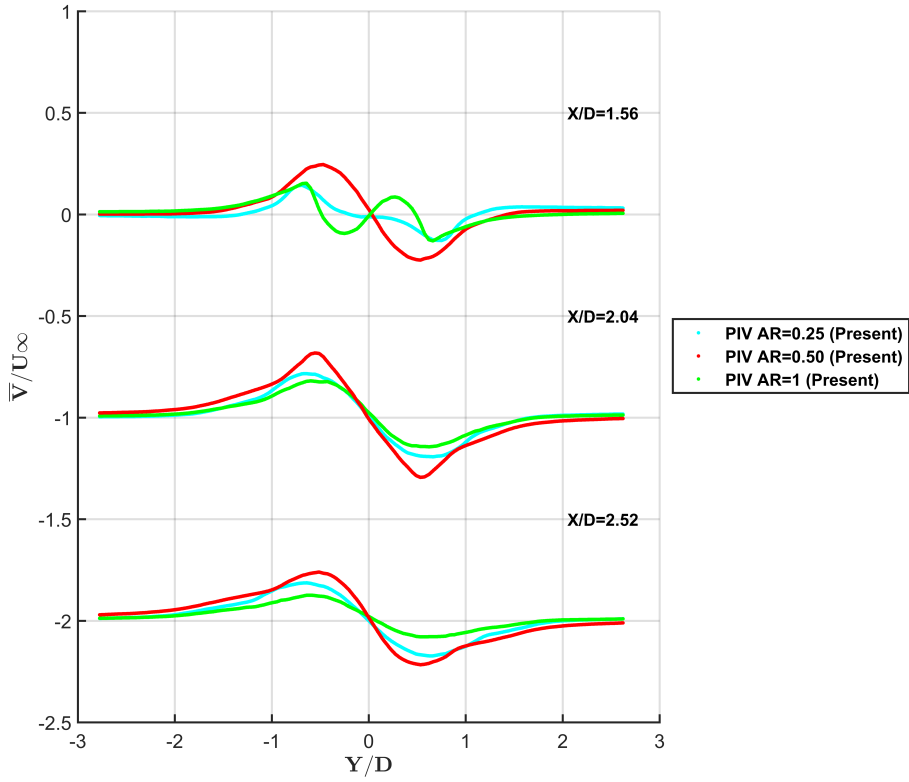


Figure 5.14: Plot of the time-mean cross-flow velocity at  $X/D = 1.56$ , 2.04 and 2.52 from PIV measurements for  $AR = 0.25$ , 0.50 and 1.

Figure 5.14 shows the profiles for the  $\overline{U'U'}$  Reynolds stress component. For  $AR = 0.25$  and 0.50, there are two smooth peaks compared to the more complex behaviour for  $AR = 1$ ; these peaks develop to a sharper shape at  $X/D = 1.56$ . Further downstream, the peaks are less defined for  $AR = 0.25$  and 0.50, and the profile of the variance is wider than the case of  $AR = 1$ . Even further downstream at  $X/D = 2.52$ , these peaks are less defined than further upstream. Again, the width of the distributions and general trends match the numerical predictions reasonably well.

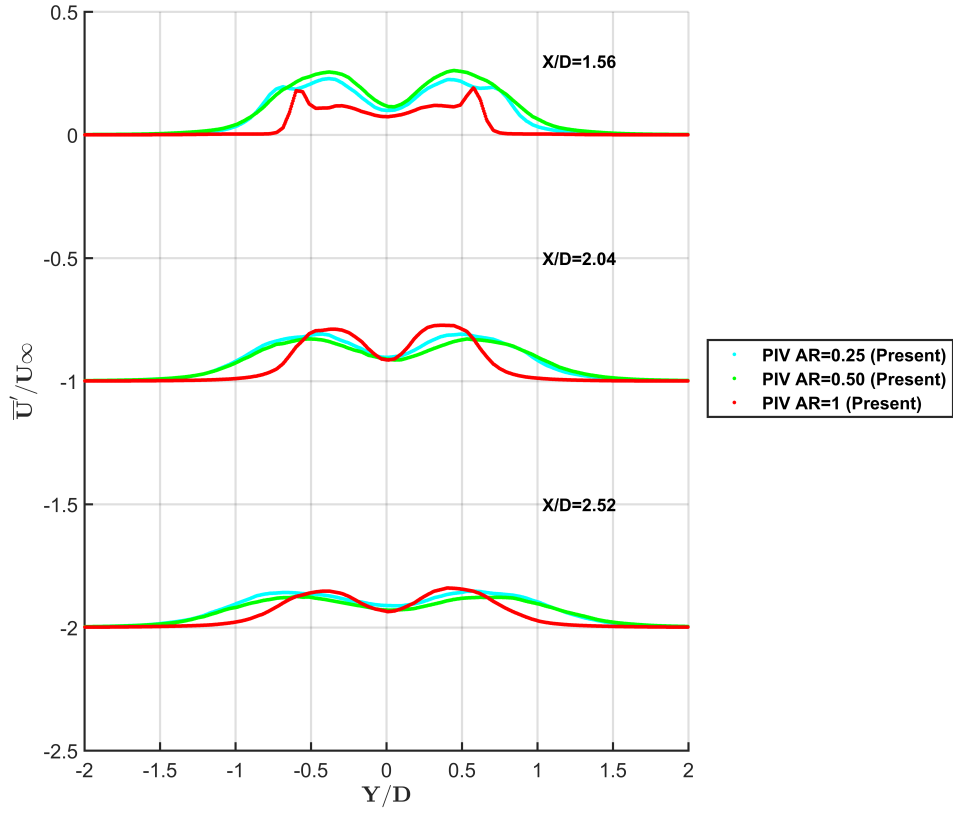


Figure 5.15: Plots of the  $\overline{U'U'}/U_\infty^2$  from PIV measurements for  $AR = 0.25, 0.50, 1$ .

Figure 5.15 shows the profiles of the  $\overline{V'V'}$  stress component at the same distances. At  $X/D = 1.56$ , the peak for  $AR=0.50$  is larger than the numerical prediction for the same aspect ratio, while for the  $AR = 0.25$  case the opposite is true. However further downstream at  $X/D = 2.52$ , the three profiles show a similar magnitude of about 0.4. This, together with the increased spread for the lower aspect ratio cases, are consistent with these trends observed for the numerical predictions shown in Figure 5.10.

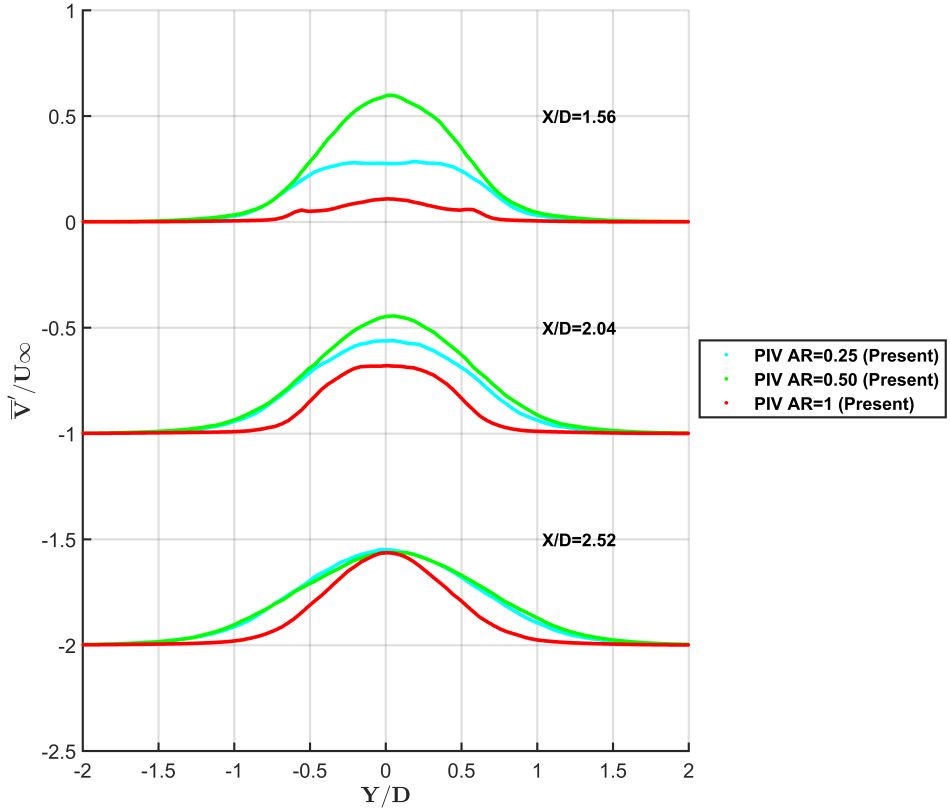


Figure 5.16: Plots of the  $\overline{V'V'}/U_\infty^2$  Reynolds stress component from PIV measurements for  $AR = 0.25, 0.50$  and  $1$ .

Figure 5.17 shows profiles of the  $\overline{U'V'}/U_\infty^2$  Reynolds stress component. In a sense, the  $AR = 0.25$  and  $1.0$  cases have more in common than the intermediate  $AR = 0.5$  case, which shows a smoother less peaked distribution. This is consistent with the shorter formation length for the  $AR = 0.5$  case, seen in the experiments. The distributions become more similar further downstream, consistent with the trend seen with the simulation results.

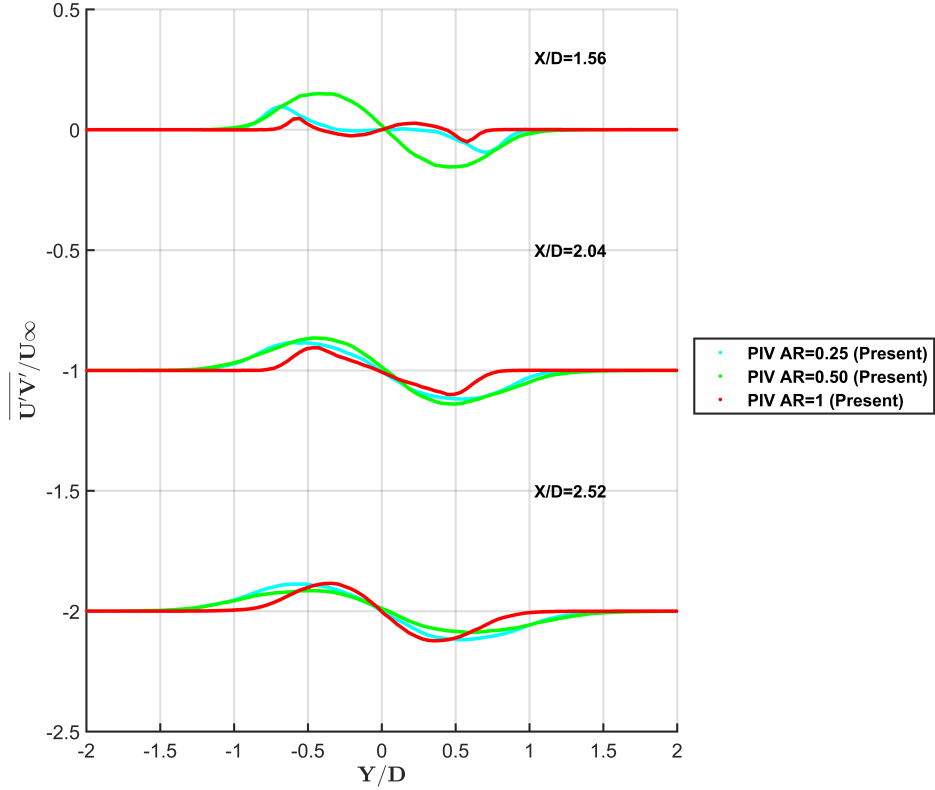


Figure 5.17: Plots of the  $\overline{U'V'}/U_\infty^2$  Reynolds stress component from PIV measurements for  $AR = 0.25, 0.50$  and  $1$ .

Generally, these results show trends similar to the numerical results, although there are some differences in some details. As has been pointed out, differences in the formation length due to various reasons, will accentuate differences in the near wake profile plots. To help to remedy this situation, the following section presents some of the data as contour plot comparisons between the experiments and the numerical simulations.

## 5.2 Field comparisons between experiments and simulations

As indicated above, this section presents direct comparisons between time- and span-averaged fields of various velocity and turbulence components to provide a more visually interpretable comparison of the datasets. The contour level ranges are kept consistent between simulation and experimental fields, although the colour maps are varied, due to the different plotting packages used to present the data.

### 5.2.1 Streamwise velocity comparisons

Figure 5.18 shows a comparison of the time- and span-averaged streamwise velocity field in the near wake. The experimental result is on the left and the prediction on the right. Three aspect ratios are shown:  $AR = 1.00$  (top);  $AR = 0.50$  (middle) and  $AR = 0.25$  bottom. The comparison between the experiments and the simulations is good, with the shape and the magnitude of the distributions match well and well as the position of the extreme values. The simulation for  $AR = 0.50$  is the least good match with the experimental field, in particular, the location of the minimum streamwise velocity is further downstream for the numerical prediction.

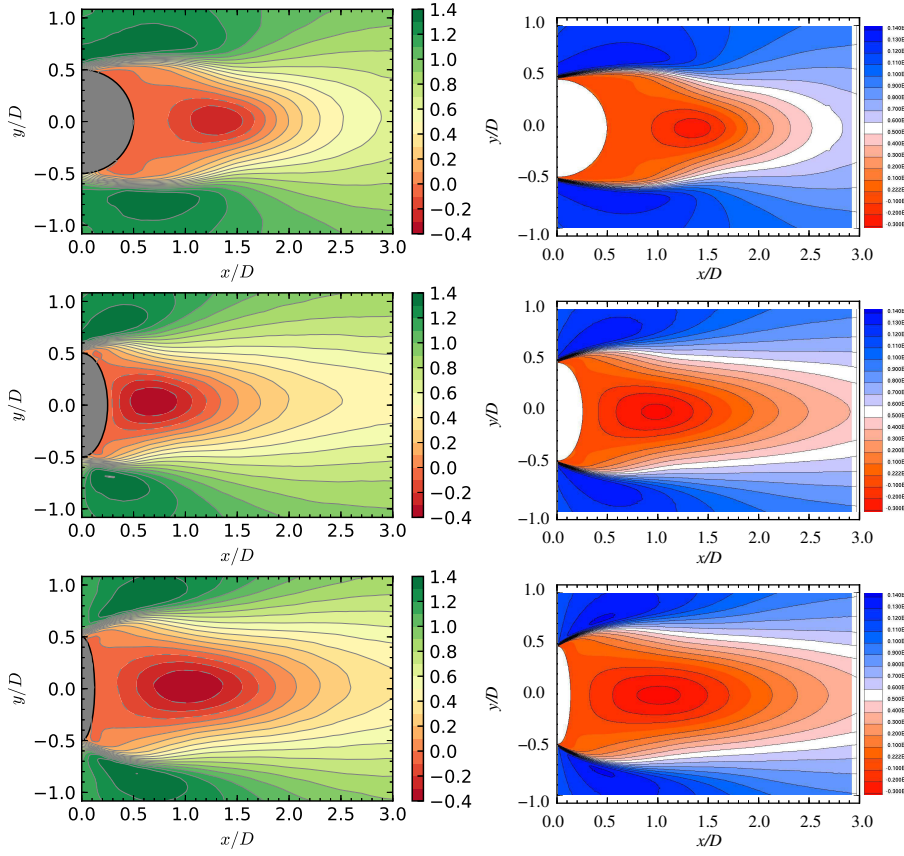


Figure 5.18: Plots of the time- and span-averaged streamwise velocity fields downstream of the cylinders. Top to bottom:  $AR = 1.0$ ,  $0.5$  and  $0.25$ ; left to right: experimental and simulation results.

### 5.2.2 Cross-stream velocity comparisons

Figure 5.19 shows a similar comparison for the near-wake cross-stream velocity fields. Again the match is good between the experiments and the simulations. The general variation is picked up well, as is the location of the maximum and minimum values. Once again, the near-wake for the  $AR = 0.50$  is slightly different, reflecting the result for the streamwise velocity component.

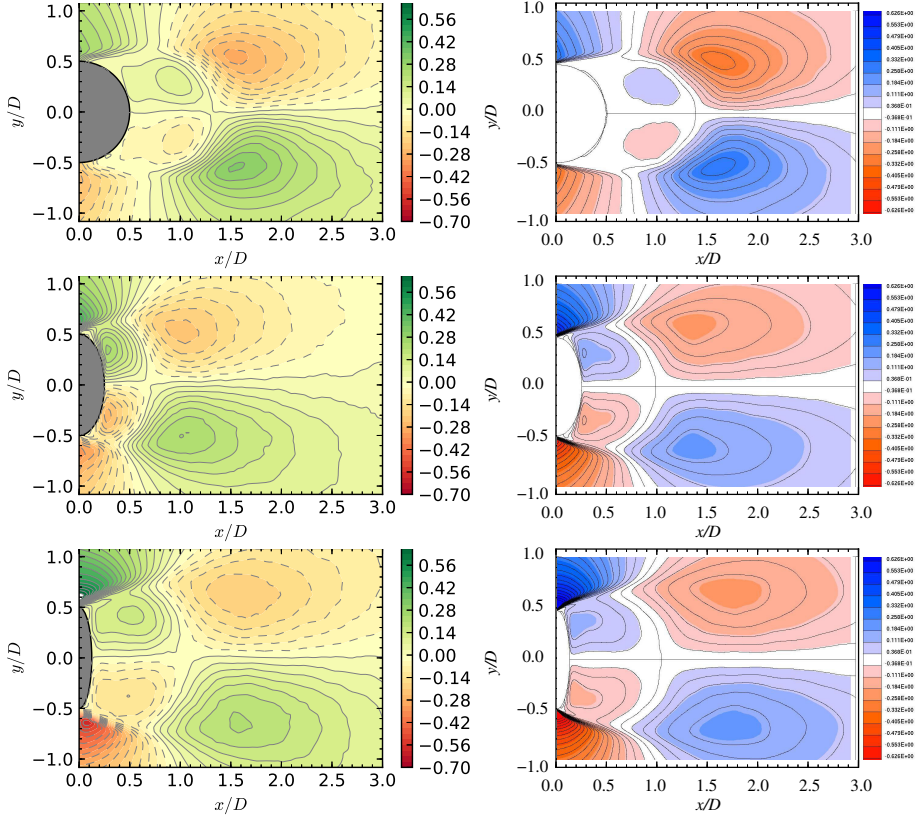


Figure 5.19: Plots of the time- and span-averaged cross-stream velocity fields downstream of the cylinders. Top to bottom:  $AR = 1.0, 0.5$  and  $0.25$ ; left to right: experimental and simulation results.

### 5.2.3 $\overline{U'V'}$ Reynolds stress comparison

Finally, the Reynolds stress distribution comparison is shown in Figure 5.20. Once again, the overall distributions match well both in magnitude, location of the extrema, and general shapes of the distributions. Thus, it appears that the numerical simulations capture the turbulent flow evolution reasonably well over a range of aspect ratios leading to variation in drag by a factor of two.

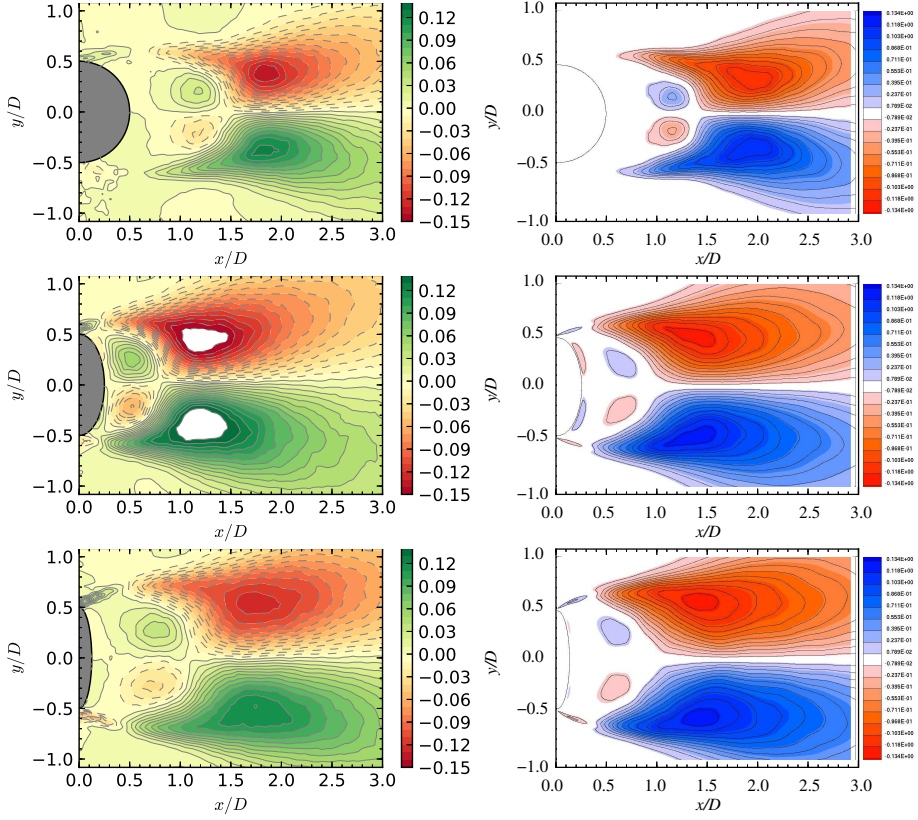


Figure 5.20: Plots of the time- and span-averaged  $\overline{U'V'}/U_\infty^2$  Reynolds stress component downstream of the cylinders. Top to bottom:  $AR = 1.0, 0.5$  and  $0.25$ ; left to right: experimental and simulation results.

### 5.3 Chapter summary

This chapter provides a detailed investigation of the flow past elliptical cylinders of different aspect ratios both numerically and experimentally. The wake properties were compared with those of a circular cylinder reported on in the previous chapter. Some conclusions of the study are as follows. Firstly, it was found that as  $AR$  increases, the wake state becomes similar to the circular cylinder case of  $AR = 1$ . However, even for elliptical cylinders of aspect ratio 0.67 there is substantial change in the downstream wake profile, Reynolds stress components and pressure distribution. In addition, the shedding of the flow becomes more chaotic and occurs closer to the elliptical body as

the aspect ratio becomes smaller. This study provides a basis for future investigations involving the elliptical cylinder under these higher Reynolds numbers and above. Chapter 6 provides a brief conclusion to this study and the limitation that exist from the present investigations.

# Chapter 6

## Conclusions and future work

### 6.1 Summary of key findings

The present work was an investigation of the flow around elliptical cylinders with different aspect ratios at  $Re = 3900$ . The comparison of numerical measurements and experimental predictions with previous works was undertaken for the reference case of a circular cylinder wake. Overall, the quality of the match was similar to that of previously published works. The simulations and experiments were then extended to elliptical cylinders with the major axis aligned in the cross-stream direction. Only aspect ratios between 0.1 and 1.0 were considered, but noting that there is a significant change in the wake state as the aspect ratio is varied. Noticeably, the turbulent simulations and experiments showed some significant changes with aspect ratio including: considerable flaring of the wake outwards from the centreline relative to the circular cylinder, and an initial shortening and then a lengthening of the formation region as  $AR$  was decreased. The experimental measurements of the wake obtained from 2D PIV in a cross-stream plane and the numerical wake predictions aligned well. Contour plots of the time-averaged flow and Reynolds stress fields in particular showed good consistency.

### 6.2 Contribution of the thesis

As far as the candidate is aware, the study of the turbulent flow past the elliptical cylinder at  $Re = 3900$  has not been investigated in detail previously. The chosen Reynolds number is high enough for the wake to develop

Kelvin-Helmholtz vortices in the separating shear layers but well below the Reynolds number range of the drag crisis. It is also high enough to display a reasonable inertial subrange in the downstream turbulence spectra, which was captured with the simulations. As indicated above, it is an interesting problem in its own right considering the significant changes in the wake state with aspect ratio that have been observed in lower Reynolds number studies. The study provides two new datasets for this geometry from the simulations and experiments. This study may be applicable to industrial applications that do not always use circular cross-sectional cylindrical components.

### 6.3 Possible future work

There are a couple of interesting aspects that deserve further attention. One is that there is still a reasonable variation between predicted (and experimental) recirculation zone lengths for the circular cylinder wake in the literature. It is clear from this study, that the drag signal has considerable variation with time. Indeed as shown in chapter 4, the signal shows long periods at predominately low or high drag values. These states correspond to states of longer and shorter mean recirculation zones. Thus, even reasonably long averaging times of tens of shedding periods may still produce variations in predictions. This aspect could be investigated further.

Another interesting point is the effect of oncoming flow turbulence level. Wind tunnels and water channels have typical turbulence levels between 0.1% and 1%. The water tunnel used for the present PIV experiments had a turbulence level of approximately 1%. Thus, it would be useful to investigate the effect on time dependence turbulence at the inlet. This can be treated in the ANSYS commercial software using synthetic turbulence generators or using zonal methods where an upstream RANS zone can produce *turbulence* to feed time-dependent turbulence at the entry to an LES zone. Again, this would form an interesting further study.

# References

- Arat, H. T., Karakus, C., Koc, A., Baltacioglu, E. (2012) *Experimental investigation of flow structure over an elliptical cylinder located between two parallel plates by using PIV technique*, 6th International Ege Energy Symposium and Exhibition, 2012 Izmir, Turkey.
- Badr, H. (1997) *Oscillating inviscid flow over elliptic cylinders with flat plates and circular cylinders as special cases*. Ocean Engineering, 21(1), pp. 105-113.
- Bai, W., Mingham, C., Causon, D. & Qian, L. (2016) *Detached eddy simulation of turbulent flow around square and circular cylinders on Cartesian cut cells*. Ocean Engineering, 117, pp. 1-14.
- Beaudan, P. & Moin, P. (1994) *Numerical experiments on the flow past circular cylinder at sub-critical Reynolds number*. Report No. TF-62, Department of Mech. Engr., Stanford University.
- Bishop, R. & Hassan, A. (1964) *The lift and drag forces on a circular cylinder oscillating in a flowing fluid*. The Royal Society Publishing, 277(1368), pp. 32-50.
- Blackburn, H. M. & Schmidt, S. (2001) *Large eddy simulation of flow past a circular cylinder*. 14th Australian Fluid Mechanics Conference, 2001, Adelaide, Australia.
- Blevins, R., D. (1984) *Applied Fluid Dynamics Handbook*. Van Nostrand Reinhold Co., New York.

Breuer, M. (1998) *Large eddy simulation of the subcritical flow past a circular cylinder: numerical and modeling aspects*. International Journal for Numerical Methods in Fluids, 28(9), pp. 1281-1302.

Breuer, M., Jaffrézic, B. & Arora, K. (2007) *Hybrid LES–RANS technique based on a one-equation near-wall model*. Theoretical and Computational Fluid Dynamics, 22(3-4), pp. 157-187.

Catalano, P., Wang, M., Iaccarino, G. & Moin, P. (2003). *Numerical simulation of the flow around a circular cylinder at high Reynolds numbers*. International Journal of Heat and Fluid Flow, 24(4), pp. 463-469.

Choi, J. H., & Lee, S. J., (2000) *Ground effect of flow around an elliptic cylinder in a turbulent boundary layer*. J. Fluid Struct., 14(5), pp. 697–709.

Constant, E., Favier, J., Meldi, M., Meliga, P. & Serre, E. (2017). *An immersed boundary method in OpenFOAM : Verification and validation*. Computers and Fluids, 157, pp. 55-72.

Courant, R., Friedrichs, K., Lewy, H., (1928) *On the partial difference equations of mathematical physics*. AEC Research and Development Report, NYO-7689, AEC Computing and Applied Mathematics Centre – Courant Institute of Mathematical Sciences, pp. 215-234.

D'Alessandro, V., Montelpare, S. & Ricci, R. (2016) *Detached-eddy simulations of the flow over a cylinder at  $Re = 3900$  using OpenFOAM*. Computers and Fluids, 136, pp. 152-169.

Daoud, S., Nehari, D., Aichouni, M. & Nehari, T. (2016) *Numerical simulations of an oscillating flow past an elliptic cylinder*. Journal of Offshore Mechanics and Arctic Engineering, 138(1), pp. 011802.

Dogan, S., Canli, E., Ozgoren, M., Solmaz, O., Ozseker, G. (2015) *Comparison of flow structures around circular and elliptical cylinders*. 6th International Congress of Energy and Environment Engineering and Management, 2015, Paris, France.

Dong, S., Karniadakis, G., Ekmekci, A. & Rockwell, D. (2006) *A combined*

*direct numerical simulation–particle image velocimetry study of the turbulent near wake.* Journal of Fluid Mechanics, 569, pp. 185-207.

Elbatran, A. (2016) *DES of the turbulent flow around a circular cylinder of finite height.* Journal of Naval Architecture and Marine Engineering, 13(2), pp. 179-188.

Fonseca, F., B., Mansur, S., S., Vieira, E. (2013) *Flow around elliptical cylinders in moderate Reynolds numbers.* 22nd International Congress of Mechanical Engineering, 2013, Ribeirão Preto, Brazil.

Fornberg, B. (1979) *A numerical study of 2-D turbulence.* Journal of Computational Physics, 25(1), pp. 1-31.

Fouras, A., Lo Jacono, D. & Hourigan, K. (2008) *Target-free stereo PIV: a novel technique with inherent error estimation and improved accuracy.* Experiments in Fluids, 44(2), pp. 317-329.

Fouras, A. & Soria, J. (1998) *Accuracy of out-of-plane vorticity measurements derived from in-plane velocity field data.* Experiments in Fluids, 25(5-6), pp. 409-430.

Fröhlich, J. & von Terzi, D. (2008) *Hybrid LES/RANS methods for the simulation of turbulent flows.* Progress in Aerospace Sciences, 44(5), pp. 349-377.

Gallardo, J., Andersson, H. & Pettersen, B. (2016) *Three-dimensional instabilities in oscillatory flow past elliptic cylinders.* Journal of Fluid Mechanics, 798, pp. 371-397.

Germano, M. (1992) *Turbulence: the filtering approach.* Journal of Fluid Mechanics, 238(1), pp. 325-336.

Ghosal, S. & Moin, P., (1995) *The basic equations for the large eddy simulation of turbulent flows in complex geometry.* Journal of Computational Physics, 118(1), pp. 24-37.

Gsell, S., Bourguet, R. & Braza, M. (2018) *Three-dimensional flow past a fixed or freely vibrating cylinder in the early turbulent regime.* Physical Re-

view Fluids, 3(1). pp. 013902.

Gus'kuva, N. Yu., Makhortykh, G. V., & Shcheglova, M. G. (1998) *Inertia and drag of elliptic cylinders oscillating in a fluid*. Fluid Dyn., 33(1), pp. 91–95.

Hong, R., Xia, Z., Shi, Y., Xiao, Z. & Chen, S. (2014) *Constrained large-eddy simulation of compressible flow past a circular cylinder*. Communications in Computational Physics, 15(2), pp. 388-421.

Hunt, J., C., R., Wray, A., A., Moin, P. (1988) *Eddies, streams and convergence zones in turbulent flows*, Center for Turbulent Research, pp. 193-208. Proceedings of the Summer Program 1988.

Inverno, J., Neves, M., Didier, E. & Lara, J. (2016) *Numerical simulation of wave interacting with a submerged cylinder using a 2D RANS model*. Journal of Hydro-environment Research, 12, pp. 1-15.

Jakirlić, S. and Maduta, R. (2012) *Sensitized-RANS modelling of turbulence: resolving turbulence unsteadiness by a (near-wall) Reynolds stress model*, Progress in wall turbulence 2: understanding and modelling, pp. 17-35. Proceedings of the ERCOFTAC Workshop on Progress in Wall Turbulence Lille, France, 2014, Stanislas, Michel, Jimenez, Javier, Marusic, Ivan (Eds.).

Johnson, S., Thompson, M. & Hourigan, K. (2004) *Predicted low frequency structures in the wake of elliptical cylinders*. European Journal of Mechanics, 23(1), pp. 229-239.

Kamali-Moghadam, R., Javadi, K. & Kiani, F. (2016) *Assessment of the LES-WALE and zonal-DES turbulence models in simulation of the flow structures around the finite circular cylinder*. Journal of Applied Fluid Mechanics, 9(2), pp. 909-923.

Kim, W., Lee, J. and Choi, H. (2016) *Flow around a helically twisted elliptic cylinder*. Phys. Fluids, 28(5), pp. 053602.

Khan, N., Jameel, M., Badry, A., Zainah, I. (2016) *Numerical study of flow around a smooth circular cylinder at Reynolds number  $Re=3900$  with large*

*eddy simulation using CFD code.* ASME 2016 35th International Conference on Ocean, Offshore and Arctic Engineering, Busan, South Korea.

Kravchenko, A. & Moin, P. (2000) *Numerical studies of flow over a circular cylinder at  $Re_D=3900$ .* Physics of Fluids, 12(2), pp. 403-417.

Kurien, S., Taylor, M. (2005) *Direct numerical simulation of turbulence: data generation and statistical analysis.* Los Alamos Science, 29, pp. 142-151.

Lübcke,H., Schmidt, St., Rung, T., Thiele, F. (2001) *Comparison of LES and RANS in bluff body flows.* Journal of Wind Engineering and Industrial Aerodynamics, 89(14-15), pp. 1471-1485.

Lee, A., Campbell, R. & Hambric, S. (2014) *Coupled delayed-detached-eddy simulation and structural vibration of a self-oscillating cylinder due to vortex-shedding.* Journal of Fluids and Structures, 48, pp. 216-234.

Leontini, J., Lo Jacono, D. & Thompson, M. (2015) *Stability analysis of the elliptic cylinder wake.* Journal of Fluid Mechanics, 763, pp. 302-321.

Loureco, L. M. & Shih, C., *Characteristics of the plane turbulent near wake of a circular cylinder; a particle image velocimetry study* (data taken from Beaudan and Moin 1994).

Lugt, H. & Haussling, H. (1974) *Laminar flow past an abruptly accelerated elliptic cylinder at  $45^\circ$  incidence.* Journal of Applied Mechanics, 45(1), pp. 711-734.

Luo, Z., Teng, F. & Di, Z. (2014) *A POD-based reduced-order finite difference extrapolating model with fully second-order accuracy for non-stationary Stokes equations.* International Journal of Computational Fluid Dynamics, 28(6-10), pp. 428-436.

Lysenko, D., Ertesvåg, I. & Rian, K. (2013) *Large-eddy simulation of the flow over a circular cylinder at Reynolds number  $2 \times 10^4$ .* Flow Turbulence and Combustion, 92(3), pp. 673-698.

Ma, X., Karamanos, G., S., Karniadakin, G.E. (2000) *Dynamics and low*

*dimensionality of a turbulent near wake.* Journal of Fluid mechanics, 410, pp. 29-65.

Meneveau, C. & Katz, J., (2000) *Scale-invariance and turbulence models for large-eddy simulation.* Annual Review of Fluid Mechanics, 32(1), pp. 1-32.

Menter, F. (1996) *A comparison of some recent eddy-viscosity turbulence models.* Journal of Fluids Engineering, 118(3), pp. 514-519.

Menter, F. R. Kuntz, M. & Bender R. (2003) *A scale-adaptive simulation model for turbulent flow predictions,* 41st Aerospace Science Meeting & Exhibit, 6-9 January, 2003, Reno, Nevada.

Mittal, R. & Moin, P. (1997) *Stability of upwind-biased finite difference schemes for large-eddy simulation of turbulent flows.* AIAA Journal, 35, pp. 1415-1417.

Mittal, S. & Raghuvanshi, A. (2001) *Control of vortex shedding behind circular cylinder for flows at low Reynolds numbers.* International Journal for Numerical Methods in Fluids, 35(4), pp. 421-447.

Modi, V. J. and Wiland, E. (1970) *Unsteady aerodynamics of stationary elliptic cylinders in subcritical flow.* AIAA J. 8(10), pp. 1814–1821.

Nemes, A., Zhao, J., Lo Jacono, D. & Sheridan, J. (2012) *The interaction between flow-induced vibration mechanisms of a square cylinder with varying angles of attack.* J. Fluid Mech. 710, pp. 102–130.

Nicoud, F., Ducros, F. (1999) *Subgrid-scale stress modelling based on the square of the velocity gradient tensor.* CERFACS, 62(3), pp. 183-200.

Nguyen, V. & Nguyen, H. (2016) *Detached eddy simulations of flow induced vibrations of circular cylinders at high Reynolds numbers.* Journal of Fluids and Structures, 63, pp. 103-119.

Norberg, C. (1987) *Effects of Reynolds number and a low-intensity free stream turbulence on the flow around a circular cylinder,* Publikation Nr 87/2, Chalmers University of Technology.

Ong, L. & Wallace, J. (1996) *The velocity field of the turbulent very near wake of a circular cylinder*. Experiments in Fluids, 20(6), pp. 441-453.

Ong, M., Utne, T., Holmedal, L., Myrhaug, D. & Pettersen, B. (2009) *Numerical simulation of flow around a smooth circular cylinder at very high Reynolds numbers*. Marine Structures, 22(2), pp. 142-153.

Park, N., Lee, S., Lee, J. & Choi, H. (2006) *A dynamic subgrid-scale eddy viscosity model with a global model coefficient*. Physics of Fluids, 18(12), pp. 151-744.

Parnaudeau, P., Carlier, J., Heitz, D. & Lamballais, E. (2008) *Experimental and numerical studies of the flow over a circular cylinder at Reynolds number 3900*. Physics of Fluids, 20(8), pp. 085101.

Parsani, M., Ghorbaniasl, G., Lacor, C. & Turkel, E., (2010) *An implicit high-order spectral difference approach for large eddy simulation*. Journal of Computational Physics, 229(14), pp. 5373-5393.

Radi, A., Thompson, M., Sheridan, J. & Hourigan, K. (2013) *From the circular cylinder to the flat plate wake: The variation of Strouhal number with Reynolds number for elliptical cylinders*. Physics of Fluids, 25(10), pp. 101706.

Raffel, M., Willert, C., Wereley, S., & Kompenhans, J. (2007) *Particle image velocimetry: a practical guide*. 2nd edn. Springer.

Rahman, M., Karim, M., Alim, A. (2007) *Numerical investigation of unsteady flow past a circular cylinder using 2-D finite volume method*. Journal of Naval Architecture and Marine Engineering, 4, pp. 27-42.

Rajani,B., N., Kandasamy, A., Majumdar, S. (2015) *On the reliability of eddy viscosity based turbulence models in predicting turbulent flow past a circular cylinder using URANS approach*. Journal of Fluid Mechanics, 9(3), pp. 1421-1435.

Raman, S.K., Prakash, K.A. & Vengadesan, S. (2013) *Effects of axis ratio*

*on fluid flow around an elliptic cylinder using immersed boundary method.* Journal of Fluids Engineering, 135(11), pp. 111201.

Rocha, L., Saboya, F. & Vargas, J. (1997) *A comparative study of elliptical and circular sections in one- and two-row tubes and plate fin heat exchangers.* International Journal of Heat and Fluid Flow, 18(2), pp. 247-252.

Rodi, W. (1997) *Comparison of LES and RANS calculations of the flow around bluff bodies.* Journal of Wind Engineering and Industrial Aerodynamics, 69-71, pp. 55-75.

Rodi, W. (2006) *DNS and LES of some engineering flows.* Fluid Dynamics Research, 38(2-3), pp. 145-173.

Romero-Gomez, P. & Richmond, M. (2016) *Numerical simulation of circular cylinders in free-fall.* Journal of Fluids and Structures, 61, pp. 154-167.

Roshko, A. (1993) *Perspectives on bluff body aerodynamics.* Journal of Wind Engineering and Industrial Aerodynamics, 49(1-3), pp. 79-100.

Sarabandi, A. & Jabari Moghadam, A. (2016) *Thermal analysis of power-law fluid flow in a circular microchannel.* Journal of Heat Transfer, 139(3), pp. 032401.

Satti, R., Li, Y.B., Shock, R. (2011) *Unsteady flow predictions around tandem cylinders with sub-critical spacing.* 49th AIAA Aerospace Sciences Meeting Including the New Horizons Forum and Aerospace Exposition, 2011, Orlando, Florida.

Senocak, I., Shyy, W. & Johansen, S. (2007) *Statistical characteristics of unsteady Reynolds-Averaged Navier Stokes simulations.* Numerical Heat Transfer, Part B: Fundamentals, 47(1), pp. 1-18.

Sheard, G., Leweke, T., Thompson, M. & Hourigan, K. (2007) *Flow around an impulsively arrested circular cylinder.* Physics of Fluids, 19(8), pp. 083601.

Shintani, K., Umemura, A. & Takano, A. (1983) *Low-Reynolds-number flow past an elliptic cylinder.* Journal of Fluid Mechanics, 136(6), pp. 277-289.

Shur, M., Spalart, P., Squires, K., Strelets, M. & Travin, A. (2005) *Three-dimensionality in Reynolds-Averaged Navier-Stokes solutions around two-dimensional geometries*. AIAA Journal, 43(6), pp. 1230-1242.

Shur, M.L., Spalart, P.R., Strelets M., & Travin, A. (2008) *A hybrid RANS-LES approach with Delayed-DES and wall-modeled LES capabilities*. Int.J. Heat Fluid Flow., 29(6), pp. 1638-1649.

Sidebottom, W., Ooi, A. & Jones, D. (2012) *A parametric study of turbulent flow past a circular cylinder using Large Eddy Simulation*. 18th Australian Fluid Mechanics Conference, 2012, Launceston, Australia.

Sørensen, N., Bechmann, A. and Zahle, F. (2011) *3D CFD computations of transitional flows using DES and a correlation based transition model*. Wind Energy, 14(1), pp. 77-90.

Spalart, P.R. and Allmaras, S.R. (1994) *A one-equation turbulence model for aerodynamic flows*. Recherche Aerospatiale, 1, pp. 5-21.

Spalart, P. and Shur, M. (1997) *On the sensitization of turbulence models to rotation and curvature*. Aerospace Science and Technology, 1(5), pp. 297-302.

Spalart, P., Deck, S., Shur, M., Squires, K., Strelets, M. & Travin, A. (2006) *A New Version of Detached-eddy Simulation, resistant to ambiguous grid densities*. Theoretical and Computational Fluid Dynamics, 20(3), pp. 181-195.

Stack, D. and Bravo, H. (2009) *Flow separation behind ellipses at Reynolds numbers less than 10*. Applied Mathematical Modelling, 33(3), pp. 1633-1643.

Taneda, S. (1956) *Experimental investigation of the wakes behind cylinders and plates at low Reynolds numbers*. Journal of the Physical Society of Japan, 11(3), pp. 302-307.

Tarvin, A., Shur, M., Strelets, M., & Spalart, P. (1999) *Detached-Eddy Sim-*

*ulations past a circular cylinder*, Flow Turbulence and Combustion, 63, pp. 293-313.

Thompson, M., Radi, A., Rao, A., Sheridan, J. & Hourigan, K. (2014) *Low-Reynolds-number wakes of elliptical cylinders: from the circular cylinder to the normal flat plate*. Journal of Fluid Mechanics, 751, pp. 570-600.

Tomboulides, A. and Orszag, S. (2000) *Numerical investigation of transitional and weak turbulent flow past a sphere*. Journal of Fluid Mechanics, 416, pp. 45-73.

Trefethen, L. N. (1996) *Finite difference and spectral methods for ordinary and partial differential equations (Chapter 4. Accuracy, stability and convergence)*, unpublished text, available at <http://people.maths.ox.ac.uk/trefethen/pdetext.html> )

Wang, P., Fröhlich, J., Michelassi, V. & Rodi, W. (2008) *Large-eddy simulation of variable-density turbulent axisymmetric jets*. International Journal of Heat and Fluid Flow, 29(3), pp. 654-664.

Wei, X. (2014) *Kinematic dynamo induced by helical waves*. Geophysical and Astrophysical Fluid Dynamics, 109(2), pp. 159-167.

Weinmann, M., Sandberg, R. & Doolan, C. (2014) *Tandem cylinder flow and noise predictions using a hybrid RANS/LES approach*. International Journal of Heat and Fluid Flow, 50, pp. 263-278.

Williamson, C. (1996) *Three-dimensional vortex dynamics in bluff body wakes*. Experimental Thermal and Fluid Science, 12(2), pp. 150-168.

Wornom, S., Ouvrard, H., Salvetti, M., Koobus, B. & Dervieux, A. (2011) *Variational multiscale large-eddy simulations of the flow past a circular cylinder: Reynolds number effects*. Computers and Fluids, 47(1), pp. 44-50.

Wu, W., Bernitsas, M. & Maki, K. (2014) *RANS Simulation versus experiments of flow induced motion of circular cylinder with passive turbulence control at  $35,000 < Re < 130,000$* , Journal of Offshore Mechanics and Artics

Engineering, 136(4), pp. 041-802.

Xiao, Z., Liu, J., Huang, J. & Fu, S. (2013) *Numerical dissipation effects on massive separation around tandem cylinders*. AIAA Journal, 50(5), pp. 1119-1136.

Xiao, Z. & Luo, K. (2014) *Improved delayed detached-eddy simulation of massive separation around triple cylinders*. Acta Mechanica Sinica, 31(6), pp. 799-816.

Zhao, J. (2012) *Flow-induced vibration of circular and square cylinders with low mass and damping*. Doctor of Philosophy, Monash University, Australia.

Zhao, J., Leontini, J., Lo Jacono, D. & Sheridan, J. (2014) *Fluid-structure interaction of a square cylinder at different angles of attack*. Journal of Fluid Mechanics, 747, pp. 688-721.